GEOLOGICA ULTRAIECTINA

Mededelingen van de
Faculteit Geowetenschappen
Universiteit Utrecht

No. 249

Deconvolution of land seismic data for source and receiver characteristics and near-surface structure

Robbert van Vossen

The research described in this thesis was carried out at:

Department of Earth Sciences
Utrecht University
Budapestlaan 4
3584 CD Utrecht
The Netherlands

Schlumberger Cambridge Research
High Cross, Madingley Road
Cambridge CB3 0EL
United Kingdom

http://www.geo.uu.nl/Research/Seismology/

This work was conducted under the programme of the Vening Meinesz Research School of Geodynamics, and was funded by Schlumberger.

Printed by Wöhrmann Print Service, Zutphen

ISBN: 90-5744-000-8

Deconvolution of land seismic data for source and receiver characteristics and near-surface structure

Deconvolutie om effecten van bron, ontvanger en ondiepe structuur op landseismische data te bepalen

(met een samenvatting in het Nederlands)

PROEFSCHRIFT

TER VERKRIJGING VAN DE GRAAD VAN DOCTOR
AAN DE UNIVERSITEIT UTRECHT
OP GEZAG VAN DE RECTOR MAGNIFICUS, PROF. DR. W.H. GISPEN,
INGEVOLGE HET BESLUIT VAN HET COLLEGE VOOR PROMOTIES
IN HET OPENBAAR TE VERDEDIGEN
OP WOENSDAG 13 APRIL 2005 DES MIDDAGS TE 14:30 UUR

DOOR

Robbert van Vossen

Geboren op 13 juli 1977, te Raamsdonk

Promotor: Prof. Dr. J. Trampert*
Copromotor: Dr. A. Curtis†

*Department of Earth Sciences, Utrecht University, The Netherlands
†Schlumberger Cambridge Research, Cambridge, United Kingdom
and:
School of GeoSciences, The University of Edinburgh, Scotland

Suddenly a thought would wander across his face with the freedom of a bird,
flutter for a moment in his eyes, settle on his half-opened lips,
and remain momentarily lurking in the lines of his forehead. Then it would disappear,
and once more his face would glow with a radiant insouciance

I. A. Gončarov, Oblomov

Members of the dissertation committee:

Prof. Dr. K. Holliger
Institute of Geophysics
ETH – Swiss Federal Institute of Technology

Prof. Dr. R. Snieder
Department of Geophysics,
Colorado School of Mines

Prof. Dr. C.J. Spiers
Department of Earth Sciences,
Utrecht University

Dr. Ir. P.L. Vermeer
WesternGeco Oslo Technology Centre

Prof. Dr. Ir. C.P.A. Wapenaar
Department Applied Earth Sciences
Technical University of Delft

Contents

Chapter 1

Introduction

1.1 Influence of near-surface conditions on land seismic data

The seismic reflection method has long been used as one of the most effective tools in the search for oil and gas. The interpretation of a seismogram is therefore primarily directed to structural or stratigraphic features of the subsurface, and for the more subtle interpretation of what occupies the pore space of potential subsurface reservoirs. However, since most seismic data are acquired at or close to the Earth's surface, the interpreter must be aware of the influence of near-surface conditions on the acquired seismic data.

This is especially important when near-surface conditions change within a given survey. This situation is characteristic for land seismic settings, where the near-surface weathered layer is usually characterized by low and highly variable velocities and high attenuation levels (Cox, 1999), and where the coupling of neighbouring seismic sources or receivers can vary greatly even across similar ground or near-surface conditions. These changing near-surface conditions bias the information which is obtained on the subsurface.

We divide the influence of the near-surface into two categories: (i) near-surface wave propagation, and (ii) wavefield acquisition (see Figure 1.1). Acquisition effects depend on the material properties close to the sources and receivers which influence the wavefield excitation and measurements, and on variability in the techniques used to couple sources and receivers to the ground; near-surface wave propagation on the other hand comprises the delaying and distorting effects of the near-surface on the wavefield. A fundamental difference between acquisition and near-surface effects is that variations due to acquisition effects can influence wavefield measurements on a sub-wavelength scale, whereas wavefield propagation variations due to near-surface effects are usually only significant over length scales of the order of a wavelength.

It is important to realize that the near-surface effects influence both processing and interpretation of the wavefield. In conventional P-wave imaging for example, the aim is

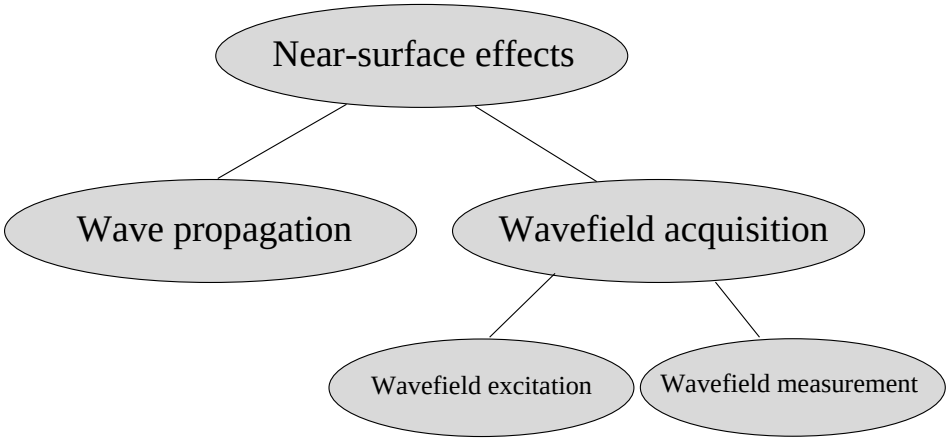

Figure 1.1: Categorization for near-surface effects on land seismic data. We distinguish near-surface wave propagation from acquisition effects. Wavefield acquisition comprises both wavefield excitation and wavefield measurement.

to create a zero-offset section consisting of primary compressional reflections only. In order to create such a section, ground roll, multiples, and converted waves have to be suppressed. Since the performance of multichannel filter operations, which are commonly used to remove ground roll and multiples, deteriorate in the presence of source and receiver perturbations, it is important to compensate appropriately for such variations early in the processing sequence (Kelamis and Verschuur, 2000). Furthermore, the near-surface effects could potentially lead to misinterpretations, e.g. amplitude-versus-offset (AVO) trends can be altered by these changes in near-surface conditions (Castagna and Backus, 1993). We now introduce the two main near-surface effects in turn.

1.2 Near-surface wave propagation

Near-surface wave propagation is important because strong near-surface velocity contrasts are commonly encountered in land seismic surveys. Both P- and S-wave velocities may change by nearly an order of magnitude across the interface defining the top of the bedrock, and P-velocities change up to 100 % across the top depth of total water saturation, i.e. the water table (Stümpel et al., 1984; Goforth and Hayward, 1992). Consequently, the near-surface low velocity layer may act as a waveguide in which energy may propagate over long distances with little loss due to geometrical spreading. This could mask reflections from a deeper target (Hunter et al., 1984; Robertsson et al., 1996). Furthermore, the near-surface is often very heterogeneous, resulting in scattering of seismic energy. Thus, near-surface wave propagation is usually very complex, and variations in this structure often cause data perturbations of a similar magnitude to the target signal

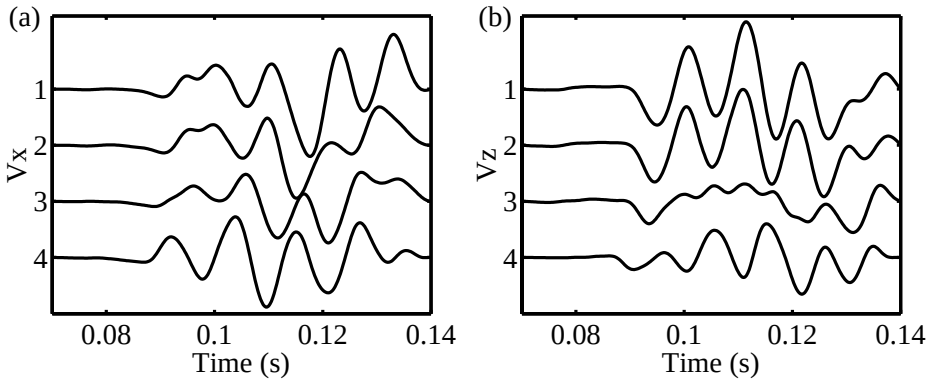

Figure 1.2: Traces of the horizontal component v_x (a) and vertical componet v_z (b) of the particle velocity acquired in a land seismic experiment at different depths. The traces labelled (1) and (2) are acquired at the free surface, 0.30 m apart, trace (3) was acquired at 0.50 m depth, and trace (4) at approximately 1.0 m depth, between the horizontal locations of (1) and (2).

(e.g. Goupillaud, 1961).

The complexity of near-surface wave propagation is illustrated with a field data example. Figure 1.2 shows traces of horizontal and vertical component recordings which are acquired at the free-surface, at 0.50 m depth, and at approximately 1.0 m depth, respectively. The large differences between the recordings are caused by interfering waves in the shallow near-surface. These cannot be caused by acquisition-related effects because the measurements obtained at the surface can be related to the measurements obtained at 1.0 m depth using the Haskell-Thomson propagator formalism (Thomson, 1950; Haskell, 1953; Gilbert and Backus, 1965). This formalism describes the propagation of plane waves through a horizontally layered medium. Thus, we can explain the observed rapid variations in the wavefield with a relatively simple model for plane wave propagation provided we know the near-surface material properties that control how the waves propagate. As indicated by Goupillaud (1961), accurate knowledge of these near-surface material properties is essential to compensate recorded data for effects of near-surface stratification.

1.3 Acquisition effects

Acquisition effects comprise differences in source repeatability and in both source and receiver coupling. The source strength and signature depend on the deformation in the near-source field, and therefore depend on the (an)elastic properties of the soil (Kähler and Meissner, 1983; Aritman, 2001). Consequently, for identical sources located in soft soil

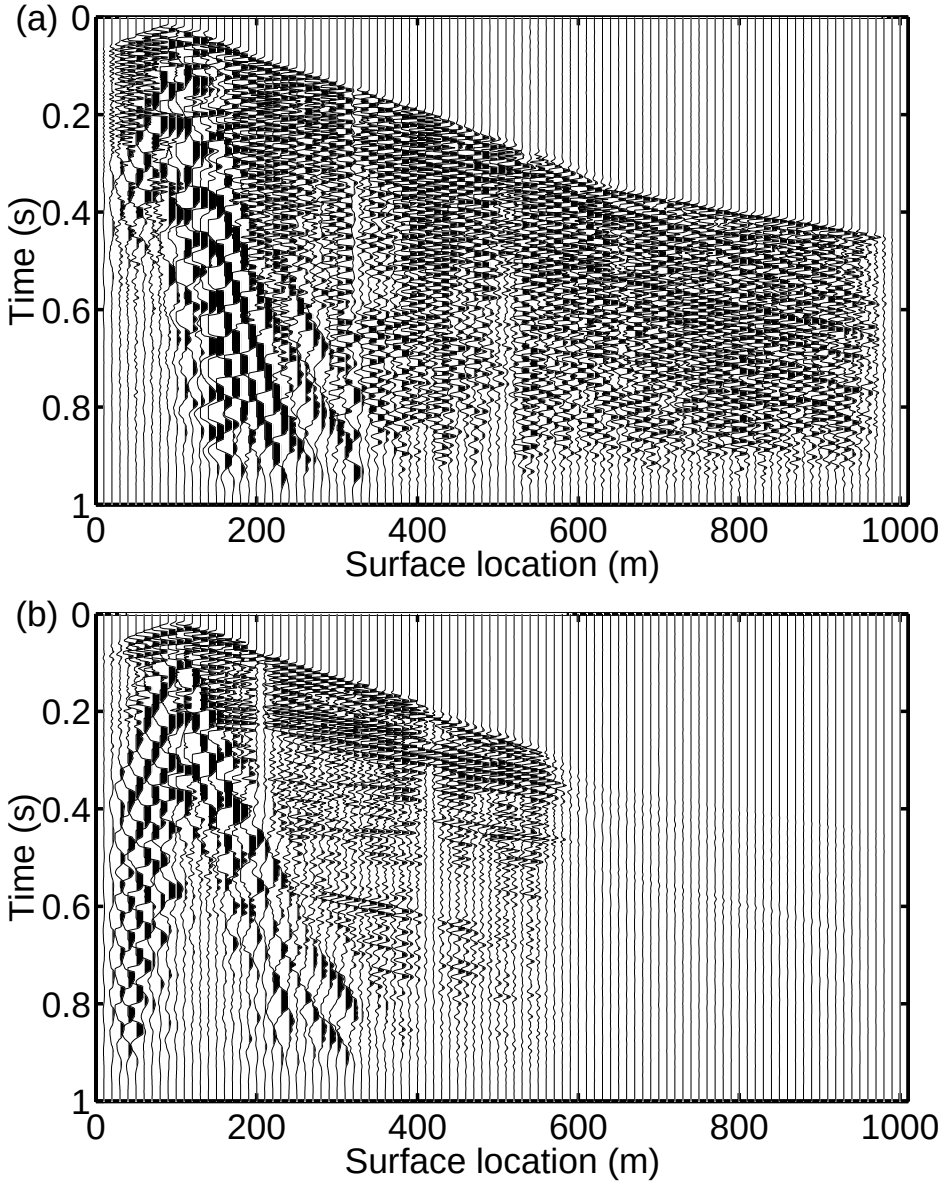

Figure 1.3: Example of raw field data. (a) Common source gather and (b) common receiver gather with identical trace scaling. The traces have been scaled with a ramp in offset to ensure that the traces are more balanced in amplitudes (data courtesy of WesternGeco).

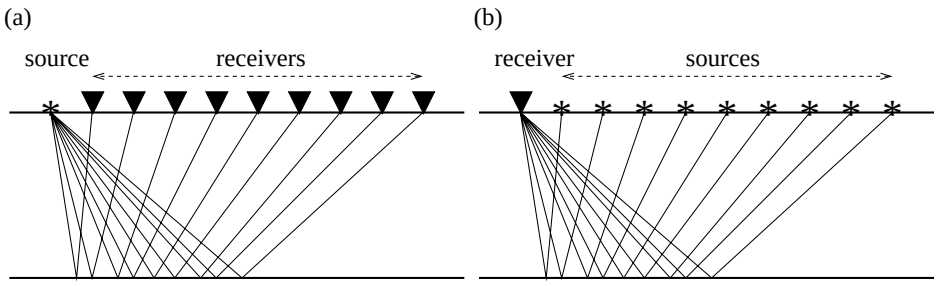

Figure 1.4: Example of a common source (a) and common receiver (b) gather.

and hard rock, respectively, the source strength and signature will differ significantly. This effect is referred to as source coupling. Therefore, marine seismic data are generally of better quality than land seismic data, since uniform elastic properties of seawater provide consistent source coupling. For land data on the other hand, the near-surface is often characterized as a zone with low velocities and highly variable elastic material properties, resulting in differences in source strength and signature.

Receiver coupling is the difference between the ground motion measured by the geophone and the motion of the ground without the geophone. This includes effects of the weight and shape of the geophone, and of the contact of the geophone to the ground (Drijkoningen, 2000). Coupling differences between geophones can be mainly attributed to the geophone-ground contact, i.e. differences between a well-planted geophone and a badly planted geophone, and this is inherently related to the firmness of the soil (Krohn, 1984).

We illustrate the influence of acquisition effects with traces recorded in a common shot and a common receiver gather (Figure 1.3). Figure 1.4 schematically shows the traces which are collected in these gathers. A common shot gather contains recordings of one physical experiment, i.e. one source and an array of geophones, whereas a common receiver gather contains records of multiple shots collected at one single receiver. The traces in the considered common receiver gather are reciprocal to the traces in the corresponding common source gather: that is, these traces are obtained with source and receiver positions interchanged.

If we assume that reciprocal conditions (Knopoff and Gangi, 1959; White, 1960) are satisfied, we can attribute the differences between the normal and reciprocal recordings to the acquisition effects. In that case, the medium response is identical for both the normal and reciprocal recordings.

However, several differences can be observed between the traces in the common shot and common receiver gather (Figure 1.3). First, in the common receiver domain the amplitudes of the recorded traces are dramatically reduced for surface locations x beyond 600 m. Figure 1.5 shows that these changes are correlated to differences in near-surface material properties. At surface location $x = 600$ m, the near-surface material properties change from moist-to-wet sediment to dry sand. This alters the source strength and

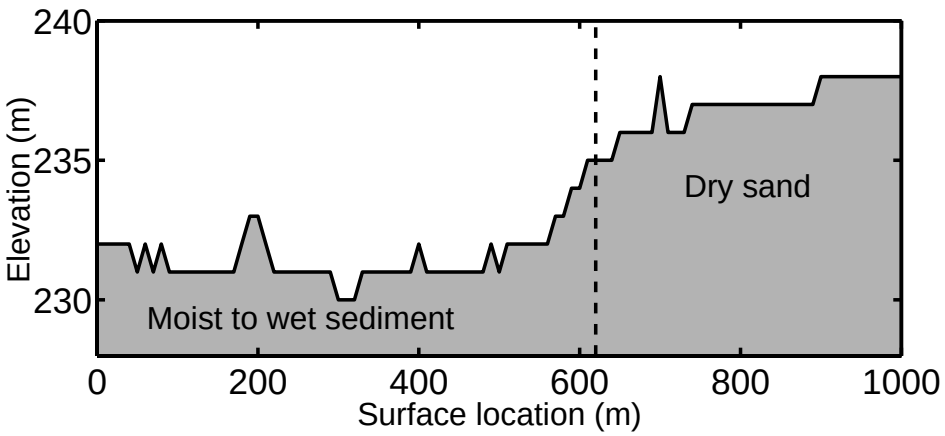

Figure 1.5: Surface topography and indication of near-surface material properties (Courtesy of WesternGeco).

signature of the explosive source used for generating these data. At the receiver side, the recordings do not show a pattern which is correlated to the changes in near-surface conditions.

Second, for the first 50 traces, the trace-to-trace consistency is better in the common receiver domain, indicating that the receiver terms vary more rapidly laterally. As a result, the reflection hyperbolas between 0.20 and 0.30 s and 0.60 and 0.80 s can be identified more easily in the common-receiver domain than in the common shot domain.

1.4 Outline of the thesis

The examples for the near-surface wave propagation and acquisition effects indicate that both effects have to be taken into account during the data processing, and that their influence on the processed data have to be understood by the interpreter.

In order to better understand the effects of near-surface heterogeneities on the recorded data, we first aim to obtain estimates for near-surface P- and S-wave velocities. However, sensitivity for these material properties is usually poor within the seismic frequency band when only geophones are deployed at the free surface. Therefore, we used a three-dimensional geophone configuration. In addition to measurements at the free-surface, we also used data acquired at shallow depth. In Chapter 2, we discuss three different methods for estimating near-surface P- and S-wave velocities which are based on inversion of the wave equation.

In Chapter 3, we continue with a field data application of one of these methods, which is based on the Haskell-Thomson propagator formalism (Thomson, 1950; Haskell, 1953; Gilbert and Backus, 1965). We refer to this method as propagator inversion. Results

indicated that near-surface material properties vary rapidly with depth close to the free-surface: we observed subsonic near-surface P-velocities in the top meter of the near-surface, whereas the average velocity for the near-surface low velocity layer is well above the sonic P-wave velocity.

In Chapter 4, we introduce a new method for correcting recorded data for source and receiver amplitude perturbations. The method is based on reciprocity, and is applicable to both single and multicomponent data. Furthermore, the corrections can be calculated with either a part of, or the whole seismogram, and therefore, it can be implemented purely as a data preprocessing step. This is an important characteristic of this method, because existing surface-consistent deconvolution techniques (Taner and Koehler, 1981; Levin, 1989; Cambois and Stoffa, 1992; Cary and Lorentz, 1993) are applicable to primary reflections only, and hence require other preprocessing to isolate these arrivals.

In Chapter 5, we apply this new method to a field data set acquired in Manistee County, Michigan. This is an excellent test case for this method because changing near-surface conditions degrade the quality of the recorded data (see Figures 1.3 and 1.5). Application of the source and receiver equalization resulted in a significant improvement of the signal-to-noise ratio, both on prestack and poststack data. Furthermore, the obtained source corrections are correlated to changing near-surface conditions.

Chapter 2

Propagator and wave-equation inversion for near-receiver material properties

Abstract

Near-receiver material properties are required for the separation of the recorded wavefield into upgoing and downgoing P and S waves, and are also important for static time-shift corrections. However, it is difficult, especially in land seismics, to obtain reliable estimates for these local material properties using conventional techniques. We compare three methods for estimating these material properties using a 3D geophone configuration. The first two methods are based on inversion of the wave equation and can be used on almost all of the recorded wavefield. However, they require that the wavefield is recorded by a dense 3D receiver group to allow the computation of either spatial wavefield derivatives or interpolants. The third approach is based on the inversion of the vertical wavefield propagator. We present a procedure for estimating this propagator using only two multicomponent geophones, one buried and one positioned at the surface. Propagator estimation and inversion avoids the explicit computation of wavefield derivatives, and is therefore less sensitive to measurement errors than both wave-equation inversion schemes. However, in the form presented it requires the identification of arrivals of incoming waves that are isolated in time, and can only be applied to such data. Noise tests demonstrate that the propagator inversion provides accurate estimates for P- and S-wave velocities of a near-surface low velocity layer, and is robust with respect to signal-generated near-surface reverberations. In case of a near-surface velocity gradient, velocities are obtained which are consistent with effective medium velocities.

This chapter has been published as: Van Vossen, R., Trampert, J. and Curtis, A., Propagator and wave-equation inversion for near-receiver material properties, *Geophysical Journal International*, **157**, 796-812, 2004.

2.1 Introduction

Most observations of seismic waves are made either at, or very near to the Earth's surface. Before reliable subsurface information can be retrieved from these recordings, corrections are required for local near-receiver structure, since variations in this structure often cause data perturbations of a similar magnitude to the target signal (e.g. Goupillaud, 1961). The variability of the elastic properties close to the measurement surface is due to a variety of geological processes and petrophysical properties, among them porosity, permeability, fractures, the presence of fluids in pores, compaction, diagenesis and metamorphism (Toksöz et al., 1976).

Variations in near-receiver elastic properties cause the following complications. First, receiver static variations in the data are receiver-to-receiver traveltime anomalies which occur due to the propagation of most of the seismic energy through the heterogeneous shallow structure. Secondly, poor repeatability of the source signature and changes in the source radiation pattern are also attributed to lateral changes in near-surface material properties (Aritman, 2001). Thirdly, lateral variations in free-surface reflectivity cause differences in the amount of reflected and converted energy. This results in amplitude perturbations, especially on horizontal recordings (Kähler and Meissner, 1983). Decomposing the recorded wavefield into upgoing and downgoing P and S waves allows an analysis of these wavefields without the effects of any free-surface interaction (e.g. Dankbaar, 1985; Wapenaar et al., 1990). However, to perform wavefield decomposition the free-surface reflectivity, and hence local sub-receiver properties, need to be known.

Since conventional seismic data are acquired only at the surface, the problem of determining seismic subsurface properties is ill-posed. Curtis and Robertsson (2002) therefore proposed to use dense 3D recording patterns to better constrain land seismic near-surface velocities. The pattern consists of a single buried three-component geophone and several surface geophones. The receivers are sufficiently close that spatial wavefield derivatives can be computed. These derivatives are required to invert the equation of motion for local material parameters. Robertsson and Muyzert (1999) originally introduced this recording geometry to accomplish P/S separation by explicitly computing the divergence and the curl of the wavefield.

In other research fields, e.g. medical imaging, several concepts to estimate local material properties have been developed. Medical practitioners aim to estimate local material properties since variations in mechanical properties of tissue often reflect early stage pathology (Gao et al., 1996). Unlike in conventional seismic surveys, the displacement field is measured throughout a tissue using ultrasound or magnetic resonance imaging (MRI) based measurement techniques (Muthupillai et al., 1995). Quantitative elasticity reconstruction is achieved either by comparing modeled stress to measured strain (Gao et al., 1996; Van Houten et al., 1999) or by direct inversion of the observed displacement field. For example, Romano et. al. (1998) and Oliphant et al. (1999;2001) have shown that elastic properties can be estimated by localized inversion of the equation of motion.

We propose an alternative method to estimate local near-surface P- and S-wave velocities. This method was originally proposed by Trampert et al. (1993) to estimate the S-wave velocity structure and the quality factor in a borehole. This was achieved by esti-

mating and inverting the vertical SH wavefield propagator derived from the spectral ratio of a downhole data record over a surface data record. We formulate this approach for the elastic P-SV case, and a strategy for inverting the propagator for near-surface P- and S-wave velocities is developed.

Before discussing propagator estimation and inversion, we briefly review techniques based on direct inversion of the wave equation, including those from medical fields. For purpose of comparison, we illustrate the importance of two of the methods and our propagator inversion method using signals perturbed by noise.

2.2 Wave-equation inversion

Oliphant et al. (1999; 2001) and Curtis and Robertsson (2002) proposed to constrain local material properties by algebraic inversion of the wave equation. A Cartesian coordinate system ($x_1 = x$,$x_2 = y$,$x_3 = z$) is used with positive vertical direction x_3 oriented downwards. The particle velocity is regarded as a function of space and time t, and is written as $\mathbf{v} = \mathbf{v}(\mathbf{x}, t)$. Overdots are used to indicate time derivatives (e.g. $\dot{\mathbf{v}} = \partial\mathbf{v}/\partial t$ and $\ddot{\mathbf{v}} = \partial^2\mathbf{v}/\partial t^2$). The wave equation for $\mathbf{v}$ in a homogeneous, isotropic medium is then given by (Aki and Richards, 2002):

$$\ddot{\mathbf{v}} = \alpha^2 \nabla (\nabla \cdot \mathbf{v}) - \beta^2 \nabla \times (\nabla \times \mathbf{v}) , \tag{2.1}$$

where $\alpha = [(\lambda + 2\mu)/\rho]^{1/2}$ is the P-wave velocity, $\beta = (\mu/\rho)^{1/2}$ is the S-wave velocity, and λ and μ are the Lamé parameters. Derivative conditions can be derived from the constitutive equation and the free-surface boundary conditions. The constitutive equation for a homogeneous, elastic medium reads:

$$\dot{\sigma}_{ij} = \lambda \partial_k v_k \delta_{ij} + \mu \left(\partial_i v_j + \partial_j v_i\right) , \tag{2.2}$$

where δ_{ij} is the Kronecker delta and ∂_k denotes the spatial derivative with respect to coordinate x_k. The summation convention applies to repeated subscripts. Boundary conditions state that the traction σ_{i3} vanishes at the free surface for $i = 1, 2, 3$, although in practice this is only an approximation, as air waves can exist. By setting $\sigma_{i3} = 0$ at the free surface, we can substitute for vertical wavefield derivatives expressions with horizontal derivatives:

$$\partial_3 v_1 = -\partial_1 v_3, \tag{2.3}$$

$$\partial_3 v_2 = -\partial_2 v_3, \tag{2.4}$$

$$\partial_3 v_3 = -\left(\frac{\alpha^2 - 2\beta^2}{\alpha^2}\right)\left(\partial_1 v_1 + \partial_2 v_2\right) . \tag{2.5}$$

Curtis and Robertsson (2002) showed that the following system of equations is obtained after substitution of the free-surface derivative conditions into the wave equation:

$$\ddot{v}_1 = \beta^2 A_1(t) - \alpha^{-2}\beta^4 B_1(t), \tag{2.6}$$

$$\ddot{v}_2 = \beta^2 A_2(t) - \alpha^{-2}\beta^4 B_2(t), \tag{2.7}$$

$$\ddot{v}_3 = \alpha^2 A_3(t) - \beta^2 B_3(t). \tag{2.8}$$

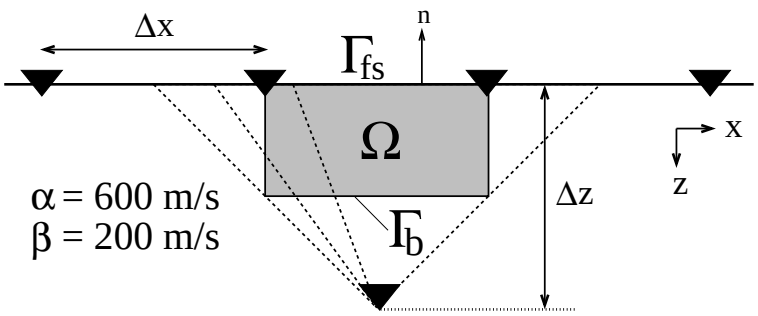

Figure 2.1: Geophone configuration for near-surface velocity estimation. The volume Ω bounded by surface $\Gamma = \Gamma_b \cup \Gamma_{\text{fs}}$ with outward pointing normal vector $\mathbf{n}$ is used in the variational formulation. Wavefield interpolation is performed along the dashed lines.

Expressions for the measurable coefficients A_i and B_i are given in Appendix A.1. These coefficients require the evaluation of spatial wavefield derivatives. A receiver group as illustrated in Figure 2.1 allows the computation of these spatial and temporal derivatives using finite-difference operators (assuming that $v_2 = 0$ and $\partial_2 \mathbf{v} = \partial_{22} \mathbf{v} = \mathbf{0}$). The spatial derivatives can only be obtained accurately if the horizontal and vertical geophone spacings Δx and Δz satisfy the following criteria: $\Delta z \sim \lambda_z^{min}/6$ and $\Delta x \sim \lambda_x^{min}/6$, where λ_x^{min} and λ_z^{min} are the minimum effective wavelengths in the x or z direction, respectively (Levander, 1988; Muijs et al., 2002). Assuming that these spatial derivatives can be calculated, equations (2.6)–(2.8) can be inverted for α and β. The attractiveness of this method is that it can deal with the complete wavefield (Curtis and Robertsson, 2002). On the other hand, it requires the computation of second-order derivatives which are likely to be affected by noise and measurement errors (Muijs et al., 2002).

Romano et al. (1998; 2000) suggested to transform the wave equation (2.1) into an integral equation to avoid the computation of spatial wavefield derivatives. This approach is referred to as the variational formulation, and we present it for estimating local near-surface material properties using the geophone configuration shown in Figure 2.1. Consider a vector-valued function $\mathbf{w}$ and a volume Ω bounded by a surface Γ with outward pointing normal vector $\mathbf{n}$ (Figure 2.1). In Appendix A.2, we demonstrate that equation (2.1) is equivalent to

$$\int_\Omega \mathrm{d}\Omega \, \mathbf{w} \cdot \ddot{\mathbf{v}} = \int_\Omega \mathrm{d}\Omega \, \mathbf{v} \cdot \mathbf{w}_\Omega + \int_\Gamma \mathrm{d}\Gamma \, \mathbf{n} \cdot \mathbf{w}_\Gamma, \tag{2.9}$$

where

$$\mathbf{w}_\Omega = \alpha^2 \nabla (\nabla \cdot \mathbf{w}) - \beta^2 \nabla \times (\nabla \times \mathbf{w}), \tag{2.10}$$

$$\mathbf{w}_\Gamma = \left(\alpha^2 - \beta^2\right) \left[\mathbf{w} (\nabla \cdot \mathbf{v}) - \mathbf{v} (\nabla \cdot \mathbf{w})\right] - \beta^2 \left[\mathbf{v} \cdot (\nabla \mathbf{w})^T - \mathbf{w} \cdot (\nabla \mathbf{v})^T\right]. \tag{2.11}$$

The surface $\Gamma = \Gamma_b \cup \Gamma_{\text{fs}}$, where Γ_{fs} is the surface of Ω which coincides with the free surface (see Figure 2.1). Because the vector-valued function $\mathbf{w}$ can be chosen arbitrarily, boundary conditions can be imposed on $\mathbf{w}$ to aid the computation of the integrals in equation (2.9). If we assume that

$$\mathbf{w} = \mathbf{0} \qquad \text{on} \quad \Gamma_b \tag{2.12}$$

and

$$(\nabla \mathbf{w})^T \cdot \mathbf{n} = \mathbf{0} \qquad \text{on} \quad \Gamma_b, \tag{2.13}$$

the contribution of the surface integral along Γ_b vanishes. The evaluation of the surface integral along Γ_{fs} requires the computation of first-order spatial wavefield derivatives at the free surface. These are also needed for accurate wavefield interpolation throughout Ω: firstly, the wavefield and its horizontal derivative are interpolated along the free surface using B-splines (Unser, 1999). Secondly, the vector gradient of the wavefield is obtained using the free-surface conditions [equations (2.3)–(2.5)]. Next, the wavefield in Ω is interpolated along lines from the surface to the buried geophone (the dashed lines in Figure 2.1). The interpolated wavefield is parameterized by second-order polynomials, which are uniquely determined by the interpolated wavefield at the free surface, the directional derivative at the free surface, and the wavefield at depth Δz. For sufficiently accurate wavefield interpolation within volume Ω, we found that, similar to the previous method, $\Delta z \sim \lambda_z^{min}/6$ and $\Delta x \sim \lambda_x^{min}/6$. Finally, the surface and volume integrals are evaluated using the trapezium rule.

Consider the following independent vector-valued functions:

$$\mathbf{w_1} = (f_w, 0, 0)^T, \tag{2.14}$$

$$\mathbf{w_2} = (0, 0, f_w)^T, \tag{2.15}$$

with

$$f_w(x_l, z_l) = \left(x_l^4 - 2x_l^2 + 1\right)(z_l - 1)^2. \tag{2.16}$$

The local coordinates x_l and z_l are related to x and z according to:

$$x_l = 2x/\Delta x_\Omega, \tag{2.17}$$

$$z_l = (2z - \Delta z_\Omega)/\Delta z_\Omega, \tag{2.18}$$

with Δx_Ω and Δz_Ω the lengths of the sides of volume Ω. The local coordinates are defined on the domain $x_l \in [-1, 1]$ and $z_l \in [-1, 1]$. The functions $\mathbf{w_1}$ and $\mathbf{w_2}$ satisfy the boundary conditions [equations (2.12) and (2.13)].

We illustrate both methods with a 2D example. Synthetic data for a half-space model are computed using the Cagniard-de Hoop method (de Hoop and Van der Hijden, 1983). An explosive line source oriented in the x_2 direction is located at 200 m depth and emits a Ricker wavelet with a dominant frequency of 40 Hz. The P-wave velocity is 600 m/s, the S-wave velocity is 200 m/s, and the density is 1600 kg/m^3. Multicomponent geophones

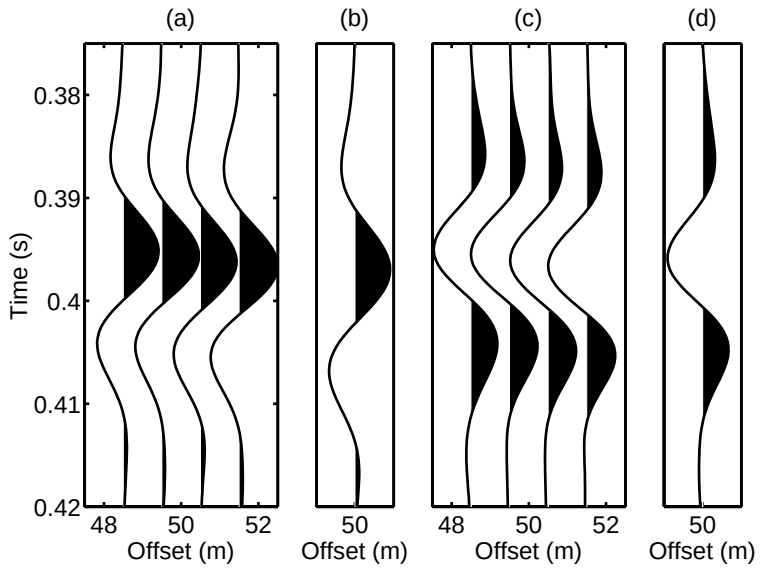

Figure 2.2: Synthetic data traces for (a) v_x at the surface, (b) v_x at depth Δz, (c) v_z at the surface, and (d) v_z at depth Δz.

are centered around 50 m offset. The horizontal geophone spacing $\Delta x = 1.0$ m and the buried geophone is located at 0.50 m depth. For a Ricker wavelet with a 40 Hz dominant frequency, the maximum frequency f_{max} with significant energy is 80 Hz. Then, the minimum wavelength $\lambda_{min} = c_{min}/f_{max} = 2.5$ m, with c_{min} the minimum phase velocity. The geophone configuration satisfies the wavelength condition for the computation of derivatives and interpolants. The lengths of the sides of Ω are $\Delta x_\Omega = \Delta x$ and $\Delta z_\Omega = \Delta z/2$ (Figure 2.1). Recorded data are shown in Figure 2.2.

The constraints of direct wave-equation inversion on α and β are illustrated in Figure 2.3. For the given model values α and β, there is a good match between the left and right side of equations (2.6) and (2.8). For noise-free data, derivative operators are obtained sufficiently accurately with the geophone configuration of Figure 2.1. Perturbing α or β results in amplitude changes in the waveforms of the right side terms in equations (2.6)–(2.8). We compare the sensitivity to perturbations in α and β to the effect of measurement errors in the particle velocity recordings. To study these effects, 25 dB uncorrelated Gaussian noise [peak-peak energy signal-to-noise (S/N) ratio] was added to the velocity recordings. A bandpass filter (20 Hz $< f <$ 100 Hz) was applied to these recordings before computing the wavefield derivatives. As a result, the effect of noise on temporal wavefield derivatives is reduced. However, spatial wavefield derivatives are still severely distorted by the added noise. Estimates for α are especially affected, since the wavelength for P waves is larger than for S waves. Consequently, the S/N ratio for spatial

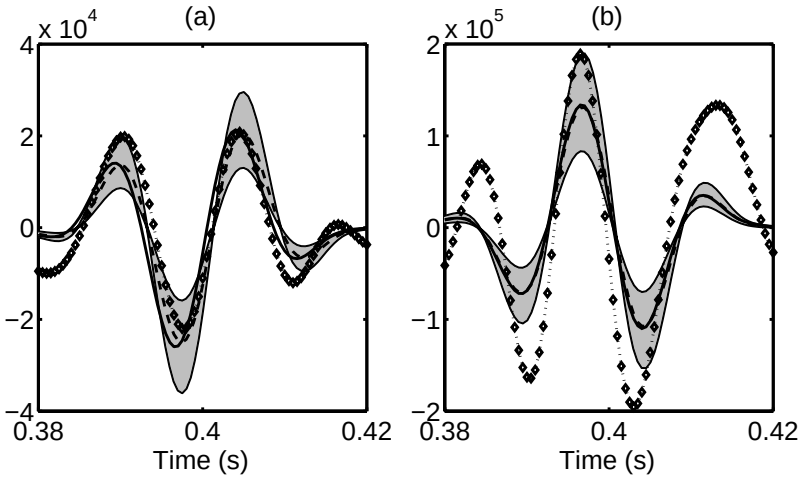

Figure 2.3: Sensitivity analysis for direct wave-equation inversion. (a) shows the waveforms of the left (dashed) and right side (solid line) of equation (2.6), and the gray area illustrates the region for $\pm$ 20% perturbations in β. The dotted line shows the effect of Gaussian noise (25 dB S/N ratio) added to the velocity recordings on the right side of equation (2.6). Similarly, (b) shows the waveforms of equation (2.8) and illustrates the region for $\pm$ 20% perturbations in α. The dotted line shows the effect of Gaussian noise (25 dB S/N ratio) added to the velocity recordings.

P-wave derivatives is lower than for S-wave derivatives.

Figure 2.4 shows a similar analysis for the variational approach. There is a good agreement between the left and right side of equation (2.9) for the given model values α and β. In principle, the interpolation and integration steps are sufficiently accurately using the geophone configuration shown in Figure 2.1. Perturbing α or β results in amplitude changes in the waveforms of the right side terms in equation (2.9). A comparison between the sensitivity to α and β and the effects of noise (25 dB S/N ratio) shows that this approach is also very sensitive to effects of noise, and again mostly for α.

These sensitivity tests demonstrate that it may only be possible to constrain β using these methods. There is not a clear difference between the derivative and variational formulation. However, for a geophone configuration with more than one buried geophone, an interpolation scheme can be developed which is less sensitive to random errors.

Muijs et al. (2002) studied the effect of deployment related errors, such as misorientation and mislocation of geophones in a 3D recording geometry, on the computation of divergence and curl. These are particularly sensitive to misorientations of geophones, requiring that the orientations of all geophones be accurate within 2°.

Instead of using the full wave-equation, the free-surface condition given in equation (2.5) can be used to determine a velocity ratio between α and β (Curtis and Robertsson,

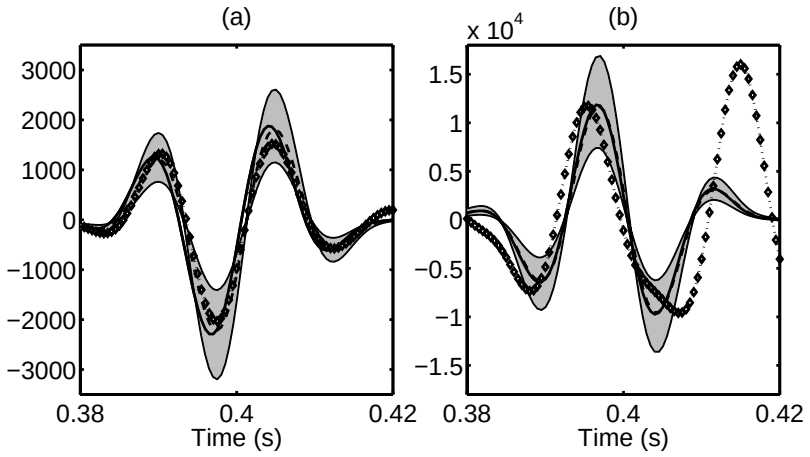

Figure 2.4: Sensitivity analysis for the variational formulation. The waveforms of the left (dashed) and right side (solid line) of equation (2.9) are shown for $\mathbf{w_1}$ (a) and $\mathbf{w_2}$ (b). The gray area in (a) illustrates the region for $\pm$ 20% perturbations in β, whereas (b) shows this region for $\pm$ 20% perturbations in α. The dotted curves show the effect of Gaussian noise (25 dB S/N ratio) added to the velocity recordings.

2002). This only requires the computation of first-order spatial wavefield derivatives, and is therefore expected to be more robust than wave-equation inversion. Both the free-surface conditions and wave-equation inversion are applicable to the complete wavefield, except the airwave.

As an alternative, we propose a new method which avoids the explicit computation of spatial wavefield derivatives and imposes no requirements on the maximum depth separation of geophones. This is achieved by assuming that the incident wavefield can be described by a single plane wave.

2.3 Propagator estimation

Our alternative approach to wave-equation inversion is based on propagator inversion. Trampert et al. (1993) proposed to estimate the S-wave velocity structure and the quality factor by analyzing the vertical SH propagator in the time domain. The propagator contains all information on the material properties between the free surface and the depth of a buried geophone, and can be estimated directly from recorded data. The S velocity can be constrained by determining the time lag between the peaks in the SH propagator. This time difference represents the two-way traveltime of an SH wave to depth Δz. The amplitude difference between the peaks can be used to infer the quality factor: downward continuation of upgoing waves result in increasing amplitudes, whereas the amplitudes of

downgoing waves decrease with depth.

We generalize this procedure to estimate the elastic P-SV propagator and illustrate a scheme to constrain near-surface P- and S-wave velocities based on waveform inversion of this P-SV propagator.

Assuming a plane wave solution for the wave equation, the plane wave at depth Δz can be written in the form

$$\mathbf{v}(t,x,\Delta z) = \mathbf{P}(t,x) * \mathbf{v}(t,x,0), \tag{2.19}$$

where

$$\mathbf{P} = \begin{pmatrix} P_{11} & P_{12} & P_{13} \\ P_{21} & P_{22} & P_{23} \\ P_{31} & P_{32} & P_{33} \end{pmatrix}. \tag{2.20}$$

and the asterisk ($*$) denotes a temporal convolution. For a homogeneous, isotropic, and elastic medium between the free surface and depth Δz, the propagator $\mathbf{P}$ is a function of the P-wave velocity α, the S-wave velocity β, and the horizontal slowness p. For a free-surface incident plane wave with slowness p propagating in the xz-plane, the theoretical propagator coefficients read (Aki and Richards, 2002):

$$\hat{P}_{11} = \beta^2 p^2 G_1^P + \left[(1-2\beta^2p^2)/2\right] G_1^S, \tag{2.21}$$
$$\hat{P}_{22} = G_1^S, \tag{2.22}$$
$$\hat{P}_{33} = \left[(1-2\beta^2p^2)/2\right] G_1^P + \beta^2 p^2 G_1^S, \tag{2.23}$$
$$\hat{P}_{13} = \left[p(1-2\beta^2p^2)/(2q_P)\right] G_2^P - \beta^2 p q_S G_2^S, \tag{2.24}$$
$$\hat{P}_{31} = \beta^2 p q_P G_2^P - \left[p(1-2\beta^2p^2)/(2q_S)\right] G_2^S, \tag{2.25}$$
$$\hat{P}_{12} = \hat{P}_{21} = \hat{P}_{23} = \hat{P}_{32} = 0, \tag{2.26}$$

where

$$G_1^P(t,p) = \left[\delta(t+q_P\Delta z) + \delta(t-q_P\Delta z)\right], \tag{2.27}$$
$$G_2^P(t,p) = \left[\delta(t+q_P\Delta z) - \delta(t-q_P\Delta z)\right], \tag{2.28}$$
$$G_1^S(t,p) = \left[\delta(t+q_S\Delta z) + \delta(t-q_S\Delta z)\right], \tag{2.29}$$
$$G_2^S(t,p) = \left[\delta(t+q_S\Delta z) - \delta(t-q_S\Delta z)\right]. \tag{2.30}$$

The vertical slownesses q_P and q_S are given by:

$$q_P = \left(\alpha^{-2} - p^2\right)^{1/2}, \tag{2.31}$$
$$q_S = \left(\beta^{-2} - p^2\right)^{1/2}. \tag{2.32}$$

Equations (2.27)–(2.30) contain the phase shifts for two-way extrapolation of the wavefield towards depth Δz. Positive phase shifts describe the propagation of downgoing waves to Δz, whereas negative phase shifts indicate propagation of upgoing waves to this depth.

The coefficients of the propagator matrix [equations (2.21)–(2.26)] can be interpreted as follows. Extrapolation of P-SV waves is described by P_{11}, P_{13}, P_{31} and P_{33}, whereas for SH waves it is given by P_{22}. The amplitude terms before G_1^P, G_1^S, G_2^P and G_2^S are wavefield decomposition filters: the wavefield is separated into P, SV and SH waves before extrapolating the recordings to depth Δz, which is given by the phase terms. Finally, summation of the extrapolated decomposed wavefield renders the total wavefield at depth Δz (Osen et al., 1999; Aki and Richards, 2002).

In the case of a non-attenuating medium, the extrapolation filters for elastic P-SV wave propagation can be obtained directly from the data exploiting symmetry properties of the filters: the theoretical expressions for the extrapolation filters show that P_{11}, P_{22}, and P_{33} are even functions around $t = 0$ and P_{13} and P_{31} are odd functions. Hence, the spectra of P_{11}, P_{22}, and P_{33} are entirely real, whereas the spectra of P_{13} and P_{31} are purely imaginary. These properties are used to estimate the extrapolation filters without prior information on α, β, and p. Equating real and imaginary parts of equation (2.19) in the frequency domain shows that the propagator coefficients are given by:

$$P_{11} = \{\Re[v_3(\omega,x,0)]\Re[v_1(\omega,x,\Delta z)] + \Im[v_3(\omega,x,0)]\Im[v_1(\omega,x,\Delta z)]\}\,/D(\omega), \tag{2.33}$$

$$P_{33} = \{\Re[v_1(\omega,x,0)]\Re[v_3(\omega,x,\Delta z)] + \Im[v_1(\omega,x,0)]\Im[v_3(\omega,x,\Delta z)]\}\,/D(\omega), \tag{2.34}$$

$$P_{13} = i\,\{\Re[v_1(\omega,x,0)]\Im[v_1(\omega,x,\Delta z)] - \Im[v_1(\omega,x,0)]\Re[v_1(\omega,x,\Delta z)]\}\,/D(\omega), \tag{2.35}$$

$$P_{31} = i\,\{\Re[v_3(\omega,x,0)]\Im[v_3(\omega,x,\Delta z)] - \Im[v_3(\omega,x,0)]\Re[v_3(\omega,x,\Delta z)]\}\,/D(\omega), \tag{2.36}$$

where

$$D(\omega) = \Re[v_3(\omega,x,0)]\Re[v_1(\omega,x,0)] + \Im[v_3(\omega,x,0)]\Im[v_1(\omega,x,0)]. \tag{2.37}$$

In these equations, $\Re[v(\omega,x,z)]$ denotes the real part of $v(\omega,x,z)$ and $\Im[v(\omega,x,z)]$ is the imaginary part of $v(\omega,x,z)$. Expressions for $\mathbf{P}(t,x)$ are found by taking the inverse Fourier transform of equations (2.33)–(2.36). Note that these symmetry properties break down for the P-SV case in the presence of attenuation. Then, only the SH case can be treated correctly (Trampert et al., 1993). The propagator estimation procedure remains valid in a vertically inhomogeneous medium.

The following procedure is used to stabilize the spectral divisions in equations (2.33)–(2.37). For arbitrary signals $F(\omega)$ and $D(\omega)$, the spectral division of $F(\omega)$ by $D(\omega)$ is given by:

$$G(\omega) = \frac{F(\omega)}{D(\omega)}. \tag{2.38}$$

Unfortunately, spectral division is numerically unstable both because signals are band-limited and due to the existence of low-amplitude notches in the spectrum. In practice,

the spectral ratio is estimated using the following technique (Helmberger and Wiggins, 1971; Langston, 1979):

$$G'(\omega) = \frac{F(\omega)D^*(\omega)}{\Phi_{DD}(\omega)}W(\omega), \tag{2.39}$$

where

$$\Phi_{DD} = \max\left\{D(\omega)D^*(\omega), c\max\left[D(\omega)D^*(\omega)\right]\right\}, \tag{2.40}$$

and $W(\omega)$ is a frequency window to limit the final frequency band in the estimated deconvolution. The complex conjugate of D is denoted by D^*. The function Φ_{DD} can be thought of as simply being the autocorrelation of $D(\omega)$ with any spectral notches filled to a level depending on the parameter c. The frequency windowing function $W(\omega)$ is a tapered window with cut-off frequencies set to the minimum and maximum frequencies for which

$$D(\omega)D^*(\omega) > c\max\left[D(\omega)D^*(\omega)\right]. \tag{2.41}$$

This criterion implies that the parameter c also controls the bandwidth of the spectral ratio $G'(\omega)$.

2.4 Propagator inversion

2.4.1 Half-space example

We shall first illustrate the inversion scheme for near-surface velocities with a half-space example. Synthetic data are computed using the Cagniard-de Hoop method (de Hoop and Van der Hijden, 1983). We restrict ourselves to the P-SV case since SH was fully treated by Trampert et al. (1993). The P-wave velocity is 600 m/s, the S-wave velocity is 200 m/s, and the density is 1600 kg/m^3. An explosive line source is located at 200 m depth and emits a 120 Hz Ricker wavelet. Multicomponent geophones are positioned at 50 m offset, one is located at the free surface and the second geophone is located at 1.0 m depth (Figure 2.5). Figure 2.6 shows traces recorded by these receivers.

The propagators P_{11}, P_{13}, P_{31} and P_{33} may be estimated from these data. Theoretical solutions for propagator filters are functions of α, β, and p. Figure 2.7(a) shows these filters for the given model parameters. Before comparing these propagator coefficients to the data-estimated propagator filters, it is necessary to limit the frequency band of these theoretical expressions to the same frequency band as used for the data-estimated propagator filters. The time domain expressions of the frequency windowing functions $W_{ij}(\omega)$ [equation (2.39)], where W_{ij} are the frequency windowing functions for propagator components P_{ij}, are shown in Figure 2.7(b). Figure 2.7(c) illustrates the data-estimated and band-limited theoretical propagators.

We choose to invert the propagator for near-surface velocities in the time domain. In this domain, the propagators can be interpreted as follows. The time delay between the

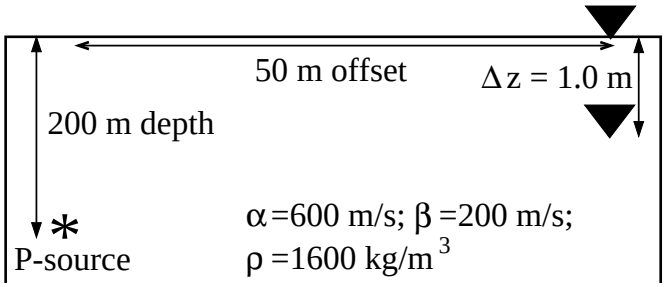

Figure 2.5: Geophone configuration and parameters of the half-space model.

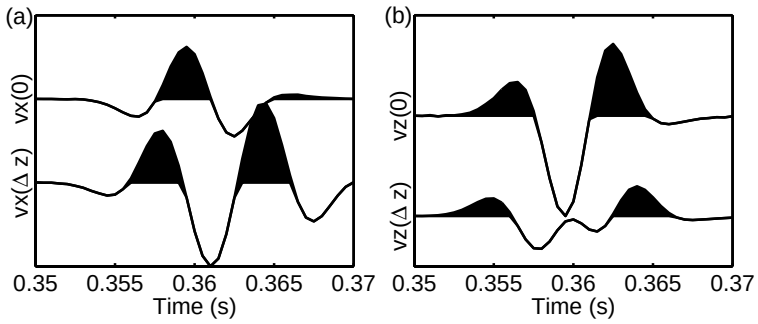

Figure 2.6: Synthetic traces of the particle velocity recorded by the surface and buried geophone shown in Fig. 2.5; (a) shows traces of v_x and (b) of v_z.

peaks in P_{11} and P_{33} gives the two-way vertical traveltime for SV and P waves, and the amplitudes of the propagator filters are controlled by the velocity structure between the free surface and depth Δz and the signal bandwidth. To constrain α, β, and p from the propagator waveforms, we define the following objective function:

$$E = E_{11} + E_{33} + E_{13} + E_{31}, \tag{2.42}$$

with

$$E_{ij} = \left\{ \sum_{t=t_1}^{t_2} \Big[P_{ij}(t,x) - \hat{P}_{ij}(t,x,\alpha,\beta,p) \Big]^2 \right\}^{1/2}. \tag{2.43}$$

The theoretical solution for the propagator filter component ij is denoted by $\hat{P}_{ij}(t,x,\alpha,\beta,p)$ and $P_{ij}(t,x)$ is the data-estimated propagator filter component ij. The objective function E is a function in a three-dimensional model space. Cross-sections of the objective function (Figure 2.8) show that perturbations in p have a relatively small influence on estimates of α and β.

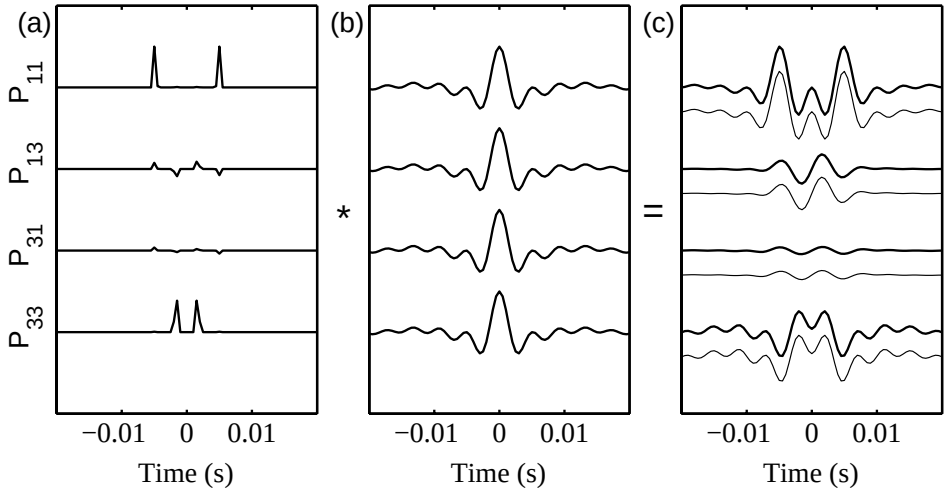

Figure 2.7: Propagator fitting procedure for the data displayed in Fig. 2.6. Given estimates for α, β, and p, theoretical solutions for the wavefield extrapolation filters can be computed (a). In practice, data are band-limited, and therefore this theoretical solution cannot be compared directly to the estimated filters. (b) shows the time-domain expressions of frequency filters which limit the solution to the frequency band in which the spectral division was performed. A convolution of the theoretical solution in (a) with the filter shown in (b) allows a comparison to the data-estimated propagator. (c) shows that there is a good agreement between the theoretical (thin lines) and data-estimated propagator filters (thick lines). The stabilization factor $c = 1 \cdot 10^{-3}$.

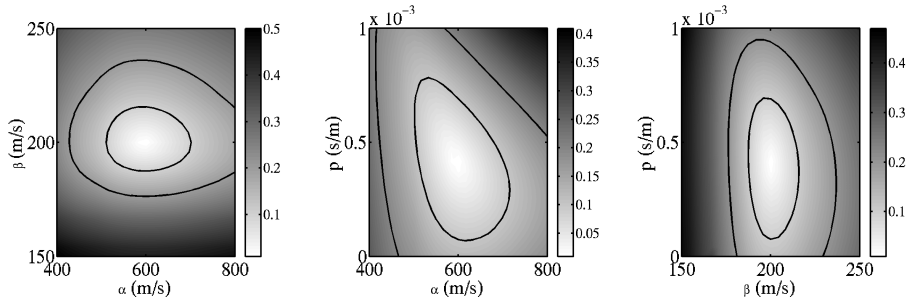

Figure 2.8: Cross-sections intersecting the minimum of the objective function E. Contours are drawn for $E = 0.10$ and $E = 0.20$.

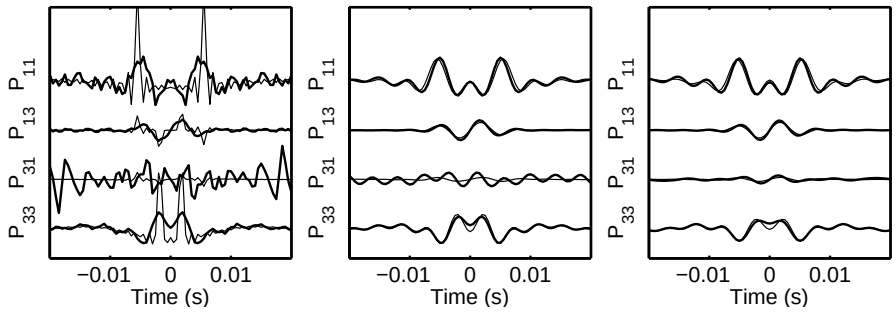

Figure 2.9: Effect of the stabilization factor c on noise-perturbed propagator filters. The S/N ratio is 25 dB. The propagator filters are computed for $c = 10^{-4}$ (left), $c = 10^{-3}$ (center) and $c = 10^{-2}$ (right). The thin lines are the band-limited theoretical solutions and the thick lines the data-estimated propagators. The amplitudes of each filter are normalized to the solution for $c = 10^{-4}$. For increasing values of c, the noise is effectively reduced.

So far, we considered noise-free data. The data-estimated propagator filters for recorded data perturbed by 25 dB uncorrelated Gaussian noise are shown in Figure 2.9. These are compared to the theoretical filters for different values of the stabilization factor c [equation (2.40)], namely $c = 10^{-4}$, $c = 10^{-3}$ and $c = 10^{-2}$. For an increasing value of c, the effect of noise is reduced in the propagator filters. Furthermore, the frequency band is more limited for a higher $c-$value. The filters are smoothed and contain less energy.

We estimated the relative variations in α, β, and p for different noise levels and c-values. To quantify the effect of noise, we define the relative root-mean-square error RMS in α by:

$$RMS(\alpha) = \frac{1}{\alpha_0}\left[\frac{\sum_{i=1}^{N}(\alpha_i - \alpha_0)^2}{N}\right]^{1/2}, \tag{2.44}$$

with α_0 the model P-wave velocity and α_i the estimated P-wave velocities, which are found by minimizing E in equation (2.43). Similar expressions are defined for the relative RMS error in β and p. For each noise level, experiments were conducted 1000 times ($N = 1000$) with different manifestations of Gaussian noise. The minimum of the objective function E was determined using a forward search method. Figure 2.10 shows that the estimates of α, β, and p are most robust for $c = 10^{-2}$: c clearly stabilizes noise very systematically. Furthermore, α and β are better constrained than p, which implies that relative errors in estimates of p have less influence on estimates of the other parameters than do relative errors of similar magnitude in either α or β.

In addition to random errors, the effect of position and orientation errors of the geophones within the recording pattern is investigated. We only consider misorientation in the xz-plane, described by rotation angle θ (positive for rotation in clockwise direction).

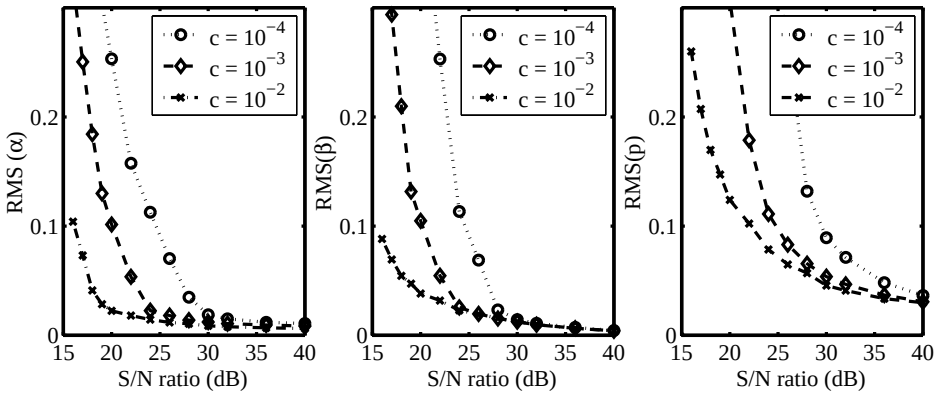

Figure 2.10: Uncertainties in estimates for α, β and p for different S/N ratios and $c-$values.

The effects of misorientation and mislocation are quantified with a relative error e. The relative error in α is given by:

$$e(\alpha) = (\alpha - \alpha_0)/\alpha_0. \tag{2.45}$$

Similar expressions are used for relative errors in β and p. Figure 2.11(a) shows the relative error in estimates for α, β, and p due to misorientation of the geophone located at the free surface. The errors in α and β are small compared to relative errors in p. Large errors are found for θ close to the angle of incidence. In this example, there are only free-surface incident P-waves. This rotation causes the energy on the horizontal recording and thus on the denominator $D(\omega)$ [equation (2.37)] to be minimized. As a consequence, the spectral divisions [equations (2.33)–(2.36)] become unstable. In case of near-surface structure, we do not expect such a rapidly increasing error, because in that case both P and S waves will be recorded.

The errors caused by misorientation of the buried geophone is shown in Figure 2.11(b). Here, $e(\alpha)$ and $e(\beta)$ remain small, because $\mathbf{v}(\omega, \Delta z)$ does not contribute to the denominator $D(\omega)$. Finally, the effect of vertical mislocation of the buried geophone is illustrated in Figure 2.11(c). To do so, the values for Δz are changed in the inversion procedure; The relative change in the depth for the buried geophone $\Delta z_r = (\Delta z - \Delta z_0)/\Delta z_0$, with Δz_0 the true depth of the buried geophone. There is a linear relationship between errors in Δz and estimated velocities. This implies that the phase contains most information on the velocities.

It is difficult to make a fair comparison between wave-equation inversion techniques and propagator inversion. Wave-equation inversion uses the *amplitudes* in the wave-equation [equation (2.1)] to constrain α and β. This requires measurement of spatial and temporal wavefield derivatives by a dense 3D geophone configuration, with a spatial separation on a sub-wavelength scale. Propagator inversion, on the other hand, uses mainly

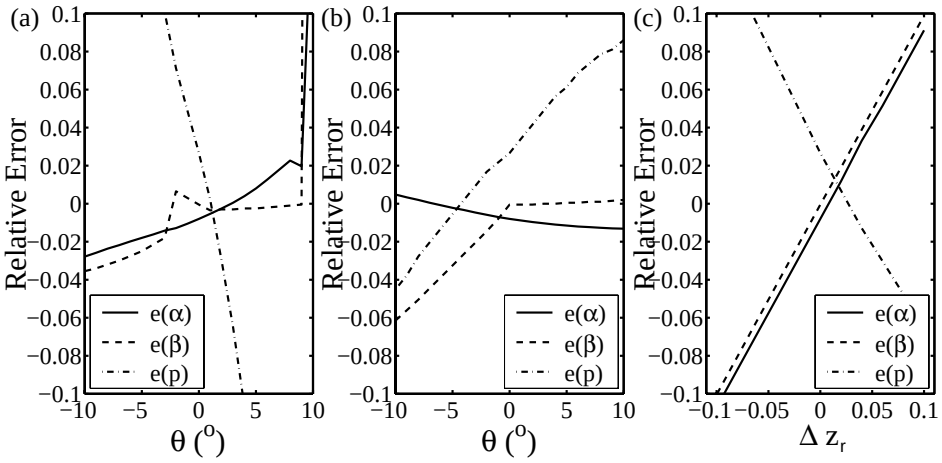

Figure 2.11: Errors in velocity estimates due to mislocation and misoriention. (a) misorientation in xz-plane of surface geophone, (b) misorientation in xz-plane of buried geophone, and (c) vertical mislocation of buried geophone. The stabilization factor $c = 10^{-3}$.

phase information. To estimate time differences reliably, the depth separation between geophones needs to be larger than those used for wave-equation inversion. Therefore, we used different depths for the buried geophone and different dominant frequencies for the source wavelet.

The obtained results suggest that propagator inversion is less sensitive to both random and deployment related data perturbations. For a S/N ratio of 25 dB, propagator inversion gives no error in α and β, whereas for the wave-equation inversion techniques Figures 2.3 and 2.4 indicate more than 20% deviations in estimates for α, while β is still well resolved. Furthermore, Figure 2.11 demonstrated that propagator inversion is tolerant to at least 5° misorientations and 5% vertical mislocations of individual geophones. Derivative operators on the other hand are particularly sensitive to random misorientations of geophones. Muijs et al. (2002) showed that computation of divergence and curl with dense 3D recording geometries requires that the orientations of all geophones are accurate within 2°. This criterion needs to be satisfied as well for wave-equation inversion techniques.

Although propagator inversion is tolerant to measurement errors, it is questionable whether this is the dominant source of errors for this method, since a single slowness assumption is implicit in propagator estimation and inversion. Wave-equation inversion techniques do not have this assumption and are applicable to the complete wavefield. In the following experiments, we investigate if propagator inversion is accurate in a model with near-surface structure.

2.4.2 Low velocity layer example

The second experiment is performed in a model with a near-surface low velocity layer. Reverberations in this layer result in multiple arrivals. The near-surface layer is 5 m thick with $\alpha = 600$ m/s, $\beta = 200$ m/s, and $\rho = 1600$ kg/m^3. The parameters of the underlying half-space are: $\alpha = 1500$ m/s, $\beta = 400$ m/s, and $\rho = 1800$ kg/m^3. The P source is located at 100 m depth and emits a 120 Hz Ricker wavelet (see Figure 2.12). The receiver group is similar to the previous experiment. Synthetic data are computed with a reflectivity method (Kennett, 1983). The recorded synthetic traces are shown in Figure 2.13. These clearly show the multiple arrivals due to interfering waves in the near-surface low velocity layer.

The data-estimated propagators are again compared to the theoretical propagators (Figure 2.14). The latter were computed for the horizontal slowness of the first break, which is $3.1 \cdot 10^{-4}$ s/m. Due to the multiple arrivals (multiple horizontal slownesses), there is not an exact match between the theoretical and data-estimated propagators. The energy in the propagator filters decays for higher values of c. For too high a c-value, the fit between the theoretical and data-estimated propagator deteriorates. This can be attributed to the stabilization of internal notches in $D(\omega)$, whereas the theoretical propagator is not compensated for the energy decay in $\mathbf{P}$ due to this stabilization.

Cross-sections of misfit functions using $c = 10^{-3}$ are shown in Figure 2.15. The minimum is located close to the model velocities, whereas the estimated p tends to be smaller than that of the first break, namely around $2.8 \cdot 10^{-4}$ s/m. Waves reverberating in the low-velocity layer arrive at smaller angles of incidence, thus the estimated p can be regarded as some averaged value over all these arrivals.

Figure 2.16 illustrates the effects of added noise on velocity and slowness estimation.

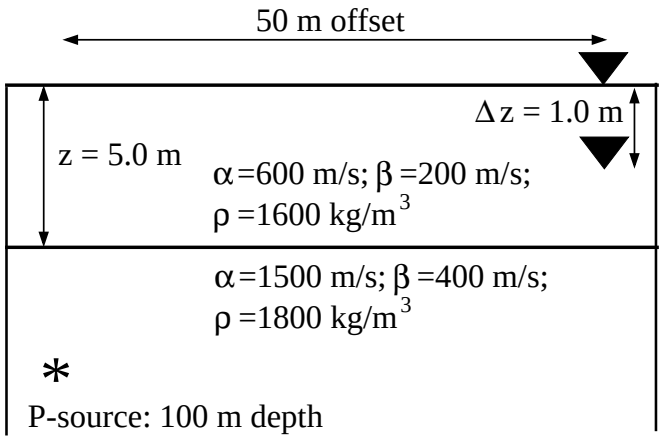

Figure 2.12: Model and geophone configuration for experiment with near-surface low velocity layer.

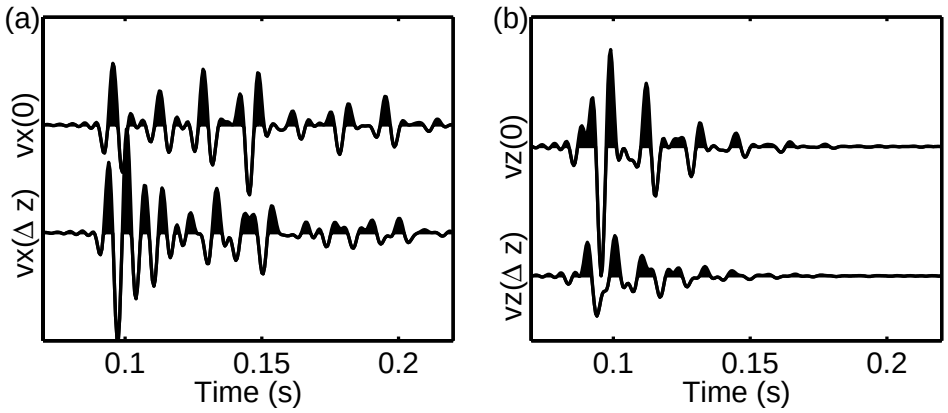

Figure 2.13: Synthetic traces recorded by the geophone configuration displayed in Fig. 2.12. Shown are recordings of v_x (a) and v_z (b).

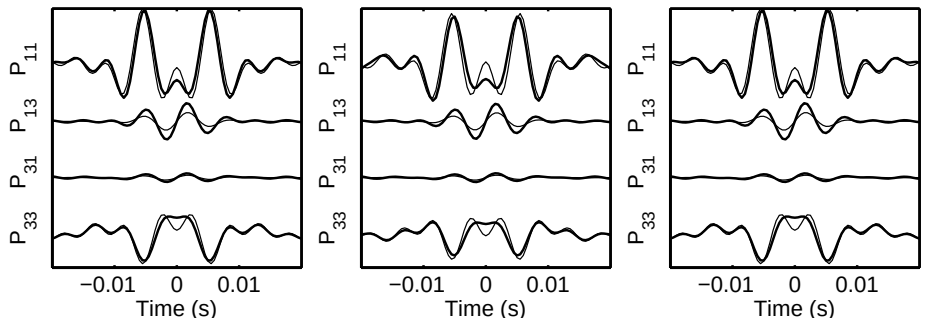

Figure 2.14: Effect of the stabilization factor c on estimated propagators: $c = 10^{-4}$ (left), $c = 10^{-3}$ (center), and $c = 10^{-2}$ (right). The thin lines are the theoretical solutions computed with the horizontal slowness of the first break and the thick solid lines are the propagators estimated from the data. Traces are normalized with respect to the $c = 10^{-4}$ curves.

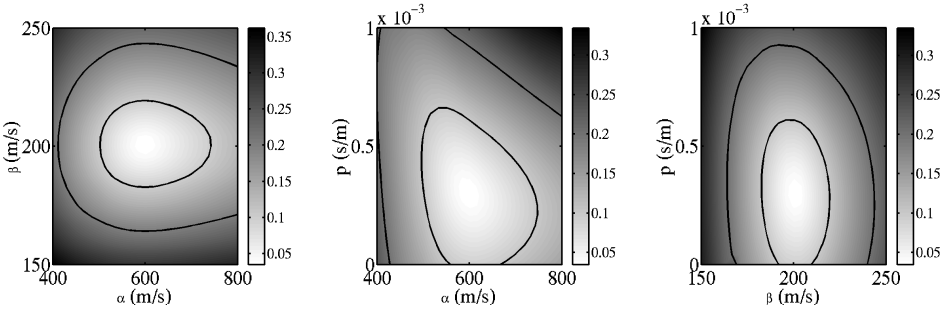

Figure 2.15: Cross-sections intersecting the minimum of the objective function E for the low-velocity layer model. Contours are drawn for $E = 0.10$ and $E = 0.20$, and $c = 10^{-3}$.

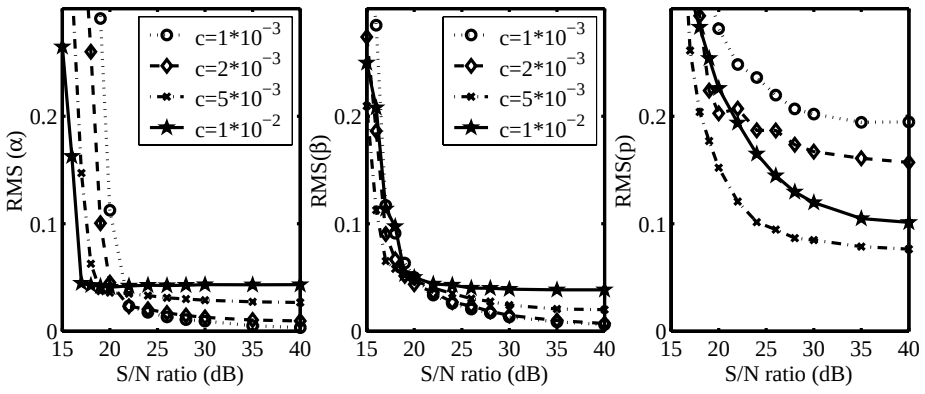

Figure 2.16: Uncertainty in estimates for α, β, and p for different $c-$values as a function of S/N ratio. The estimated horizontal slowness is compared to the slowness of the direct arrival.

For high S/N ratios, the estimates for α and β do not exactly converge for $c = 5 \cdot 10^{-3}$ and $c = 10^{-2}$, as was suggested by Figure 2.15 as well. The estimated horizontal slowness differs from that of the direct arrival and varies for different values of c. As in the half-space example, c stabilizes the effects of noise. Reliable estimates for α and β are obtained for S/N ratios down to approximately 18 dB.

2.4.3 Structure between surface and buried geophone

A critical assumption in the propagator inversion scheme is that the medium between the surface and buried geophones is homogeneous. However, according to the classical Hertz-Mindlin model (Mindlin, 1949), velocities increase with confining pressure and thus with depth, especially in the top few meters. This also has been observed in field experiments (e.g. Bachrach et al., 2000). Here, we consider a model with a large velocity gradient close to the free surface. The velocity gradient decreases with depth (Figure 2.17). The gradient model is parameterized by 0.02 m thick layers. Synthetic data are computed using a reflectivity method (Kennett, 1983). The explosive line source is located at 100 m depth and 50 m offset, and emits a 120 Hz Ricker wavelet. The buried geophone is located at 1.0 m depth. Figure 2.18 shows the synthetic traces for both the surface and buried multicomponent geophones. Data-estimated propagators are shown in Figure 2.19. These are compared to theoretical solutions with effective medium velocities, which lower and upper bounds are given by the Reuss and Voigt average velocities (Wang and Nur, 1992). For the top 1.0 m, the Reuss velocities are $\alpha^- = 259$ m/s and $\beta^- = 101$ m/s, and the Voigt velocities are $\alpha^+ = 284$ m/s and $\beta^+ = 105$ m/s, respectively. The average value of the Voigt and Reuss velocities is used to compute the theoretical propagator. Although the propagator waveforms do not exactly match, the time lags of the peaks are similar. Figure 2.20 shows cross-sections of the misfit function. Both α and β are well constrained, whereas p cannot be resolved. The estimated velocities are $\alpha = 272 \pm 8$ m/s

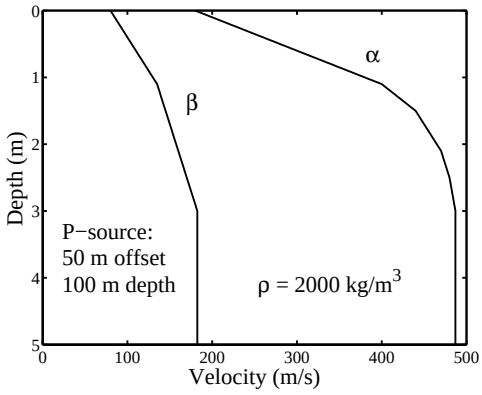

Figure 2.17: Gradient velocity model and source location

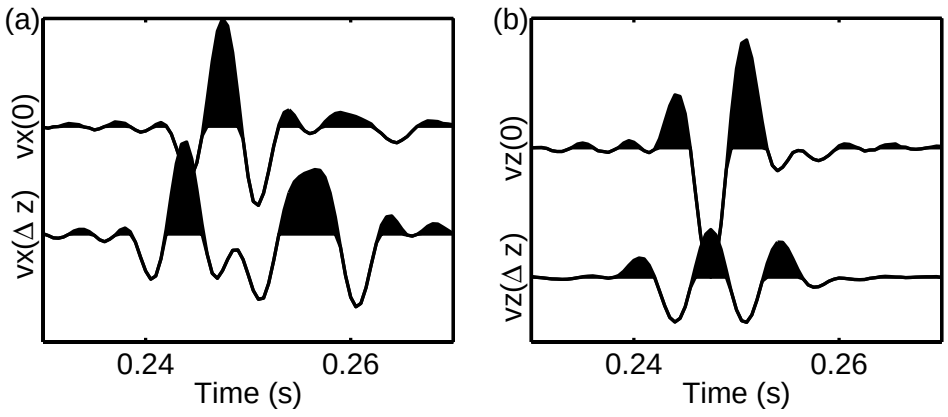

Figure 2.18: Synthetic data recorded in the gradient model at 50 m offset. The buried geophone is located at 1.0 m depth and the P source at 100 m depth. Shown are recordings of v_x (a) and v_z (b).

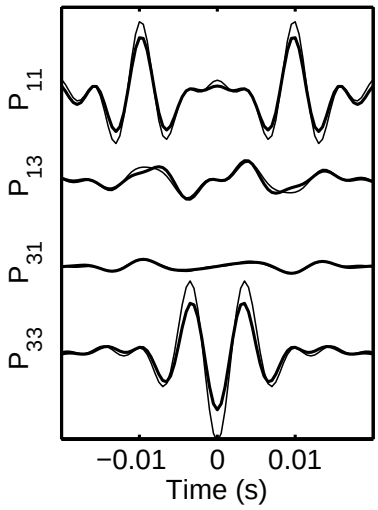

Figure 2.19: Data-estimated and theoretical propagators in the gradient model. The theoretical propagator is computed using the average value of the Voigt and Reuss effective medium velocities: $\alpha = 272$ m/s and $\beta = 103$ m/s, $p = 8.75 \cdot 10^{-4}$ (s/m) and $c = 10^{-3}$.

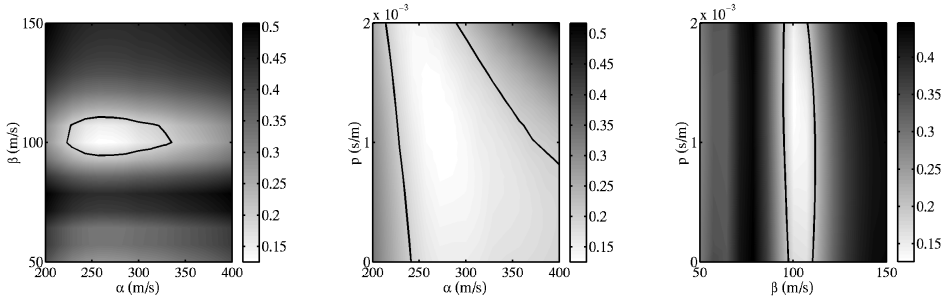

Figure 2.20: Cross-sections through the minimum of the objective function E for the gradient model. A contour is drawn for $E = 0.20$, and $c = 10^{-3}$.

and $\beta = 102.8 \pm 0.6$ m/s. These values are obtained by performing repeated experiments ($N = 1000$) with different manifestions of random noise ($S/N = 25$ dB), determining the minimum of the objective function E with a forward search method, and using the average and standard deviation of all these estimates. The obtained velocities fall within the Voigt and Reuss bounds for effective medium velocities.

2.5 Discussion

Three methods to estimate near-surface properties were evaluated in this paper. The first two methods are based on inversion of the wave equation, whereas the third method inverts wavefield propagator filters for near-surface velocities. A fundamental difference between the methods is that wave-equation inversion schemes use amplitude information to constrain α and β. By changing α and β, the amplitudes in the wave-equation change, not the phase. On the other hand, propagator inversion uses predominantly phase information to constrain α and β, i.e., the time lags of the peaks in the propagator coefficients are controlled by the wave velocities.

These sensitivities for either predominantly amplitude information or phase information result in a different optimum experimental setup. Wave-equation inversion techniques require the measurement of spatial wavefield derivatives, with a spatial geophone spacing on a sub-wavelength scale. Propagator inversion on the other hand uses mainly phase information. To estimate time differences accurately, both the depth separation of the surface and the buried geophone and the bandwidth of the recorded signal have to be larger. For this reason, we used different configurations, different frequencies and a different depth of the buried geopone, to compare wave-equation inversion techniques to propagator inversion.

Before fitting the waveforms in the wave-equation inversion schemes, either spatial wavefield derivatives or interpolants need to be evaluated. For an accurate implementation of these methods, the spacing between geophones must be sufficiently close, approx-

imately $1/6$ of the effective wavelength. Since the wavelength depends on the material properties, some prior knowledge has to be available to design the receiver group.

Propagator inversion on the other hand has no wavelength constraints on the maximum allowed separation of geophones. Therefore, the method may be applicable to borehole recordings. This has been demonstrated for the SH case by Trampert et al. (1993). However, in the P-SV case we only treated the elastic situation, whereas attenuation has to be included in the formulation for borehole applications. The near-surface velocity estimates presented in this paper are not affected by attenuation, because the geophone separation $\Delta z \ll \lambda$.

However, for a geophone buried at too shallow a depth, propagator inversion cannot resolve the wave velocities. Then, small errors in the phase will cause large uncertainties in the estimated velocities, especially for α. These uncertainties are reduced by increasing the depth of the buried geophone (Van den Berg et al., 2003). The minimum depth for the buried geophone depends on the frequency band, the angle of incidence, on α, and on the time sampling rate.

The wave-equation inversion schemes use the complete wavefield as input signal. Any event which satisfies the wave equation provides constraints on the near-surface properties. The main sources of error which need to be dealt with are deployment related errors. Muijs et al. (2002) demonstrated that errors such as misorientation and mislocation of individual geophones significantly affect estimates of spatial wavefield derivatives. Correction schemes need to be developed to compensate for these effects. Propagator inversion on the other hand avoids the explicit computation of spatial wavefield derivatives. As a consequence, this method is less sensitive to these types of errors.

In contrast to wave-equation inversion techniques, a single slowness assumption is required to construct and invert the propagator filters. As a consequence, a part of the data containing arrivals that are isolated in time needs to be selected before this method can be applied. We demonstrated, however, that in a medium with a near-surface low velocity layer, estimates for α and β are not significantly affected by signal-generated reverberations, and that in a model with a strong velocity gradient, effective medium parameters are obtained.

The following strategies for propagator inversion can be developed combining data of different shots. First, if the horizontal slownesses in selected data show little variation for different shot points, it is possible to reduce effects of noise by stacking the estimated propagator filters.

Second, propagator inversion can be formulated without requiring the isolation of an event which can be approximated by a single plane wave. When using a dense source array, the frequency-wavenumber spectra can be computed for common receiver gathers of both the surface geophone and the geophone at depth. Consequently, propagator filters can be determined for each wavenumber or horizontal slowness individually by a spectral division of these two spectra, Thus, propagator inversion is potentially applicable to the complete wavefield. However, difficulties might arise due to lateral variations in near-surface material parameters and poor repeatability of the source.

Synthetic tests have been performed in two dimensions, whereas three-dimensional wave propagation has to be considered in the field. Applications in the field require a dif-

ferent acquisition geometry for wave-equation inversion. Wave-equation inversion techniques require a 2D patch of 4×4 receivers at the surface and a buried geophone in the center at this geophone group. Then, all spatial and temporal derivatives or interpolants can be computed. Propagator inversion requires the separation of P-SV waves from SH waves, hence rotation of the recordings in the inline/crossline direction is required. Furthermore, propagator inversion is aided by an estimate for the horizontal slowness in the inline direction, and therefore a cross pattern of receivers at the surface is recommended for field applications. The general characteristics of the considered methods do not change in three-dimensions, and therefore the presented two-dimensional synthetic results will apply to the three-dimensional situation.

2.6 Conclusions

We evaluated three methods to estimate local near-receiver material properties. A fundamental difference between the methods is that the wave-equation inversion schemes constrain the P-wave and S-wave velocities by matching amplitudes in the wave-equation, whereas propagator inversion constrains the wave velocities using predominantly phase information, i.e., with the traveltime from the free surface to the depth of the buried geophone. As a consequence, wave-equation and propagator inversion have different optimum receiver configurations. For wave-equation inversion, the configuration needs to be designed to allow the measurement of spatial wavefield derivatives or interpolants, whereas the configuration in propagator inversion must allow a reliable measurement of a phase difference.

Both the derivative and the integral formulation for wave-equation inversion are almost equally sensitive to the effects of measurement errors. If a configuration with more than one buried geophone would have been allowed, an interpolation scheme may be developed which is less sensitive to these type of errors. However, these configurations are not convenient for practical applications, and therefore were not considered.

Propagator inversion has two advantages and one disadvantage over wave-equation inversion schemes. First, instead of a 3D receiver configuration, only two geophones are required, one positioned at the surface and one buried. Second, this scheme avoids the explicit evaluation of spatial wavefield derivatives or interpolants and therefore it is less sensitive to deployment related errors. On the other hand, this technique implicitly assumes that a data window containing arrivals with a similar horizontal slowness can be isolated in the recorded data, whereas wave-equation inversion schemes are applicable to nearly the complete recordings. Synthetic experiments were performed to assess the consequences of the single slowness assumption in propagator inversion. These experiments demonstrated that the method is robust with respect to signal-generated reverberations, and in case of a near-surface velocity gradient, results are consistent with effective medium velocities, which upper and lower bounds are given by the Voigt and Reuss averaged velocities. Moreover, when using a shot array, propagator inversion could be formulated without the plane wave assumption, and therefore, it is potentially applicable to the complete wavefield.

Chapter 3

Subsonic near-surface *P*-velocity and low *S*-velocity observations using propagator inversion

Abstract

Detailed knowledge of near-surface P- and S-wave velocities is important for processing and interpreting multicomponent land seismic data, because (i) the entire wavefield passes through, and is influenced by the near-surface soil conditions, (ii) both source repeatability and receiver coupling also depend on these conditions, and (iii) near-surface P and S velocities are required for wavefield decomposition and demultiple methods. However, it is often difficult to measure these velocities with conventional techniques because sensitivity to shallow wave velocities is low, and because of the presence of sharp velocity contrasts or gradients close to the Earth's free surface. We demonstrate that these near-surface P- and S-wave velocities can be obtained using a propagator inversion. This approach requires data recorded by at least one multicomponent geophone at the surface and an additional multicomponent geophone at depth. The propagator between them then contains all information on the medium parameters governing wave propagation between the geophones at the surface and at depth. Hence, inverting the propagator gives local estimates for these parameters. This technique has been applied to data acquired in Zeist, the Netherlands. The near-surface sediments at this site are unconsolidated sands with a thin vegetation soil on top, and the sediments considered are located above the groundwater table. A buried geophone was positioned 1.05 m beneath receivers on the surface. Propagator inversion yielded low near-surface velocities, namely 270 $\pm$ 15 m/s for the compressional wave velocity, which is well below the sound velocity in air, and 150 $\pm$

This chapter has been published as: Van Vossen, R., Curtis, A. and Trampert, J., Subsonic near-surface P-velocity and low S-velocity observations using propagator inversion, *Geophysics*, in press.

9 m/s for the shear velocity. Higher P-wave velocity estimates were obtained with dispersion analysis for guided waves. This apparent discrepancy can be explained by the different depth sensitivities of the methods, indicating that velocities increase with depth in the near-surface low velocity layer. As a result, the wave velocities at the measurement interface can only be obtained using either a 3D geophone configuration or with an additional high-frequency experiment. We suspect that this is the reason that subsonic near-surface P-wave velocities are not commonly observed.

3.1 Introduction

Strong near-surface velocity contrasts are often encountered in land seismic surveys. Both P- and S-wave velocities may increase by nearly an order of magnitude at the interface defining the top of the bedrock, and P-velocities increase up to 100 % across the top depth of total water saturation (Stümpel et al., 1984; Goforth and Hayward, 1992).

Detailed knowledge of near-surface velocities is essential for engineering applications, groundwater and environmental projects (Ward, 1990). Furthermore, this is required for correctly processing and interpreting (multicomponent) land data. For instance, the near-surface soil conditions have a significant influence on the source wavelet and radiation pattern (Kähler and Meissner, 1983; Aritman, 2001). Also, wavefield decomposition, which enables independent interpretation of up- and downgoing P and S waves, requires the free-surface reflectivity to be known accurately (e.g. Dankbaar, 1985; Wapenaar et al., 1990; Robertsson and Curtis, 2002). Wavefield decomposition is a prerequisite for demultiple (Verschuur et al., 1992). Demultiple is especially important in media with a near-surface low velocity layer which may act as a waveguide in which energy may propagate over long distances with little loss due to geometrical spreading. This could mask reflections from a deeper target (Hunter et al., 1984; Robertsson et al., 1996). Demultiple methods remove these guided waves.

While shallow material properties are especially important for processing and interpretation of multicomponent seismic data, near-surface wave velocities usually cannot be resolved with an acquisition geometry designed for imaging deeper structure. Detailed information can, however, be obtained with shallow, high-resolution, reflection and refraction experiments (Doornenbal and Helbig, 1983; Hunter et al., 1984; Steeples and Miller, 1990). These techniques use arrays of closely spaced geophones and high frequencies to obtain detailed images of the shallow subsurface.

Subsonic P-wave velocities have been observed with these shallow high resolution seismic experiments by analyzing moveout velocities close to source (Birkelo et al., 1987; Bachrach and Nur, 1998; Bachrach et al., 1998; Baker et al., 1999), whereas they are not commonly observed using conventional seismic techniques. This is a consequence of different depth sensitivities of these methods, combined with a near-surface velocity gradient due to increasing confining pressure. A drawback of estimating near-source moveout velocities is that the complexity of the near-source field requires careful processing and interpretation of these types of data to avoid misinterpretation of recorded events (Michaels, 2002).

Recently, Curtis and Robertsson (2002) introduced a technique for estimating local near-surface velocities using a 3D geophone configuration. Geophones are not only deployed at the surface, but also at shallow depths to enhance the imaging of the near-surface, without having to perform an additional high-resolution experiment. With the proposed 3D geophone configuration, spatial wavefield derivatives can be approximated, allowing inversion of the wave equation for near-surface P- and S-wave velocities (Curtis and Robertsson, 2002). An advantage of this method is that it is applicable to the complete wavefield. However, a drawback is the sensitivity to deployment related errors (Muijs et al., 2002).

We present results from a technique referred to as propagator inversion (Trampert et al., 1993; Van Vossen et al., 2004c). This technique also uses a 3D geophone configuration to determine near-surface P- and S-wave velocities, but avoids the explicit computation of spatial wavefield derivatives, and is therefore less sensitive to deployment related errors. Moreover, it does not require the measurement and interpretation of moveout velocities in the near-source region, and it can be incorporated in a seismic survey for imaging deeper structure without having to perform an additional high-resolution experiment.

3.2 Propagator estimation from data

Propagator matrices were introduced in seismology by Thomson (1950) and Haskell (1953) and generalized by Gilbert and Backus (1965). These describe the propagation of plane waves through a horizontally layered medium. Throughout this paper, the free-surface is used as a reference level. The propagator can then be interpreted as a wavefield extrapolation filter. Application of the propagator to the recorded wavefield at the free surface gives the wavefield at depth Δz.

Trampert et al. (1993) introduced SH propagator inversion to obtain the SH velocity structure and the quality factor in a borehole. This propagator can be obtained from the recorded data by taking the spectral ratio of a downhole record over a surface record. It is completely determined by the medium parameters governing wavefield propagation between these two records. Recently, Van Vossen et al. (2004c) formulated propagator estimation for the elastic P-SV case. We briefly review this concept before we discuss the inversion scheme for near-surface material parameters.

In an isotropic medium, the propagator naturally decomposes into SH and coupled P-SV waves. The anelastic SH case is fully treated by Trampert et al. (1993). We only review the elastic P-SV case here. We denote the inline particle velocity component by v_1 and the vertical component by v_3. The full propagator is a 4×4 matrix, and the boundary conditions state that the free-surface is stress-free, so that the wavefield at depth Δz is related to the wavefield recorded at the free surface ($z = 0$) by:

$$\begin{pmatrix} v_1(\omega, x, \Delta z) \\ v_3(\omega, x, \Delta z) \end{pmatrix} = \begin{pmatrix} P_{11} & P_{13} \\ P_{31} & P_{33} \end{pmatrix} \begin{pmatrix} v_1(\omega, x, 0) \\ v_3(\omega, x, 0) \end{pmatrix}. \tag{3.1}$$

For an elastic, homogeneous medium, with P velocity α and S velocity β, the propagator

coefficients read in the time domain (Aki and Richards, 2002; Van Vossen et al., 2004c):

$$P_{11} = \beta^2 p^2 G_1^P + \left[\left(1 - 2\beta^2 p^2\right)/2\right] G_1^S, \quad (3.2)$$

$$P_{33} = \left[\left(1 - 2\beta^2 p^2\right)/2\right] G_1^P + \beta^2 p^2 G_1^S, \quad (3.3)$$

$$P_{13} = \left[p\left(1 - 2\beta^2 p^2\right)/(2q_P)\right] G_2^P - \beta^2 p q_S G_2^S, \quad (3.4)$$

$$P_{31} = \beta^2 p q_P G_2^P - \left[p\left(1 - 2\beta^2 p^2\right)/(2q_s)\right] G_2^S, \quad (3.5)$$

where

$$G_1^P = \delta(t + q_P \Delta z) + \delta(t - q_P \Delta z), \quad (3.6)$$

$$G_2^P = \delta(t + q_P \Delta z) - \delta(t - q_P \Delta z), \quad (3.7)$$

$$G_1^S = \delta(t + q_S \Delta z) + \delta(t - q_S \Delta z), \quad (3.8)$$

$$G_2^S = \delta(t + q_S \Delta z) - \delta(t - q_S \Delta z). \quad (3.9)$$

The horizontal slowness is denoted by p, and the vertical slownesses q_P and q_S are:

$$q_P = \left(\alpha^{-2} - p^2\right)^{1/2}, \quad (3.10)$$

$$q_S = \left(\beta^{-2} - p^2\right)^{1/2}. \quad (3.11)$$

These theoretical expressions show that P_{11} and P_{33} are symmetric around $t = 0$, whereas P_{13} and P_{31} are antisymmetric around $t = 0$. Thus, in the frequency domain P_{11} and P_{33} are entirely real, and P_{13} and P_{31} are purely imaginary. As a result, we can directly estimate the components of $P_{ij}(\omega)$ by equating real and imaginary parts in equation (3.1). In the following, we denote the propagator coefficients estimated from the data with $\tilde{\mathbf{P}}(\omega)$. The explicit expressions for estimating $\tilde{\mathbf{P}}(\omega)$ are:

$$\tilde{P}_{11} = \{\Re[v_3(\omega,0)]\Re[v_1(\omega,\Delta z)] + \Im[v_3(\omega,0)]\Im[v_1(\omega,\Delta z)]\}/D(\omega), \quad (3.12)$$

$$\tilde{P}_{33} = \{\Re[v_1(\omega,0)]\Re[v_3(\omega,\Delta z)] + \Im[v_1(\omega,0)]\Im[v_3(\omega,\Delta z)]\}/D(\omega), \quad (3.13)$$

$$\tilde{P}_{13} = i\{\Re[v_1(\omega,0)]\Im[v_1(\omega,\Delta z)] - \Im[v_1(\omega,0)]\Re[v_1(\omega,\Delta z)]\}/D(\omega), \quad (3.14)$$

$$\tilde{P}_{31} = i\{\Re[v_3(\omega,0)]\Im[v_3(\omega,\Delta z)] - \Im[v_3(\omega,0)]\Re[v_3(\omega,\Delta z)]\}/D(\omega), \quad (3.15)$$

with the denominator $D(\omega)$ given by:

$$D(\omega) = \Re[v_3(\omega,0)]\Re[v_1(\omega,0)] + \Im[v_3(\omega,0)]\Im[v_1(\omega,0)]. \quad (3.16)$$

In these equations $\Re[v_1(\omega,\Delta z)]$ is the real part of $v_1(\omega,\Delta z)$, $\Im[v_1(\omega,\Delta z)]$ is the imaginary part, and i denotes the imaginary unit $\sqrt{-1}$. Note that the symmetry properties used to obtain explicit expressions for the propagator filters break down in the visco-elastic case. Then, only the SH propagator can be directly obtained from the data (Trampert et al., 1993).

Van Vossen et al. (2004c) computed $\tilde{\mathbf{P}}$ with a stabilized spectral division using the so-called water level method (Helmberger and Wiggins, 1971). Stabilization is required due to a limited bandwidth of $D(\omega)$, and also interfering waves may introduce internal notches in $D(\omega)$. However, a problem associated with this method is that the amount of

stabilization can influence the estimates for the propagator (Ammon, 1991). This may affect the inversion results as well (Van Vossen et al., 2004c). To avoid these problems, we decided to implement the spectral divisions in the time domain instead using a Wiener deconvolution scheme. Either symmetric ($\tilde{P}_{11}$ and $\tilde{P}_{33}$) or antisymmetric filters ($\tilde{P}_{13}$ and $\tilde{P}_{31}$) around $t = 0$ are constructed with N independent coefficients. Details on the implementation of the acausal Wiener deconvolution can be found in Appendix B.

3.3 Propagator inversion

In the previous section we showed that $\tilde{\mathbf{P}}$ can be obtained from data recorded by one surface geophone and one at depth. In this section, we outline the inverse procedure for estimating the near-surface velocities α and β from $\tilde{\mathbf{P}}$.

A flow diagram for the inverse problem is shown in Figure 3.1. The 3D receiver configuration used for the Zeist field experiment, conducted to test propagator estimation and inversion, is shown in Figure 3.2. We discuss this experiment in detail in the next section. The configuration has multicomponent geophones positioned in a cross-shape at the surface. Two geophones are buried at the center of the receiving group. Strictly speaking, propagator estimation only requires one multicomponent geophone positioned at the surface and a second geophone at depth. Then, the horizontal slowness also needs to be constrained by the inverse procedure. However, we do not have to incorporate the horizontal slowness in the inverse procedure when a short array of geophones is deployed at the surface, since it can be measured directly.

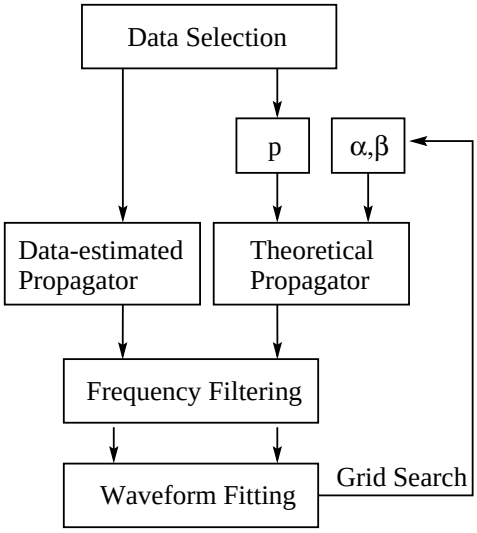

Figure 3.1: Propagator inversion scheme for α and β.

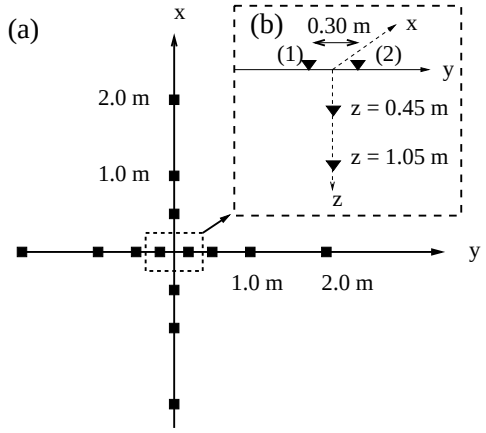

Figure 3.2: 3D receiver configuration for the Zeist field experiment, (a) top view and (b) front view. All geophones were multicomponent geophones, and the source positions were located on the $x-$axis.

Propagator inversion consists of the following steps. First, a data window is selected to isolate an arrival. The window is tapered at its edges by a cosine taper. Second, the selected data are used as input for propagator estimation. The horizontal slowness p of the dominant arrival in this time window can be determined using the array of geophones in the inline direction x. This is accomplished by estimating the time shifts for which the stack power is optimized. The remaining unknown parameters in the theoretical propagator for a homogeneous isotropic medium are α and β [equations (3.2)–(3.11)]. Values for α and β are selected using a grid search technique. A physical bound is imposed such that $\beta < \alpha/\sqrt{2}$, i.e. the Poisson's ratio has to be positive. Given values for α, β and p, the theoretical propagator can be evaluated. Before comparing the waveforms of the theoretical propagator $\mathbf{P}$ to the data estimated propagator $\tilde{\mathbf{P}}$, frequency filtering is necessary, since $\tilde{\mathbf{P}}$ is band-limited, whereas $\mathbf{P}$ has an infinite bandwidth. After bandwidth equalization, the propagator waveforms can be compared to each other. The L2 norm was used as objective function:

$$E_{ij} = \left\{ \sum_{t=-N\Delta t}^{N\Delta t} \left[\tilde{P}_{ij}(t) - P_{ij}(t,\alpha,\beta,p) \right]^2 \right\}^{1/2}, . \tag{3.17}$$

with $i,j = 1,3$. The objective function for the joint inverse of all propagator coefficients is given by the sum of all individual misfit functions,

$$E_{tot} = E_{11} + E_{13} + E_{31} + E_{33}.. \tag{3.18}$$

Estimates for α and β can be obtained by minimizing E_{tot}.

3.4 Application on Zeist field data

We illustrate propagator inversion on a field data set acquired in Zeist, the Netherlands. On this site, the near-surface material mainly consists of unconsolidated sands, with on top a thin layer of vegetation soil.

3.4.1 Data acquisition

A walkaway noise test was performed with 3C 4.5 Hz geophones at offsets between 0.75 and 84 m, with 0.75 m geophone spacing. These data (Figure 3.3) show that groundroll and guided waves are dominant in the recordings. In addition, measurements were made with a dense 3D 3C receiving configuration that will be used for propagator inversion (see Figure 3.2). Geophones were positioned in a cross-shape at the surface. In the $x-$direction, receivers were located at 0.50, 1.00 and 2.00 m distance to the center of the configuration, in the $y-$direction the distances were 0.15, 0.50, 1.00 and 2.00 m. The buried geophones were positioned at 0.45 and 1.05 m depth, respectively. Geophones can be buried efficiently in unconsolidated sediments using a hand ground drill. This approach minimizes the medium perturbations caused by burial of geophones. For the dense 3D 3C group, data were acquired using 11 different source positions located between 35 and 85 m offset. The shot spacing was 5.0 m, and all shot points were located on the $x-$axis. The experiment was repeated four times for every shot position. During the whole experiment, a weight drop source was used. A steel ball of about 37 kg was dropped from approximately 3.5 m height on a steel plate resting on the ground. The recording instrument was a Bison Spectra with 48 channels, and the time sampling interval was 0.25 ms.

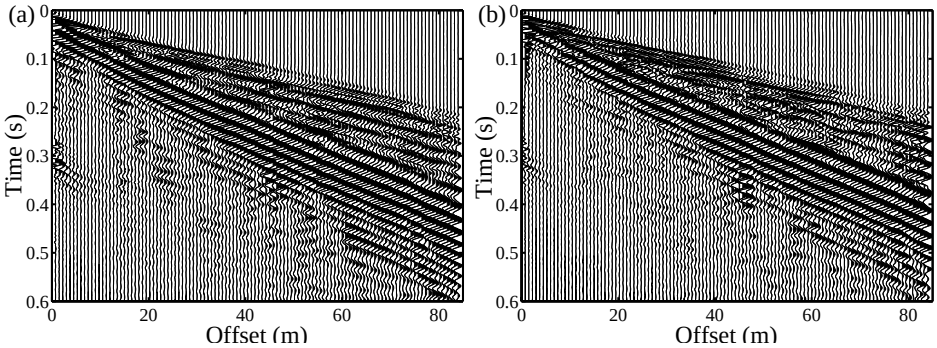

Figure 3.3: Walkaway noise survey for (a) v_x and (b) v_z. The panels are displayed with trace normalization.

3.4.2 Data selection and estimation of horizontal slowness

In theory, the propagator method is valid for a single slowness, i.e. isolating an arrival as uncontaminated as possible by other arrivals. On the other hand, considering only very short time windows results in a poor signal-to-noise ratio. Synthetic experiments demonstrated that propagator inversion is insensitive to small slowness variations in the selected data (Van Vossen et al., 2004c). Therefore, we selected data windows including all events arriving before the ground roll. For each shot position, time windows which contain the selected data are listed in Table 3.1. A cosine taper with 0.01 s length was applied to both edges of the window. An example of data selected for slowness estimation is shown in Figure 3.4. A bandpass filter with cut-off frequencies between 40 and 140 Hz was applied to these recordings. The events shown may be interpreted as trapped waves above the groundwater table. Because there are significant differences in the recorded amplitudes on the inline component, we decided to estimate p using only the vertical component of the recorded particle velocity. These slowness estimates are given for each shot position in Table 3.1. The differences between the estimated horizontal slownesses for the different source positions are small.

3.4.3 Propagator estimation and inversion

Contrary to horizontal slowness estimation, no frequency filtering was applied to the selected data prior to propagator estimation. An example of the data used for propagator estimation is shown in Figure 3.5. It shows that recordings rapidly change with depth, especially on the vertical component. At 0.45 m depth, high frequencies are strongly attenuated compared to the recordings obtained at the free surface and at 1.05 m depth. On the other hand, the low-frequency content of the signal decays with depth. This charac-

shot number	offset (m)	t_1 (s)	t_2 (s)	p (ms/m)	$\sigma(p)$ (ms/m)
1	85	0.19	0.26	2.10	0.11
2	80	0.18	0.25	2.12	0.07
3	75	0.17	0.24	2.23	0.03
4	70	0.16	0.23	2.18	0.06
5	65	0.15	0.22	2.20	0.06
6	60	0.14	0.21	2.15	0.06
7	55	0.13	0.20	2.12	0.04
8	50	0.11	0.18	2.11	0.03
9	45	0.09	0.17	2.23	0.05
10	40	0.08	0.16	2.19	0.05
11	35	0.07	0.14	2.21	0.03
mean				2.17	0.05

Table 3.1: Horizontal slowness estimates for each shot position. Data are selected in time windows with t between t_1 and t_2.

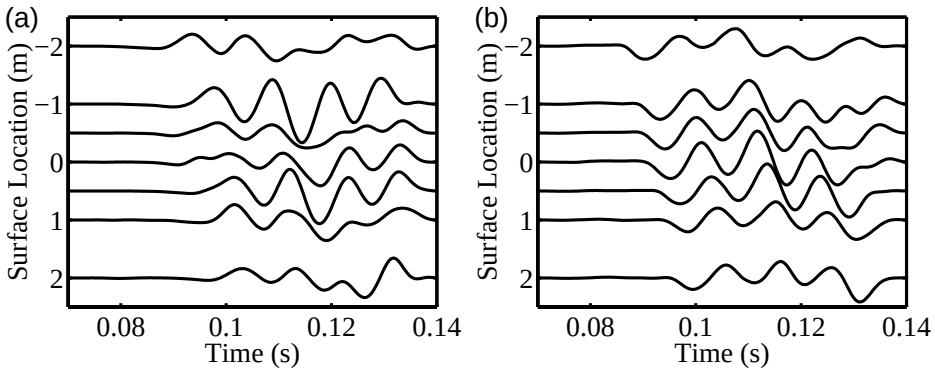

Figure 3.4: (a) Inline and (b) vertical component recordings with the source located at 35 m distance to the center of the receiver group.

teristic behavior is caused by interference between free-surface incident and its reflected and converted waves.

The interpretation of the data recorded on the horizontal component is difficult. The two surface geophones show that there are significant amplitude differences in the high-frequency part of the spectrum. For lower frequencies on the other hand, there is an excellent agreement between these recordings. This observation could indicate coupling differences between these two surface geophones (Krohn, 1984). Another interesting observation is that the amount of energy recorded in the 50 to 60 Hz frequency band is small, whereas we did not apply a notch filter to the data.

We demonstrate propagator inversion first using surface geophone (1) and the buried geophone at 1.05 m depth. Then, we consider the data recorded by surface geophone (2). Given the frequency content of the signal and the time sampling interval of 0.25 ms, accurate velocity estimation with the geophone buried at 0.45 m depth is in our opinion not feasible.

Figure 3.6 shows the data-estimated propagator for each shot position. The frequency passband is between 40 and 140 Hz. The theoretical propagator $\mathbf{P}$ is shown with α and β for which E_{tot} is minimized. There is a good agreement between $\tilde{\mathbf{P}}$ and $\mathbf{P}$ for most individual shots. Since the changes in the estimated horizontal slowness are small (Table 3.1), stacking of the data-estimated propagator components over all source positions is not in conflict with the single slowness assumption. This process enhances the signal-to-noise ratio of the data-estimated propagator. Figure 3.6 shows that an excellent fit is obtained between the averaged propagator components and the best fitting theoretical propagator.

The constraints offered by each individual propagator component are shown in Figures 3.7a–d. Misfit functions are shown for the stacked propagator, and the minima of the prestack propagators illustrate the uncertainty. No computations are performed with combinations for α and β for which the Poisson ratio becomes negative. The misfit functions

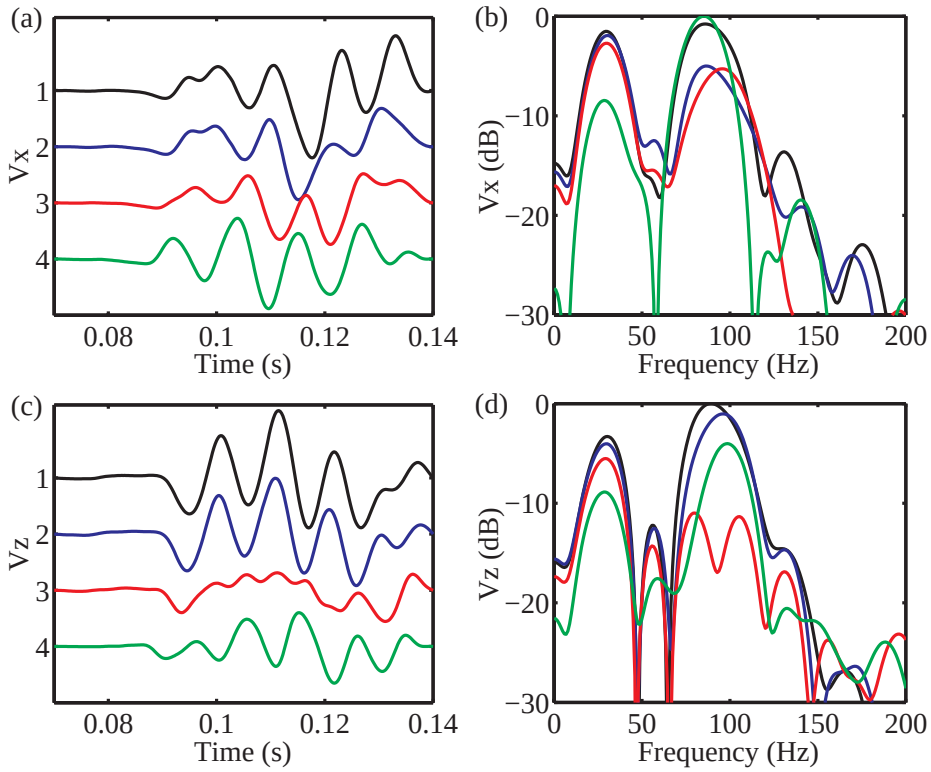

Figure 3.5: Traces and amplitude spectra for v_x (a,b) and for v_z (c,d) for different depths, recorded at 35 m offset. The black and blue traces are the recordings acquired at the free surface by the geophones labelled (1) and (2) (Fig. 3.2), the red traces were acquired at 0.45 m depth, and the green traces at 1.05 m depth.

show that P_{11} and P_{31} are dominantly sensitive to variations in β, whereas P_{33} is more sensitive to variations in α. P_{13} contains information on both α and β. Because P_{33} is dominantly sensitive to variations in α, $(\beta p)^2 \ll 1$ [equation (3.3)]. This is confirmed by Table 3.1. Thus, for near-vertical incident waves, the propagator inversion is dominantly sensitive to phase differences rather than amplitude effects as a result of interaction of the incident wavefield with the free surface. However, close to the critical angle for incident S-waves, the amplitude coefficient of P_{13} changes rapidly, which results in sensitivity for both α and β.

Figure 3.7e illustrates the joint inversion for all propagator coefficients. Both α and β are well constrained. The minimum of the joint inversion is equal to the average of all minima of the misfit functions for each individual shot. We obtain the following estimates: $\alpha = 270 \pm 15$ m/s and $\beta = 150 \pm 9$ m/s. The uncertainties given are the standard deviations

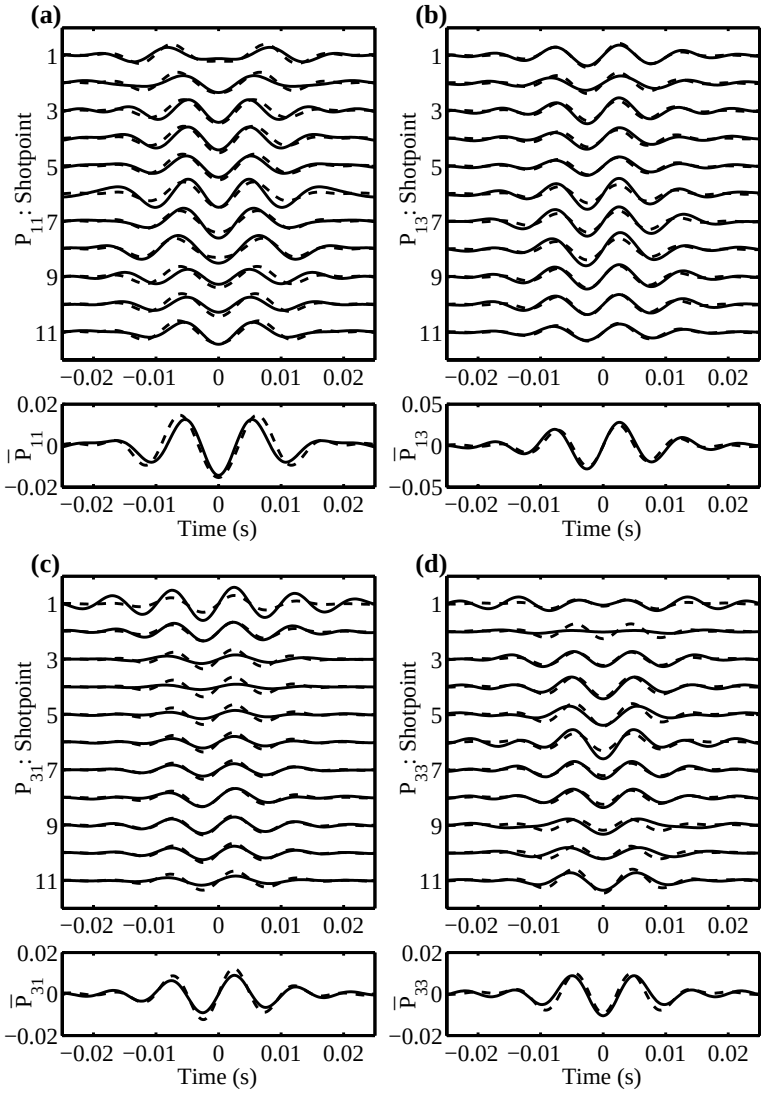

Figure 3.6: Prestack and poststack data-estimated propagators (solid) compared to the best fitting theoretical propagator (dashed). Shown are (a) P_{11}, (b) P_{13}, (c) P_{31}, and (d) P_{33}. The data-estimated propagators are computed using surface geophone (1) and the buried geophone at 1.05 m depth. Frequency filters are applied with pass band between 40 and 140 Hz.

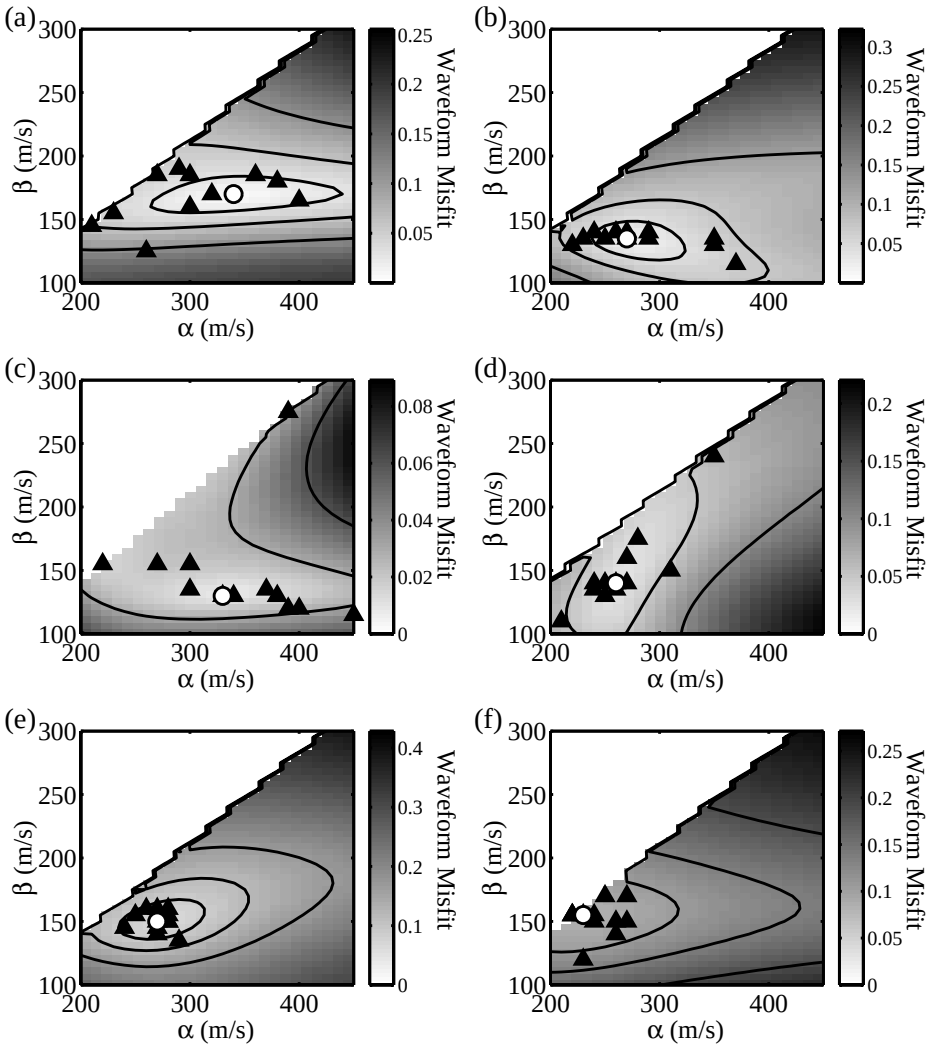

Figure 3.7: Waveform misfit functions (a) E_{11}, (b) E_{13}, (c) E_{31}, (d) E_{33} for poststack P_{11}, P_{13}, P_{31}, and P_{33} computed using surface geophone (1). The combined constraints are shown in (e). The joint inverse results using surface geophone (2) are shown in (f). Contours are drawn for $E_{ij} = min(E_{ij}) + c$, with $c = 0.02$, 0.05 and 0.10, and the indices i and j take the values 1 or 3. The open circle denotes the minimum of E_{ij}, and the triangles indicate the positions of the minima of E_{ij} for each individual shot. No computations are performed in the non-physical region $\beta > \alpha/\sqrt{2}$.

of the variation of best estimates for the individual shots.

So far we have only discussed the data-estimated propagator obtained using surface geophone (1). Because there are significant differences between the horizontal component recordings (1) and (2) (Figure 3.5), it is important to assess the consequences of these data differences on propagator estimation and inversion. This allows us to determine whether propagator inversion is robust in the presence of realistic data errors. Figure 3.8 shows that the match between $\tilde{\mathbf{P}}$ and $\mathbf{P}$ is not as good compared to the results for surface geophone (1), although the fit is good for the first three shot points and for P_{33}. This propagator coefficient is not significantly affected by data variations on the horizontal component: it relates the vertical component acquired at the free-surface to the same component at depth [equation(3.1)]. The high-cut frequency was lowered to 100 Hz to reduce the effects of coupling errors to the velocity estimation. The misfit function for the joint inverse of all stacked propagators is shown in Figure 3.7f. The velocities corresponding to the minimum of E_{tot} are $\alpha = 230$ m/s and $\beta = 155$ m/s. Averaging all individual shots gives: $\alpha = 244 \pm 20$ m/s and $\beta = 152 \pm 14$ m/s. The estimates for β agree well with the previously obtained velocity estimates, whereas α is less consistent. For shotpoints 1, 2 and 3, which show a good match between $\tilde{\mathbf{P}}$ and $\mathbf{P}$, we find that $\alpha \geq 260$ m/s.

Although geophones (1) and (2) were close together (spacing 0.30 m between them), the horizontal component data recorded by these two geophones significantly differ for frequencies above 70 Hz. These amplitude differences are attributed to geophone-ground coupling. This refers to the accuracy with which a geophone measures the actual ground motion. It is especially relevant for horizontal component recordings. A well-coupled horizontal geophone has coupling resonance frequency of 130 Hz, whereas poorly coupled horizontal geophones could have significantly lower (down to 30 Hz) resonance frequencies (Krohn, 1984). For frequencies much lower than the coupling resonance frequency, the geophone accurately follows the ground motion.

The results of surface geophone (1) are not sensitive to changes in the high-cut frequency from 100 up to 140 Hz. Increasing this frequency reduced the uncertainty in the velocity estimates. For surface geophone (2) on the other hand, increasing this frequency resulted in poor fits of the propagator coefficients and large uncertainties in the estimated velocities. Therefore, we decided to use different frequency bands for the application of propagator inversion to data acquired by surface geophones (1) and (2). The obtained results are hardly influenced by the choice of the low-cut frequency. Lowering this frequency to 20 Hz yielded similar velocity estimates, although the data misfit between $\mathbf{P}$ and $\tilde{\mathbf{P}}$ somewhat increased, resulting in larger uncertainties attached to these estimates. Therefore, we selected 40 Hz as low-cut frequency.

Thus, the analysis indicates that best results are obtained with the data recorded by surface geophone (1). For surface geophone (1), inversion results are stable up to 140 Hz, a better data fit is obtained, and the data have a better resolving power for near-surface P- and S-wave velocities. Although the data quality of the recordings of surface geophone (2) is less good, the estimate for the S-wave velocity is in agreement with the results obtained with surface geophone (1), and the difference between the obtained P-wave velocities is approximately 10 % of the estimated value. This indicates that the propagator inversion is robust in the presence of measurement errors.

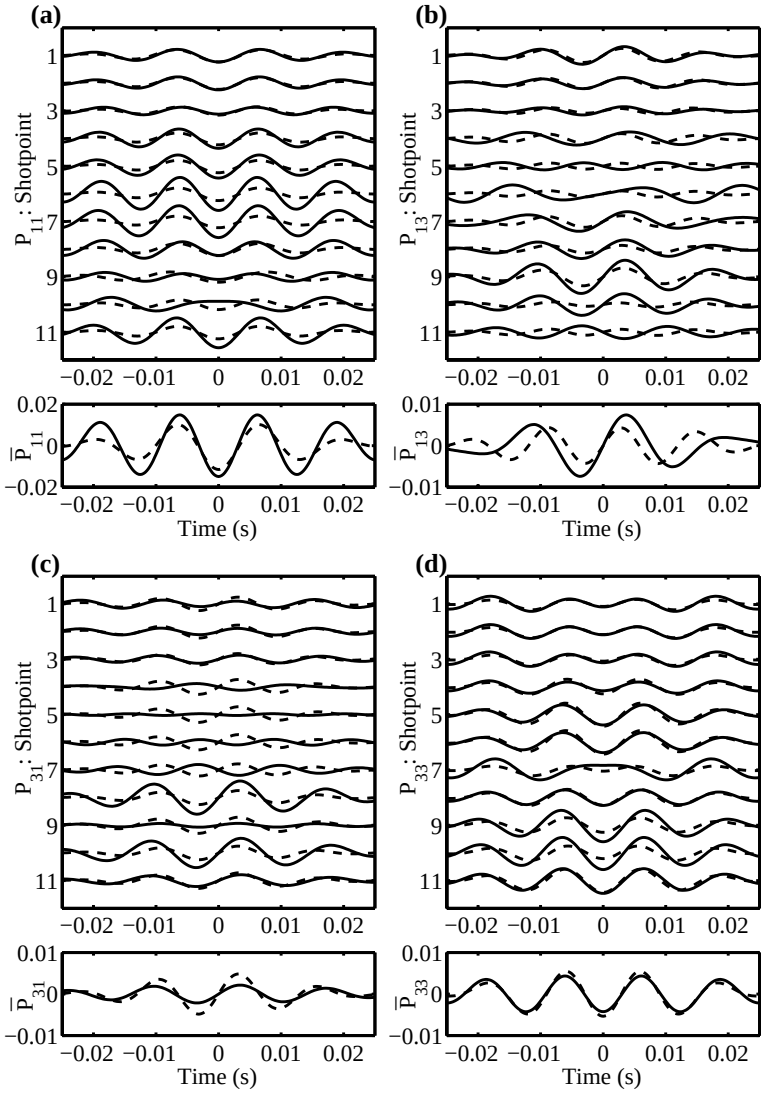

Figure 3.8: Prestack and poststack data-estimated propagators (solid) compared to the best fitting theoretical propagator (dashed). Shown are (a) P_{11}, (b) P_{13}, (c) P_{31}, and (d) P_{33}. The data-estimated propagators are computed using surface geophone (2) and the buried geophone at 1.05 m depth. Frequency filters are applied with pass band between 40 and 100 Hz.

3.5 Discussion

Low near-surface velocities are obtained with propagator inversion, namely $\alpha = 270 \pm 15$ m/s and $\beta = 150 \pm 9$ m/s using geophone (1). The Poisson ratio σ which corresponds to these velocities is 0.28 with uncertainty range between 0.18 and 0.34. Because the Poisson ratio is sensitive to perturbations in the estimated velocities, it is difficult to make a sensible lithological interpretation. Despite this uncertainty, we may argue that the observed Poisson ratio lies between the end-member models for dry, gas-saturated sands with $\sigma \in [0.0\ 0.22]$ and water-saturated sands with $\sigma \in [0.38\ 0.50]$ (Bourbié et al., 1987), which qualitatively makes sense because the considered sediment was partially water-saturated.

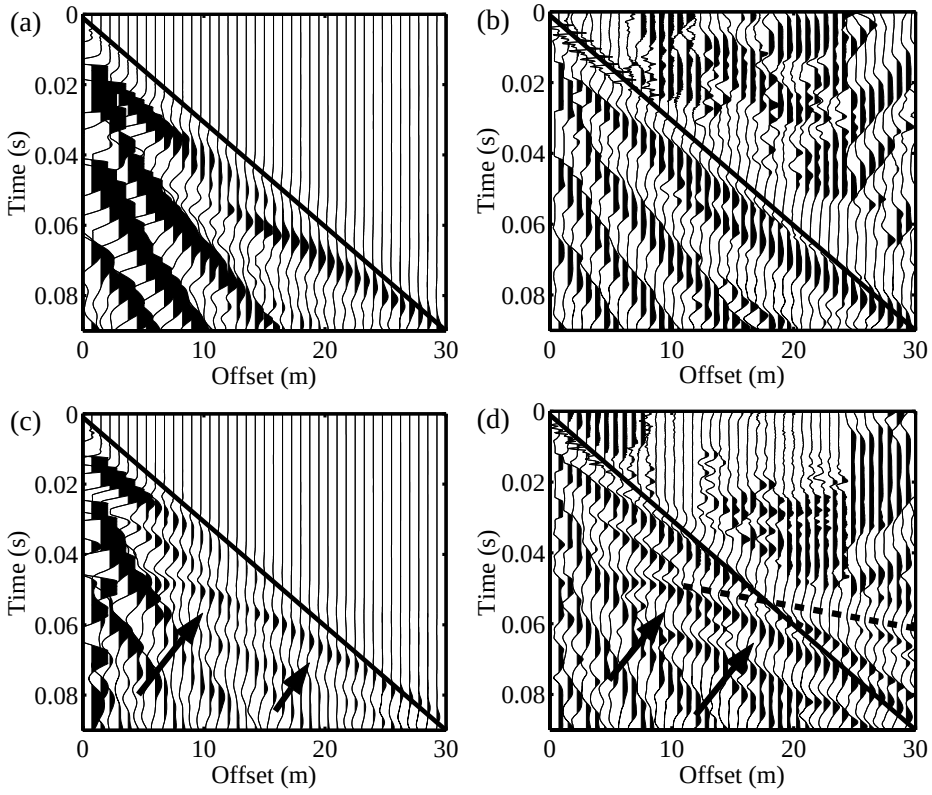

Figure 3.9: Near-source traces of walkaway noise survey for (a) v_x,(b) v_x with 0.005 s AGC window, (c) v_z and (d) v_z with 0.005 s AGC window. The airwave is indicated with the solid line, the groundwater refraction with the dashed line, and the arrows indicate the reflected P wave at the groundwater table.

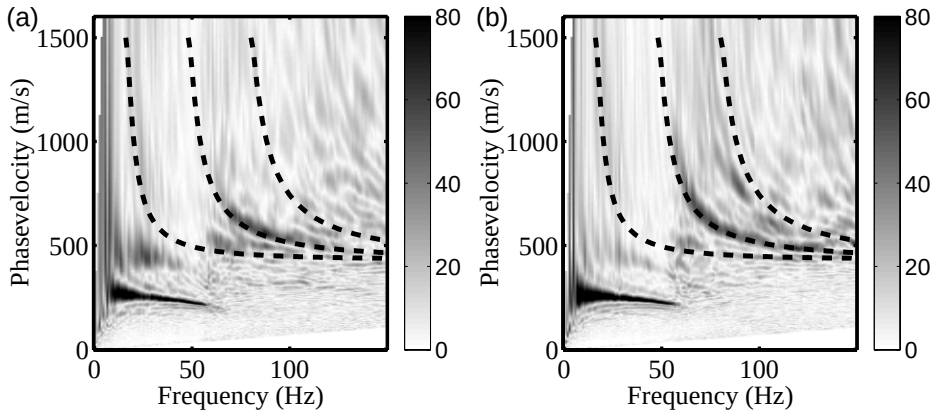

Figure 3.10: Amplitude spectra (horizontal phase velocity versus frequency) for v_x (a) and v_z (b). Rayleigh waves are characterized by low velocities and frequencies, whereas guided waves have higher velocities and frequencies. Theoretical curves for guided wave modes (0,1,2) are fitted to the data. The parameters for these theoretical dispersion curves are listed in Table 3.2.

To test the results of propagator inversion, we analyze the Zeist walkaway noisespread with recordings between 0 and 84 m offset. Near-offset sections of these data are shown in Figure 3.9. The receiver spacing is 0.75 m. No frequency filtering was applied to these multicomponent recordings. The airwave is clearly visible on both the inline and vertical components in the automatic gain control (AGC) plots. In the offset range between 0 and 10 m we do not observe coherent energy arriving before the airwave. Events with a higher moveout velocity arrive just after the airwave. This indicates that the near-surface velocity is low, and that velocities increase with depth close to the free surface. Between 15 and 30 m offset, the refracted wave from the water table can be observed, and also the reflected wave from this interface can easily be identified on the vertical component.

The recordings in the complete noisespread are dominated by surface waves and guided waves traveling above the groundwater table (Figure 3.3). Independent estimates for the near-surface P velocity and depth of the water table can be obtained by dispersion analysis of these guided waves (Brekhovskikh, 1980; Robertsson et al., 1996). This analysis assumes that the medium below the free-surface is acoustic and homogeneous. These assumptions are reasonable since water saturation leads to a sharp increase in P velocity while the S velocity remains very low (Stümpel et al., 1984).

For the dispersion analysis, the data shown in Figure 3.3 are transformed using a technique proposed by Park et al. (1998). Amplitude spectra of the transformed data are shown in Figure 3.10. The low-frequency part of the spectrum is dominated by groundroll, whereas guided waves have higher frequencies and velocities. Different modes for guided waves can be identified. The higher modes are more pronounced on the spectrum of

P-wave velocity top layer	430 m/s
P-wave velocity half-space	1500 m/s
Density top layer	1700 kg/m^3
Density half-space	2000 kg/m^3
Thickness top layer	7.5 m

Table 3.2: Parameters of the guided wave dispersion curves.

v_z. Dispersion curves for guided waves (Brekhovskikh, 1980; Robertsson et al., 1996) are matched to these data by varying the thickness of the top layer and its P velocity. The P velocity for the second layer is obtained from the groundwater refraction. The parameters used to construct the dispersion curves are listed in Table 3.2. The densities hardly influence the dispersion curves.

At first glance, there seems to be a discrepancy between the obtained velocities, $\alpha \approx 430$ m/s and $\beta \approx 200$ m/s from dispersion analysis of guided waves and from propagator inversion. However, the thickness of the near-surface low-velocity layer is estimated at about 7.5 m. Dispersion analysis yields an average velocity for this layer, whereas propagator inversion determines the velocity for the top 1.0 m of this layer. Because dispersion analysis yields observations on a different scale, we cannot compare these observations to the velocities obtained with propagator inversion directly. It is because of these different depth sensitivities that subsonic near-surface P-wave velocities are not commonly observed in this seismic frequency range. Furthermore the results suggest that the velocities increase with depth in the unsaturated zone, from 270 ± 15 m/s in the top meter, with an average of around 430 m/s in the top 7.5 m, before an abrupt change in the P velocity to around 1500 m/s occurs at the groundwater table. This observation is consistent with the results of White and Sengbush (1953), and also explains the near-offset data shown in Figure 3.9.

We have therefore shown that information on very shallow near-surface wave velocities can be obtained with the propagator method using a 3D geophone configuration. Although shallow material properties may influence the actual wave propagation, we believe that these have most impact on the *measured* wavefield. Both the energy transmitted into the ground and the recordings of the wavefield by geophones depend on the near-surface soil conditions.

The repeatability of the source mostly depends on the (an)elastic properties of the soil (Aritman, 2001). Both the amount of energy radiated into the ground and the radiation pattern are influenced by the near-source material properties. Lateral variations in near-surface material properties could lead to poor repeatability of the source, degrading the quality of the seismic section. In addition, the measurements of the recording instruments differ from the actual ground motion. The so-called receiver coupling is influenced by the stiffness of the soil (Krohn, 1984). As a consequence, differences between recordings of adjacent receivers can exist due to coupling differences. Coupling errors especially affect the quality of converted wave data. Thus, correct processing and interpretation of

seismic data acquired in a land seismic survey requires an understanding of both source and receiver coupling effects, and such an understanding may be facilitated by the very near-surface velocity estimates obtained using propagator inversion.

Another issue is the interaction of the wavefield with the free surface. Usually, we are only interested in the free-surface incident P and S waves, while receivers placed on land measure the interaction of these incident wavefields with the free-surface. In principle, we can obtain the free-surface incident P and S waves using wavefield decomposition. Wavefield decomposition requires as input the free-surface reflectivity, which depend on the P- and S-wave velocities just below the free-surface. Because we measure the wavefield exactly at the free surface, we should not use effective or averaged medium parameters for wavefield decomposition. Thus, the very shallow material properties obtained with propagator inversion may improve wavefield decomposition and demultiple.

Although application of the propagator method would require additional effort in acquiring data, we demonstrated that the technique provides additional information relevant for a land seismic survey. The propagator method can be incorporated into a seismic survey without having to perform an additional high-resolution experiment.

Finally, it should be mentioned that propagator estimation assumes that the medium is elastic. Although attenuation can be significant in the weathered layer, it does not affect the obtained results, since the dominant wavelength of the analyzed signal is not much smaller than the distance between the surface and buried geophone.

3.6 Conclusions

The data-estimated propagator contains all information on the material parameters governing wave propagation between the free-surface and the depth of a buried geophone. We applied propagator inversion on Zeist field data to determine the local near-surface velocities. This inversion yielded subsonic compressional wave velocity, $\alpha = 270 \pm 15$ m/s, and a low shear velocity, $\beta = 150 \pm 9$ m/s for the top meter.

Higher velocities are obtained with dispersion analysis of guided waves for α. This difference is attributed to the different depth sensitivity of dispersion analysis. Propagator inversion is only sensitive to the wave velocities between the free surface and the buried geophone, whereas dispersion analysis is sensitive to velocities in the entire layer above the water table. For this reason, these low P and S velocities are not commonly observed in seismic surveys with a deeper target.

Although very shallow anomalies are considered to have a small impact on the wavefield propagation, these may significantly influence the wavefield recordings. Both the energy transmitted into the subsurface by the source and receiver coupling depend on very shallow material properties. Hence, lateral changes in material properties could lead to poor repeatability of the source and receiver coupling differences. Also corrections for the interaction of the wavefield with the free-surface require these shallow wave velocities to be known.

Chapter 4

Surface-consistent amplitude corrections for single- or multi-component sources and receivers using reciprocity and waveform inversion

Abstract

In land seismics, near-surface conditions often vary within surveys, resulting in differences in source strength and signature. Furthermore, discrepancies between closely spaced recordings are also commonly observed. Processing and interpretation of recorded data require that data are corrected for these source and receiver perturbations in the early stages of processing. However, existing surface-consistent deconvolution techniques are applicable to primary reflection data only, and therefore require that ground roll and multiples are suppressed prior to the application. This is usually performed with multichannel filter operations. The performance of these filter operations, however, rapidly deteriorates in presence of acquisition-related amplitude and phase perturbations. We propose an alternative approach to compensate for acquisition-related perturbations. It is essentially a preprocessing step, and has the following characteristics: (i) it can be applied to complete recordings, hence does not require the isolation of primary reflections in the data, (ii) no assumptions are imposed on the subsurface, and (iii) it is applicable to multicomponent data. The procedure is based on reciprocity of the medium response, so that differences

This chapter has been submitted for publication by R. Van Vossen, A. Curtis and J. Trampert to *Geophysical Journal International*.

between normal and reciprocal traces can be attributed to source and receiver perturbations. The application of reciprocity requires symmetric data acquisition, i.e. identical source and receiver patterns, identical locations, and the source orientations have to be identical to the receiver components. Besides reciprocity, additional constraints are required to determine the lateral source and receiver amplitude variations fully. We use criteria based on minimizing total energy differences between adjacent common source and common receiver gathers, and in common offset panels of the medium response. Synthetic tests demonstrate that acquisition-related amplitude differences can be significantly reduced using this method.

4.1 Introduction

Amplitude anomalies of reflections in seismic recordings have been used for many decades. Initially, the focus was the search for high-intensity seismic reflections, so-called bright spots, in stacked seismic sections. These bright spots could indicate hydrocarbon accumulations, particularly gas. An important development was the introduction of amplitude-versus offset (AVO) interpretation techniques (Ostrander, 1984): observations of reflection coefficients for different angles of incidence can be used to discriminate different lithologies. This allows the separation of gas- and non-gas- related amplitude anomalies. Other applications are the detection of oil reservoirs and of porosity in carbonates (Castagna and Backus, 1993).

However, before we can interpret amplitudes in recorded data, we have to compensate for near-surface and acquisition-related effects, such as source strength and receiver coupling variations, preferably in the early stages of the processing. These variations influence all common-midpoint (CMP) based processing, since traces with different sources and receivers are combined in a CMP stack. This degrades the quality of the stack and could lead to biased AVO trends, particularly when related to slowly varying near-surface conditions.

For multicomponent data, it is important to realize that acquisition-related perturbations distort the vector-wavefield characteristics, since coupling has a different effect on horizontal and vertical source and receiver components (Krohn, 1984). This can bias the observed polarization (Li and MacBeth, 1997; Michaud and Snieder, 2004). For example, determining the polarization direction of the leading split shear wave involves simultaneous rotation of the horizontal source and receiver coordinates to conform with the principal axes of an azimuthal anisotropic medium (Alford, 1986). This can only be achieved after separating the acquisition-related amplitude effects on the different recorded wavefield components from the medium response effects.

Amplitude corrections can be performed using surface-consistent processing techniques (Taner and Koehler, 1981; Levin, 1989; Cambois and Stoffa, 1992; Cary and Lorentz, 1993). Surface consistency refers to the following approximations: the source and receiver amplitude terms can be expressed as finite-impulse response filters which do not vary throughout the recording time and are independent of the direction of propagation of the incident wavefield. These existing techniques are applicable to primary reflections

which have to be isolated in the data, and common-depth point (CDP) gathering is assumed to be valid. The isolation of primary reflections requires the suppression of ground roll and multiples, which is commonly performed using multichannel filter operations. However, the performance of these multichannel filter operations rapidly deteriorates in presence of amplitude and phase perturbations as a result of the wavefield acquisition (Newman and Mahoney, 1973). Therefore, it is not surprising that careful preprocessing is required before multiples can be successfully eliminated (Kelamis and Verschuur, 2000).

We developed an alternative approach to compensate for source and receiver perturbations which is essentially a preprocessing step. It takes full seismic waveforms into account, and does not require mid-point binning. The approach uses reciprocity of the medium response for evaluating lateral source and receiver amplitude variations: differences between normal and reciprocal traces can be attributed to differences in source strength and receiver coupling. Karrenbach (1994) and Luo and Li (1998) applied this technique to determine the seismic source wavelets, assuming that there are no lateral variations in receiver coupling. We show how the latter constraint can be relaxed. This method is also suitable for application to multicomponent data for which the conventional methods cited above often fail because it is more difficult to identify and isolate primary reflections.

Application of reciprocity requires symmetric data acquisition. This includes identical source and receiver positions and shot/receiver patterns, and identical source and receiver components. Multicomponent recordings require thus multicomponent sources.

4.2 Background theory: convolutional model and reciprocity

Multicomponent data (3C $\times$ 3C), excited by a source located at $\mathbf{x}_j$ and recorded at location $\mathbf{x}_i$ can be represented as a matrix of traces (Tatham and McCormack, 1991):

$$\mathbf{V}(t,i,j) = \begin{pmatrix} V_{xx}(t,i,j) & V_{xy}(t,i,j) & V_{xz}(t,i,j) \\ V_{yx}(t,i,j) & V_{yy}(t,i,j) & V_{yz}(t,i,j) \\ V_{zx}(t,i,j) & V_{zy}(t,i,j) & V_{zz}(t,i,j) \end{pmatrix}, \tag{4.1}$$

with the top row corresponding to the in-line (x) geophone traces from in-line (x), crossline (y), and vertical (z) sources. The second row contains crossline geophone traces, and the third row vertical geophone traces. We assume that the source and receiver positions are located on a line. The indices i and j refer to the receiver and source location numbers, respectively.

Considering the earth as a linear system for the propagation of seismic waves, the recorded traces $\mathbf{V}(t,i,j)$ satisfy the convolutional model (Zeng and MacBeth, 1993),

$$\mathbf{V}(t,i,j) = \mathbf{R}(t,i) * \mathbf{G}(t,i,j) * \mathbf{S}(t,j), \tag{4.2}$$

where $\mathbf{R}(t,i)$ is the receiver response at surface location $\mathbf{x}_i$, $\mathbf{S}(t,j)$ is the source signature at surface position $\mathbf{x}_j$, and $\mathbf{G}(t,i,j)$ is the corresponding medium response. The asterisk $(*)$ denotes convolution in the time domain.

We assume that $\mathbf{R}(t,i)$ and $\mathbf{S}(t,j)$ are surface consistent. This means that effects associated with a particular source or receiver remain constant throughout the recording time, and affect all wave types similarly, regardless of the direction of propagation. The time dependence in $\mathbf{R}(t,i)$ and $\mathbf{S}(t,j)$ denotes the length of the finite-impulse response filters. We also assume that sources and geophones are perfectly aligned, and that cross-coupling between different source and receiver components can be neglected. Then, the geophone and source responses $\mathbf{R}(t,i)$ and $\mathbf{S}(t,j)$ are diagonal matrices of time series with the principal components given by the scalar functions of the in-line, cross-line, and vertical geophones and sources.

The objective at this stage is to determine the medium response $\mathbf{G}(t,i,j)$, or to remove the influence of lateral source and receiver variations from the recorded data. To achieve this, we have to determine the individual components in the convolutional model [equation (4.2)]. We can reduce the number of unknown parameters using reciprocity. Because the medium response is reciprocal, differences between recordings of a reciprocal source/receiver pair can be attributed to lateral differences in source strength and receiver coupling. Reciprocity of the medium response is expressed as (Knopoff and Gangi, 1959; White, 1960):

$$\mathbf{G}(t,i,j) = \mathbf{G}^T(t,j,i), \tag{4.3}$$

where $\mathbf{G}^T$ is the transpose of $\mathbf{G}$. Reciprocity can only be applied to data if symmetry conditions are satisfied during data acquisition: the source positions should be identical to the receiver positions, and application of reciprocity to multicomponent recordings also requires multicomponent sources.

4.3 Formulation of the inverse problem

Let us assume that we have data recorded with N identical source and receiver positions, such that $i,j = 1,\ldots,N$. Then, the convolutional model and reciprocity result in a system of equations which constrain the individual terms in the convolutional model. We can formulate a linear inverse problem in the log/Fourier domain (Taner and Koehler, 1981; Cambois and Stoffa, 1992), where $\log x$ denotes the natural logarithm of x. The log/Fourier transform of a time function $X(t)$ is defined as

$$\tilde{X}(\omega) = \log\left[\int_{-\infty}^{\infty} X(t)e^{-i\omega t}\mathrm{d}t\right], \tag{4.4}$$

with the inverse transform

$$X(t) = \frac{1}{2\pi}\int_{-\infty}^{\infty} e^{\tilde{X}(\omega)+i\omega t}\mathrm{d}\omega. \tag{4.5}$$

Since convolution in the time domain is equivalent to summation in the log/Fourier domain, the convolutional model becomes in the log/Fourier domain:

$$\tilde{\mathbf{V}}(\omega, i, j) = \tilde{\mathbf{R}}(\omega, i) + \tilde{\mathbf{G}}(\omega, i, j) + \tilde{\mathbf{S}}(\omega, j). \tag{4.6}$$

The real part of equation (4.6) describes the decomposition of the natural logarithm of the Fourier amplitude spectra into the source, receiver, and medium response terms, whereas the imaginary part of equation (4.6) gives the decomposition of the phase. In the following, we only consider the amplitude component of the problem.

For the analysis of the system of equations, it is convenient to recast equation (4.6) in a matrix-vector form:

$$\mathbf{A}\mathbf{m}(\omega) = \mathbf{d}(\omega), \tag{4.7}$$

where $\mathbf{A}$ is the coefficient matrix, $\mathbf{m}(\omega)$ contains the unknown parameters in the log/Fourier domain, and the data-vector $\mathbf{d}(\omega)$ contains the measurements of the wavefield $\tilde{\mathbf{V}}(\omega, i, j)$. The "model" vector $\mathbf{m}(\omega)$ is partitioned into the individual components:

$$\mathbf{m}(\omega) = \begin{pmatrix} \mathbf{m}_G(\omega) \\ \mathbf{m}_R(\omega) \\ \mathbf{m}_S(\omega) \end{pmatrix}, \tag{4.8}$$

where $\mathbf{m}_G(\omega)$ contains the medium response, $\mathbf{m}_R(\omega)$ the receiver terms, and $\mathbf{m}_S(\omega)$ the source wavelets. The coefficient matrix $\mathbf{A}$ is frequency independent. It only contains ones and zeros.

We treat reciprocity of the medium response as an exact relationship. Instead of inserting the reciprocal equations (4.3) in the coefficient matrix $\mathbf{A}$, we directly reduce the number of unknown parameters in $\mathbf{m}_G(\omega)$ by explicitly substituting the reciprocal medium response terms using equation (4.3). Since the number of unknowns is reduced, this approach is computationally favourable.

Furthermore, we can only solve for relative source and receiver differences. Consequently, we can impose a zero-mean constraint on the source and receiver terms without loss of generality. We also treat this as an exact relationship and implement it in a similar fashion as the reciprocity constraints.

4.4 Analysis of reciprocity constraints on single component data

Consider single component data with forty-one ($N = 41$) identical source/receiver positions. For $N > 5$, there are more data $N_D = N^2$ than unknown parameters $N_U = (N+1)N/2 + 2(N-1)$: $\mathbf{m}_G$ has $(N+1)N/2$ unknown coefficients, and both $\mathbf{m}_R$ and $\mathbf{m}_S$ contain $N-1$ unknown terms. In this example, there are 941 unknown parameters. We use singular value decomposition (Lanczos, 1961) to analyze the constraints on the model parameters. The singular values are shown in Figure 4.1. There are $N-1$ zero

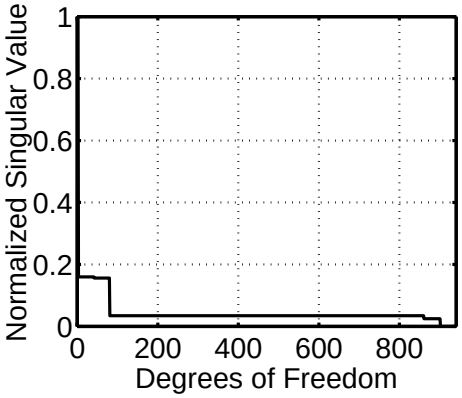

Figure 4.1: Normalized singular values of $\mathbf{A}$ using 41 sources and receivers. The total number of degrees of freedom is then 941.

singular values, thus $N-1$ undetermined model parameters. This number corresponds to the number of model parameters in the source or receiver terms. The nonuniqueness is a result of the absence of N reciprocity constraints on zero-offset data. Thus, despite the fact that there are more equations than unknown parameters, the number of independent equations is insufficient to give a unique solution. Combining the constraints for different frequencies does not provide any additional information to reduce the model null-space, since the coefficient matrix $\mathbf{A}$ is frequency independent.

4.5 Regularization criteria

Additional information is required to obtain a unique solution to the inverse problem. We investigated regularization using both energy criteria and minimum variation in common-offset sections of the medium response. Energy criteria give prior information on the source and receiver terms, and the variation criterion provides information about the medium response. Prior information and a reference model $\mathbf{m}^0$ are included in the inverse problem defining a cost function:

$$Y = (\mathbf{Am}-\mathbf{d})^T \mathbf{C}_d^{-1} (\mathbf{Am}-\mathbf{d}) + \left(\mathbf{m}-\mathbf{m}^0\right)^T \mathbf{C}_m^{-1} \left(\mathbf{m}-\mathbf{m}^0\right), \tag{4.9}$$

where $\mathbf{C}_d^{-1}$ is the inverse of the data covariance matrix which we take to be diagonal, and $\mathbf{C}_m^{-1}$ is the inverse of the prior model covariance matrix. It is a block-diagonal matrix and can be written in partitioned form:

$$\mathbf{C}_m^{-1} = \begin{pmatrix} \mathbf{C}_{m_G}^{-1} & \mathbf{0} & \mathbf{0} \\ \mathbf{0} & \mathbf{C}_{m_R}^{-1} & \mathbf{0} \\ \mathbf{0} & \mathbf{0} & \mathbf{C}_{m_S}^{-1} \end{pmatrix}, \tag{4.10}$$

where $\mathbf{C}_{m_G}$, $\mathbf{C}_{m_R}$ and $\mathbf{C}_{m_S}$ are the covariance matrices describing prior information on the medium response, receiver, and source terms, respectively. The least squares solution of equation (4.9) is found by setting the derivatives with respect to the model parameters equal to zero, and is given by (e.g. Tarantola, 1987):

$$\tilde{\mathbf{m}} = \left(\mathbf{A}^T\mathbf{C}_d^{-1}\mathbf{A} + \mathbf{C}_m^{-1}\right)^{-1}\left(\mathbf{A}^T\mathbf{C}_d^{-1}\mathbf{d} + \mathbf{C}_m^{-1}\mathbf{m}^0\right). \tag{4.11}$$

The model resolution matrix is then:

$$\mathbf{R} = \left(\mathbf{A}^T\mathbf{C}_d^{-1}\mathbf{A} + \mathbf{C}_m^{-1}\right)^{-1}\mathbf{A}^T\mathbf{C}_d^{-1}\mathbf{A}. \tag{4.12}$$

The resolution operator tells us to what extend we can retrieve the chosen model parameters independently from the inverse operator. The total number of independent parameters used to construct the estimated model is given by the trace of the resolution matrix.

An alternative approach is to add information only to the null-space of the unregularized inversion. The procedure of adding null-space information while retaining the data fit was originally proposed by Deal and Nolet (1996) for tomographic inverse problems. We consider this approach less flexible in dealing with data contaminated by noise, and therefore we only show results for the conventional implementation using regularization criteria shown in equation (4.11).

In the following sections we show that prior information given by a minimum variation criterion and energy criteria can be incorporated in the conventional formalism, i.e. we derive expressions for the prior model and for the prior model covariances for the proposed regularization criteria. The derivations are given for single component data, but are readily generalized for multicomponent data.

4.5.1 Minimum variation in common-offset domain

Prior information on the medium response can be obtained by requiring that variation in common-offset sections of the medium response is small. The underlying idea is that lateral source and receiver variations result in amplitude variations in common-offset sections. If we correctly retrieve these lateral source and receiver variations and correct the recorded data for these source and receiver effects, the amplitude variations in these common-offset sections of the medium response are reduced to the minimum required by the data. We define variation in the common-offset medium response using a measure of length (Menke, 1984):

$$\begin{aligned} L(\mathbf{x}_o) &= \left[\mathbf{m}_G(\mathbf{x}_o) - \boldsymbol{\mu}_G(\mathbf{x}_o)\right]^T\left[\mathbf{m}_G(\mathbf{x}_o) - \boldsymbol{\mu}_G(\mathbf{x}_o)\right] \\ &= \left[\mathbf{A}_l(\mathbf{x}_o)\mathbf{m}_G(\mathbf{x}_o)\right]^T\left[\mathbf{A}_l(\mathbf{x}_o)\mathbf{m}_G(\mathbf{x}_o)\right], \end{aligned} \tag{4.13}$$

where $\mathbf{m}_G(\mathbf{x}_o)$ denotes the partition of $\mathbf{m}_G$ with offset $\mathbf{x}_o$, and the elements of $\boldsymbol{\mu}_G(\mathbf{x}_o)$ are the average of $\mathbf{m}_G(\mathbf{x}_o)$:

$$\left[\mu_G(\mathbf{x}_o)\right]_j = \frac{\sum_{i=1}^{N(\mathbf{x}_o)}\left[m_G(\mathbf{x}_o)\right]_i}{N(\mathbf{x}_0)}, \qquad j = 1, \ldots, N(\mathbf{x}_o), \tag{4.14}$$

with $N(\mathbf{x}_o)$ the number of traces with offset $\mathbf{x}_o$. The matrix $\mathbf{A}_l(\mathbf{x}_o)$ is the coefficient matrix, and is defined such that $\mathbf{A}_l(\mathbf{x}_o)\mathbf{m}_G(\mathbf{x}_0) = \mathbf{m}_G(\mathbf{x}_o) - \boldsymbol{\mu}_G(\mathbf{x}_o)$.

We define the minimum variation cost function L by combining all common-offset sections, using the number of traces in each common-offset section as weights, i.e. this criterion provides more reliable information using common-offset sections with many traces, since the mean and variation with respect to this mean value can be determined more accurately. The cost function is given by:

$$L = \sum_{\mathbf{x}_o} N(\mathbf{x}_o) L(\mathbf{x}_o) = \left[\mathbf{A}_l \mathbf{m}_G\right]^T \mathbf{W}_m \left[\mathbf{A}_l \mathbf{m}_G(\omega)\right]. \tag{4.15}$$

The coefficient matrix $\mathbf{A}_l$ comprises all individual matrices $\mathbf{A}_l(\mathbf{x}_o)$, and the diagonal matrix $\mathbf{W}_m$ contains the corresponding weighting factors $N(\mathbf{x}_0)$ and is normalized such that the maximum value of

$$\max\left[\mathbf{A}_l^T \mathbf{W}_m \mathbf{A}_l\right] = \frac{2}{N+1}. \tag{4.16}$$

This maximum is set equal to the ratio of the number of unknowns in $\mathbf{m}_R$ or $\mathbf{m}_S$ over $\mathbf{m}_G$. This normalization has been chosen to reduce the dependency of the damping parameters on the number of sources/receivers.

The minimum variation criterion can be included in the inverse problem [equations (4.9)], with the inverse of the medium-response model covariance given by:

$$\mathbf{C}_{m_G}^{-1} = \theta \mathbf{A}_l^T \mathbf{W}_m \mathbf{A}_l, \tag{4.17}$$

where θ is the overall damping parameter. We set the prior medium response

$$\mathbf{m}_G^0 = \mathbf{0}. \tag{4.18}$$

The choice of the prior medium response does not influence the inversion results when these are set to a constant value. This criterion minimizes differences with respect to the average value in common offset panels.

4.5.2 Energy criteria

Consider a common source gather for a source positioned at $\mathbf{x}_j$ with N receivers. The energy for frequency ω in this gather is proportional to the squared sum of all traces:

$$E(\omega, j) = \sum_{i=1}^{N} \left|v(\omega, i, j)\right|^2. \tag{4.19}$$

Inserting the convolutional model [equation (4.2)] into equation (4.19) yields:

$$E(\omega, j) = \left|S(\omega, j)\right|^2 \left(\sum_{i=1}^{N} \left|R(\omega, i)\right|^2 \left|G(\omega, i, j)\right|^2\right). \tag{4.20}$$

The energy in the common-source gather for the adjacent source position, with geophones positioned at similar offsets, is given by:

$$E(\omega, j+1) = |S(\omega, j+1)|^2 \left(\sum_{i=1}^{N} |R(\omega, i+1)|^2 \, |G(\omega, i+1, j+1)|^2 \right). \quad (4.21)$$

For closely spaced sources, we may assume that differences in the medium response only occur close to these sources. This implies that energy differences between two adjacent common source gathers are then primarily attributed to differences at the source. This leads to the following approximation for the energy difference between two adjacent common source gathers:

$$E(\omega, j+1) - E(\omega, j) \approx \left[|S(\omega, j+1)|^2 - |S(\omega, j)|^2 \right] \times \frac{1}{2} \left\{ \sum_{i=1}^{N} |R(\omega, i)|^2 |G(\omega, i, j)|^2 + |R(\omega, i+1)|^2 |G(\omega, i+1, j+1)|^2 \right\}. \quad (4.22)$$

The last term in equation (4.22) is the average of the medium response and the receiver terms of the two adjacent common source gathers [equations (4.20) and (4.21)]. It is assumed that this accurately represents the medium and receiver responses for both sources.

Using a similar approximation for $E(\omega, j+1) + E(\omega, j)$, we obtain for the division of the energy difference by its sum:

$$\frac{E(\omega, j+1) - E(\omega, j)}{E(\omega, j+1) + E(\omega, j)} \approx \frac{|S(\omega, j+1)|^2 - |S(\omega, j)|^2}{|S(\omega, j+1)|^2 + |S(\omega, j)|^2}. \quad (4.23)$$

Equation (4.23) is equivalent to

$$|S(\omega, j+1)|^2 - \frac{E(\omega, j+1)}{E(\omega, j)} |S(\omega, j)|^2 = 0. \quad (4.24)$$

We obtain expressions in the log/Fourier domain by taking the natural logarithm of equation (4.24):

$$\tilde{S}(\omega, j+1) - \tilde{S}(\omega, j) = \frac{1}{2} \log \left[\frac{E(\omega, j+1)}{E(\omega, j)} \right], \quad (4.25)$$

where the energy term on the right of equation (4.25) is calculated from the data alone. Hence, this equation imposes additional data-derived constraints on the source terms. Since we can only solve for relative source variations, we can impose a zero-mean constraint on the source terms. This imposes an artificial absolute scale on the Green's functions which is always required in seismic data processing. Equation (4.25) can be written in matrix-vector form:

$$\mathbf{A}_0 \mathbf{m}_S^0(\omega) = \mathbf{d}_S^0(\omega), \quad (4.26)$$

where $\mathbf{m}_S^0(\omega)$ contains the prior source variations, $\mathbf{d}_S^0(\omega)$ is the data vector, and $\mathbf{A}_0$ is the coefficient matrix. We obtain the prior model estimate for $\mathbf{m}_S^0$ using the least-squares solution of equation (4.26).

A similar analysis can be performed in the common-receiver domain. This results in the following system of equations for the prior receiver terms:

$$\tilde{R}(\omega, i+1) - \tilde{R}(\omega, i) = \frac{1}{2} \log \left[\frac{E(\omega, i+1)}{E(\omega, i)} \right]. \tag{4.27}$$

Equation (4.27) in matrix-vector form is written as:

$$\mathbf{A}_0 \mathbf{m}_R^0(\omega) = \mathbf{d}_R^0(\omega), \tag{4.28}$$

where $\mathbf{m}_R^0(\omega)$ contains the prior receiver model parameters, and $\mathbf{d}_R^0(\omega)$ is the data vector.

We use the covariance matrices $\mathbf{C}_{m_R}$ and $\mathbf{C}_{m_S}$ to impose the energy criteria upon the model vector. We define these as:

$$\mathbf{C}_{m_R}^{-1} = \frac{2\theta\phi\lambda\, \mathbf{A}_0^T \mathbf{A}_0}{\max\left[\mathbf{A}_0^T \mathbf{A}_0\right]}, \tag{4.29}$$

$$\mathbf{C}_{m_S}^{-1} = \frac{2\theta\phi(1-\lambda)\, \mathbf{A}_0^T \mathbf{A}_0}{\max\left[\mathbf{A}_0^T \mathbf{A}_0\right]}, \tag{4.30}$$

where θ is the overall damping parameter, The smaller the value of θ, the more the model parameters are allowed to vary around the energy and minimum variation constraints, and the better the data can be explained. The parameter ϕ determines the strength of the energy criteria relative to the variation criterion, and λ controls the relative strength of the energy criteria applied in the common-source domain compared to the common-receiver domain, and may take values between 0 and 1. The denominator in equation (4.29) and (4.30) is used to reduce the dependency of the damping parameters ϕ and λ on the number of sources/receivers considered in the inverse problem.

4.6 Synthetic example

We illustrate the method with a synthetic example on single component data, and analyze the influence of the selection of the damping parameters.

4.6.1 Data description

Consider the model shown in Figure 4.2 with a synclinal structure and lateral heterogeneity close to the free surface ($z = 0$ m). The model parameters are listed in Table 4.1. Synthetic data were computed with a viscoelastic finite-difference code (Robertsson et al., 1994). The first source and receiver are positioned at 100 m, the last ones at 900 m. The shot and receiver spacing is 20 m: there are 41 source and receiver positions. Both sources and receivers are located at the free surface. The source mechanism is a vertical

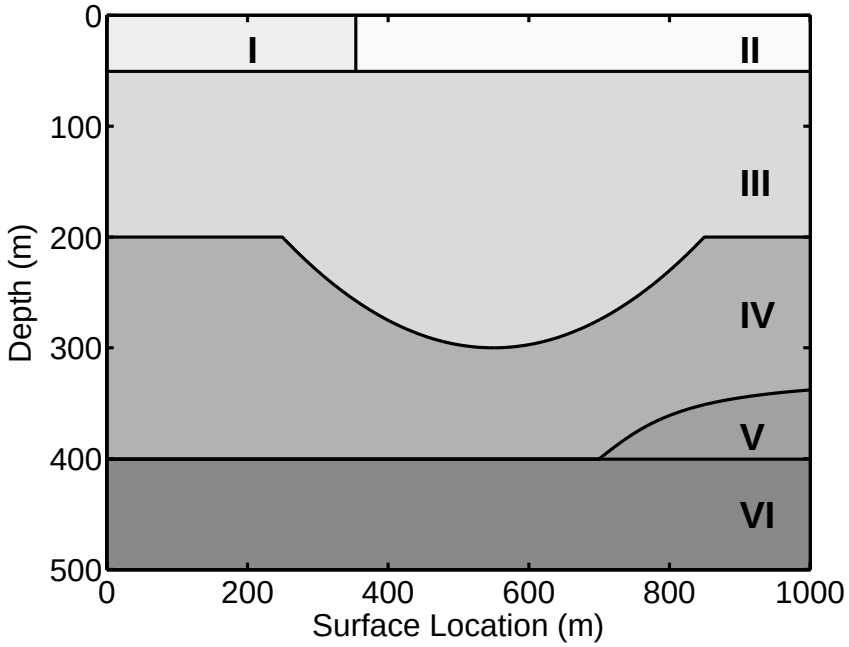

Figure 4.2: Synclinal model used to generate synthetic data, with layers numbered for identification.

Layer number	α (m s^{-1})	β (m s^{-1})	ρ (kg m^{-3})	Q_p	Q_s
I	1100	280	1700	100	50
II	900	250	1600	100	50
III	1500	400	2000	10000	10000
IV	2200	600	2100	10000	10000
V	2500	700	2150	10000	10000
VI	3000	800	2200	10000	10000

Table 4.1: Values for velocity, density, and attenuation for each layer in the model shown in Fig. 4.2.

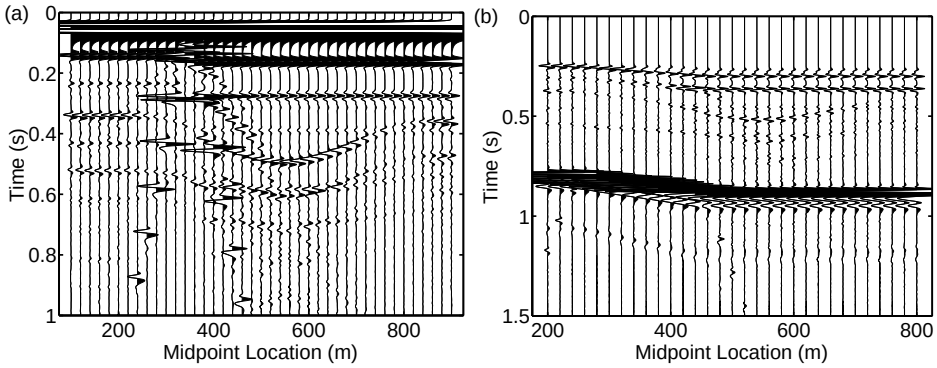

Figure 4.3: Common-offset panels for (a) 0 m and (b) 200 m offset. The midpoint coordinate is denoted by $\mathbf{x}_m$.

force source, which emits a Ricker wavelet with a 40 Hz central frequency. The time sampling interval is 0.001 s, and a trace has 4000 samples.

Two common-offset panels of the data are shown in Figure 4.3. The ground-roll is the most energetic event in the data. The near-surface lateral heterogeneity results in different amplitudes and traveltimes in the P-P reflected waves between 0.10 and 0.20 s, and causes backscattering of surface waves. These are the steeply dipping events between $x = 200$ and 500 m in the zero-offset section. The synclinal structure is easily recognized in the zero-offset panel. The structure is repeated due to reverberations in the near-surface low velocity layer. The 200 m common-offset panel shows that the near-surface heterogeneity results in different moveout velocities for the ground roll, which are the large amplitude events between 0.8 and 1.0 s. The signature of the synclinal structure is less pronounced in this section.

At the receiver side, data are perturbed using a damped harmonic oscillator description. This represents both the response of the geophone-ground coupling, and of the instrument response (Hoover and O'Brien, 1980; Krohn, 1984). The complex response can be written as:

$$R(f) = \frac{-\left(\frac{f}{f_g}\right)^2 \left[1 + i\left(\frac{f}{f_c}\right)\eta_c\right]}{\left[1 - \left(\frac{f}{f_g}\right)^2 + i\left(\frac{f}{f_g}\right)\eta_g\right]\left[1 - \left(\frac{f}{f_c}\right)^2 + i\left(\frac{f}{f_c}\right)\eta_c\right]}. \tag{4.31}$$

In this model, f_g and f_c are the resonant frequencies, and η_g and η_c are the damping factors for the geophone's internal spring, denoted with subscript g, and for the geophone ground coupling, indicated with subscript c. Critical damping occurs when η_g or $\eta_c = 2$. In this equation, i denotes the imaginary unit $\sqrt{-1}$.

We also used a damped harmonic oscillator description to represent the coupling of

	f_c (Hz)	f_g (Hz)	f_s (Hz)	η_c	η_g	η_s
μ	150	4.5	150	1.0	1.0	1.0
σ	50	0.5	50	0.2	0.2	0.2

Table 4.2: Values for average resonant frequencies and damping factors of source and receiver perturbations and the corresponding standard deviations.

the source (vertical vibrator) to the ground (Sallas, 1984)[1]:

$$S(f) = \frac{-\left[1 + i\left(\frac{f}{f_s}\right)\eta_s\right]}{\left[1 - \left(\frac{f}{f_s}\right)^2 + i\left(\frac{f}{f_s}\right)\eta_s\right]}, \tag{4.32}$$

where f_s and η_s are source coupling resonant frequency and damping parameter. For each source and geophone, the resonant frequencies and damping parameters are selected randomly from a Gaussian distribution. The parameters which characterize these distributions are listed in Table 4.2.

We only used the damped-oscillator description for the source and receiver perturbations in these synthetic examples. The inversion method does not use any constraints that follow from this model, and is thus independent from the damped-oscillator parameterization.

Since we are only able to solve for relative source and receiver perturbations in the log/Fourier domain, we decompose the source and receiver terms into an average and a perturbation term:

$$R(\omega, i) = \bar{R}(\omega)\left[1 + \frac{\Delta_R(\omega, i)}{\bar{R}(\omega)}\right] = \bar{R}(\omega)\Delta'_R(\omega, i), \tag{4.33}$$

$$S(\omega, j) = \bar{S}(\omega)\left[1 + \frac{\Delta_S(\omega, j)}{\bar{S}(\omega)}\right] = \bar{S}(\omega)\Delta'_S(\omega, j), \tag{4.34}$$

where $\bar{R}(\omega)$ is the geometric mean of the different receiver terms:

$$\bar{R}(\omega) = \left[\prod_{i=1}^{N} R(\omega, i)\right]^{1/N}. \tag{4.35}$$

The relative source and receiver terms (perturbations) are $\Delta'_S(\omega, j)$ and $\Delta'_R(\omega, i)$, respectively. The geometric mean in the Fourier domain corresponds to the arithmetic mean in the log/Fourier domain. In the inverse procedure, we only solve for the source and receiver perturbations $\Delta'_S(\omega, j)$ and $\Delta'_R(\omega, i)$, and therefore we only added the perturbation terms to the data.

[1] Note that we only consider the coupling of the baseplate to the ground in this example, which response is given by a damped harmonic oscillator description. We do not consider the mechanical model of the vibrator itself.

4.6.2 Results

We first study inversion results for a single frequency. To gain an idea of the influence of ϕ and λ on the model estimate, we minimize equation (4.9) many times, systematically varying the parameters ϕ and λ. We added errors to the data drawn from a Gaussian distribution with a standard deviation $\sigma_d = 0.10$ in the log/Fourier domain. This corresponds to errors with a standard deviation of 10 per cent of the values of the synthetic data in the frequency domain. The experiments are repeated with different manifestations of random noise. We performed experiments for different resonant frequencies and damping parameters for the source and receiver perturbations, and plot the reduced χ^2 as a function of independent parameters in the final model. We define the reduced χ^2 as:

$$\chi^2 = \frac{1}{N_D - M} \left(\mathbf{Am} - \mathbf{d}\right)^T \mathbf{C}_d^{-1} \left(\mathbf{Am} - \mathbf{d}\right), \tag{4.36}$$

where N_D is the number of data and $M = \text{trace}(\mathbf{R})$. Furthermore, we compare the estimated model to the true solution $\mathbf{m}_{true}$. We quantify the true-model misfit with

$$\xi^2 = \frac{(\tilde{\mathbf{m}} - \mathbf{m}_{true})^T (\tilde{\mathbf{m}} - \mathbf{m}_{true})}{N_U}, \tag{4.37}$$

where N_U is the number of unknown parameters. The measure ξ has been chosen such that it can be interpreted as an average uncertainty in the estimated model parameters.

Figure 4.4 shows misfit curves for the data and model uncertainty for $f = 50$ Hz. These misfit curves are computed varying the overall damping parameter θ, and consequently the trace of $\mathbf{R}$ using equation (4.12). If we reduce the overall damping θ, i.e. allowing more independent parameters in the inversion, the data are better explained, resulting in small values for χ^2. As we reduce the overall damping, χ^2 monotonically tends towards 1, as expected.

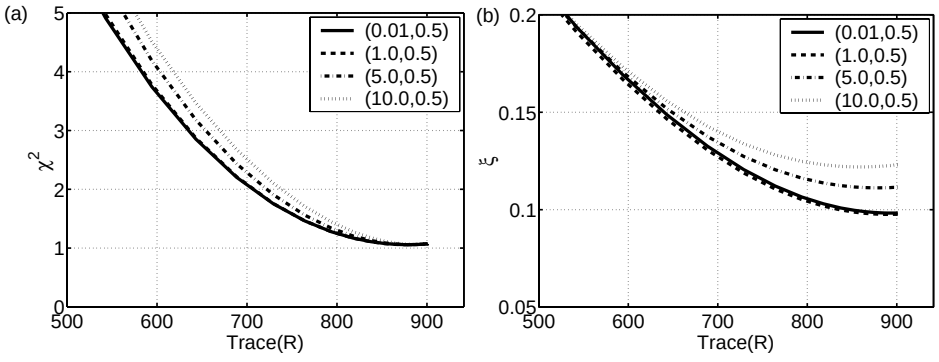

Figure 4.4: Misfit curves obtained for various source and receiver perturbations. The curves are labelled showing the values of the parameters (ϕ,λ). (a) shows the data misfit with the reduced chi-squared measure, and (b) shows the true model misfit.

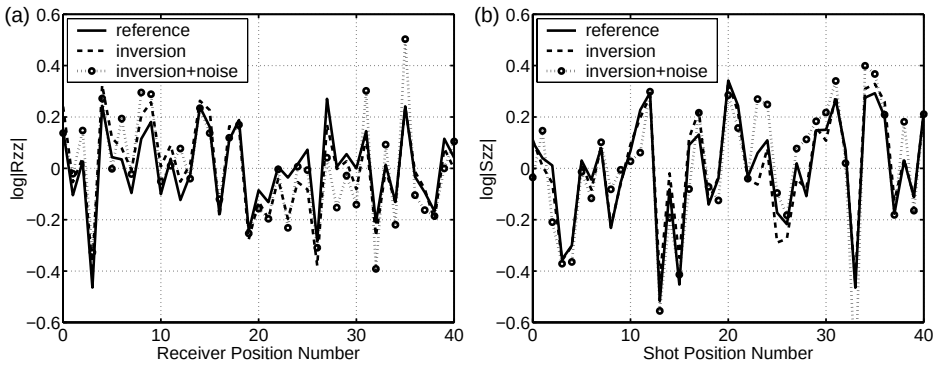

Figure 4.5: Inversion results for relative (a) receiver and (b) source perturbations at frequency $f = 50$ Hz. The inversion results are computed with the following damping parameter values: $\theta = 0.001$, $\phi = 0.01$, and $\lambda = 0.5$, which results in $trace(\mathbf{R}) \approx 901$, and are compared to the reference solution. Results are shown for unperturbed data, and for data contaminated with Gaussian noise.

Both the data and the model misfit measures indicate that best results are obtained if $\phi \leq 1$. For a fixed value of trace($\mathbf{R}$), the data are better explained for $\phi \leq 1$. For larger values, both the data and model misfit increase. The explanation for this is that the source and receiver terms are better constrained by the data than the individual medium response terms, i.e. all equations in a common-source gather constrain the individual source term, whereas there is only one equation for a particular Green's function. Thus, imposing prior information on the source and receiver terms potentially has a larger influence on data and model misfit than prior information on the medium response terms. Sensitivity tests for λ, the trade-off parameter between source and receiver terms, indicated that the inversion results are not influenced by variations in this parameter.

An example of the inversion for lateral source and receiver perturbations is shown in Figure 4.5. In Figure 4.5a, the ordinate value R_{zz} represents the vertical component of the receiver correction, and S_{zz} in Figure 4.5b represents the vertical component of the source correction. The frequency $f = 50$ Hz, and the damping parameter values are $\theta = 0.001$, $\phi = 0.01$ and $\lambda = 0.5$, resulting in trace($\mathbf{R}$) ≈ 901. Inversion results are shown for unperturbed data, and for data contaminated with Gaussian noise with standard deviation 0.10. In order to quantify the error, we use the measure $\xi_{R,S}$ for the source and receiver amplitude terms:

$$\xi^2_{R,S} = \frac{\left(\tilde{\mathbf{m}}_R - \mathbf{m}_{R\,true}\right)^T \left(\tilde{\mathbf{m}}_R - \mathbf{m}_{R\,true}\right) + \left(\tilde{\mathbf{m}}_S - \mathbf{m}_{S\,true}\right)^T \left(\tilde{\mathbf{m}}_S - \mathbf{m}_{S\,true}\right)}{2N} \tag{4.38}$$

For the unperturbed data, there is a good fit to the reference solution which is the true solution for the lateral source and receiver amplitude variations: $\xi_{R,S} = 0.083$. For the

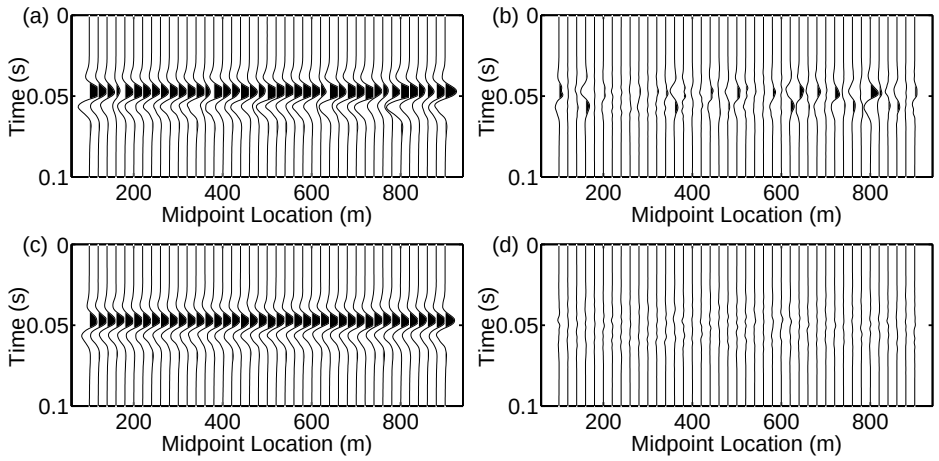

Figure 4.6: Effect of source and receiver amplitude corrections on zero offset data: focus on ground roll. Shown are (a) perturbed data, (b) difference between perturbed data and reference solution, (c) corrected data, and (d) difference between these corrected data and reference solution.

data contaminated with Gaussian noise with standard deviation 0.10, the fit is slightly less good: $\xi_{R,S} = 0.098$.

Instead of using directly the inversion results for the medium response terms $\mathbf{m}_G$, we use the lateral source and receiver terms to compensate the recorded data for these effects. This approach is favoured since it allows the implementation of the additional requirement that the source and receiver terms have a finite impulse response (e.g. Drijkoningen; 2000), which was not imposed explicitly in our implementation. Thus, the compensation scheme consist of the following steps: first we estimate the filters which compensate for lateral source and receiver variations in the log/Fourier domain. These inverse filters are obtained by reversing the sign of the obtained source and receiver perturbations terms in the log/Fourier domain. Then, we apply the inverse log/Fourier transform and limit the impulse response in the time domain. This operation is performed such that the resulting filters are zero phase, and the filter length in the presented examples is set to 0.03 s. Finally, we correct the recorded data for lateral source and receiver amplitude variations by convolution in the time domain.

We illustrate the performance of this compensation scheme on the synthetic data described in the previous section. We added errors drawn from a Gaussian distribution with a standard deviation of 10 per cent of the values of the synthetic data in the time domain, followed by a low-pass filter with 100 Hz cut-off frequency, and use the same values of the damping parameters as in the previous example. Figures 4.6 and 4.7 show the results on the recorded zero-offset data. Figure 4.6 shows the results of the first arrival. The amplitudes in Figure 4.7 are blown up to focus on the reflected waves.

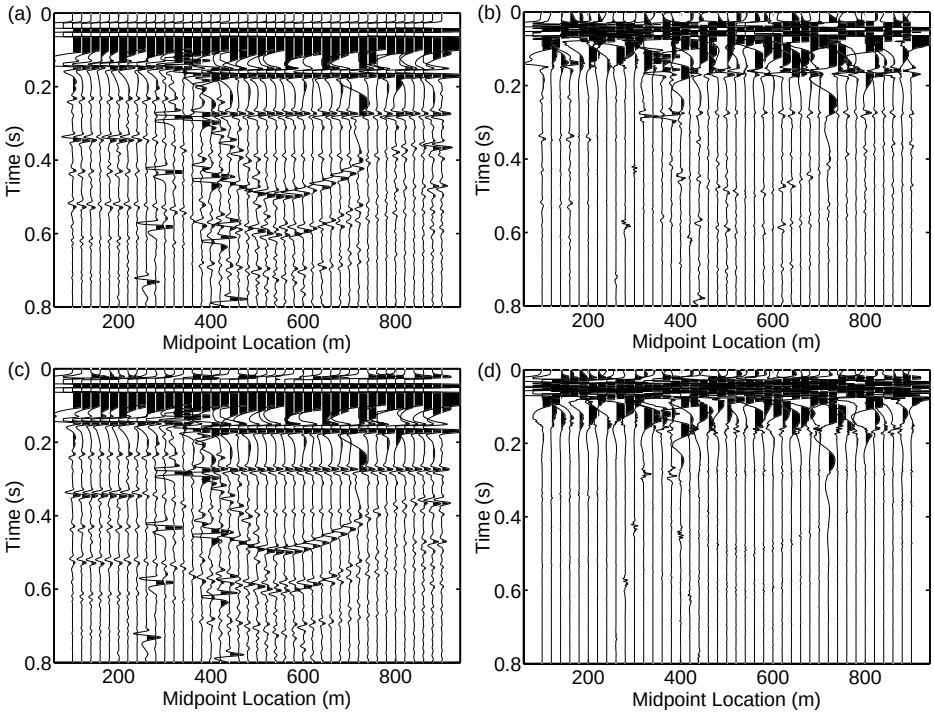

Figure 4.7: Effect of source and receiver amplitude corrections on zero offset data: focus on reflected waves. Shown are (a) perturbed data, (b) difference between perturbed data and reference solution, (c) corrected data, and (d) difference between corrected data and reference solution.

The results are compared to a reference solution which *includes* the phase shifts induced by the lateral source and receiver variations and the average source and receiver terms. Thus, the reference solution is the input data which are compensated for the lateral source and receiver amplitude variations, and do not contain the additional Gaussian errors. The phase differences are included in the reference solution to be able to demonstrate the performance of the amplitude correction scheme. Otherwise, we would obtain differences between the compensated data and the reference solution due to the phase differences for which we do not compensate.

Both for the first arrival and for the reflected waves, the differences of the corrected solution with the reference solution are significantly smaller than for the perturbed data. The large errors in the first 0.2 seconds of Figure 4.7d correspond to the residue shown in Figure 4.6d.

Similar results are obtained for amplitude corrections for 200 m offset data. (Figures 4.8 and 4.9). Amplitude errors in both the ground roll and the reflected waves are reduced.

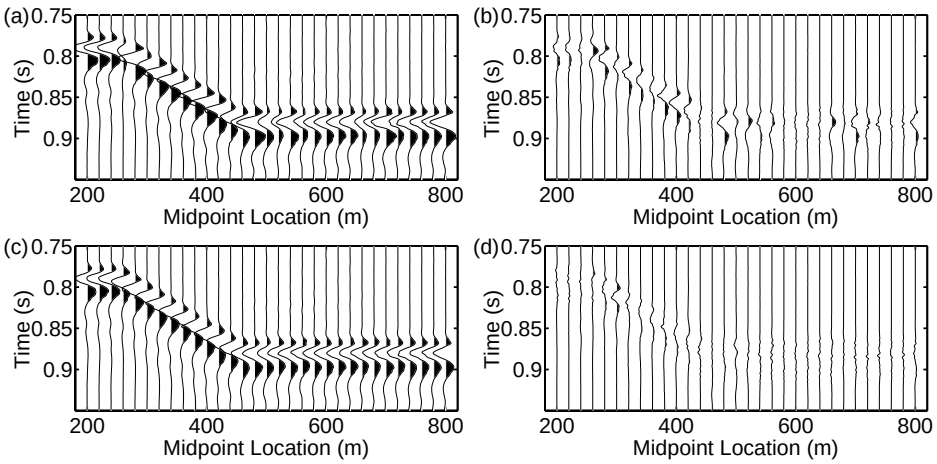

Figure 4.8: Effect of source and receiver amplitude corrections on 200 m offset data: focus on ground roll. Shown are (a) perturbed data, (b) difference between perturbed data and the reference solution, (c) corrected data, and (d) difference between these corrected data and the reference solution.

A comparison of the energy differences with the reference solution before and after the amplitude corrections shows that the errors are significantly reduced. In the noise-free case, the relative energy difference $(E - E_{ref})/E_{ref}$, where E is the energy of all data traces before or after the amplitude corrections and E_{ref} is the energy of the reference solution, decreases from 0.079 to 0.0065. For data perturbed with the random noise (Gaussian noise; standard deviation 10 per cent of the values of the synthetic data), the relative energy differences before and after the amplitude corrections are 0.086 and 0.011, respectively.

This synthetic example demonstrates that the proposed technique significantly reduces effects of lateral source and receiver variations from the data, without having to select primary reflections and without prior structural information.

4.7 Discussion

The correction for lateral source and receiver variations is based on the assumption that the conditions for reciprocity are applicable to seismic data acquisition. In practice, however, positioning of sources and receivers at identical positions is difficult to realize. Moreover, we also need to consider an explosive source in addition to a vertical force source (vibrator), and source patterns are also commonly used in land seismics.

Fenati and Rocca (1984) conducted a field test to assess the applicability of reciprocity in the field using both explosive and vibratory sources. They observed a good coherence

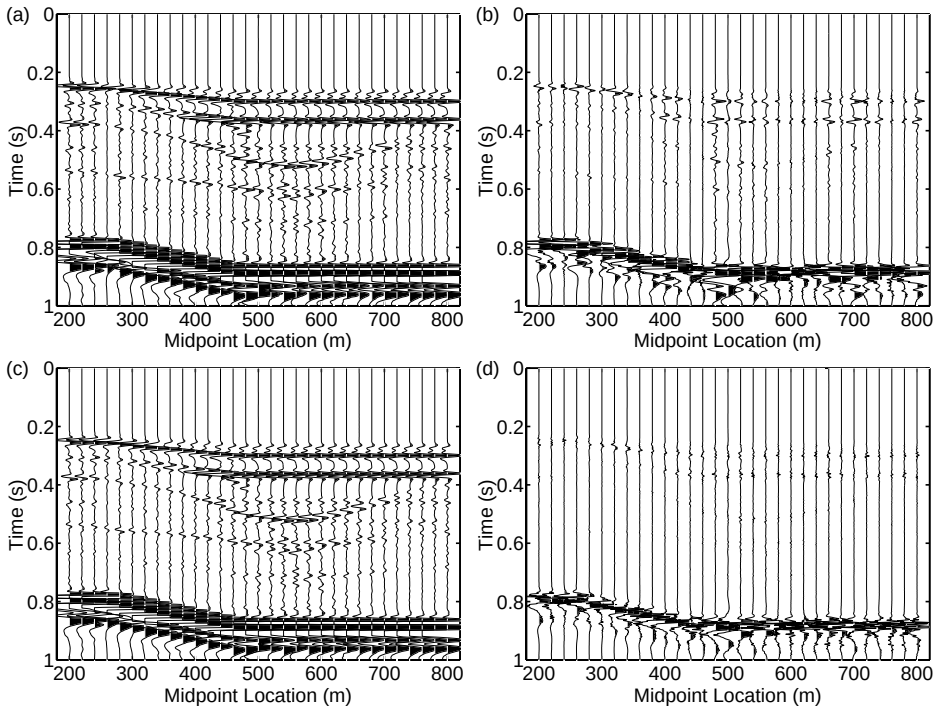

Figure 4.9: Effect of source and receiver amplitude corrections on 200 m offset data: focus on reflected waves. Shown are (a) perturbed data, (b) difference between perturbed data and the reference solution, (c) corrected data, and (d) difference between these corrected data and the reference solution.

between the direct and reciprocal traces regardless of the source, except at near-offsets and early times with explosive sources. Furthermore, we performed sensitivity tests to evaluate the effect of nonidentical source-receiver positions. These tests indicated that the results are not influenced by small differences in source and receiver positions when the distance between the reciprocal sources and receivers remains constant. For example, this allows sources at a shallow depth, while the receivers are positioned at the surface. We also expect that the results are not sensitive to a small displacement between parallel source and receiver lines.

It is important to realize that, contrary to conventional surface-consistent processing techniques (Taner and Koehler, 1981; Levin, 1989; Cambois and Stoffa, 1992; Cary and Lorentz, 1993), reciprocity constrains source and receiver effects only, which do not include wavefield propagation effects of the near surface. Thus, we assume that the amplitude perturbations for each source and receiver component are independent of the wave type and the angle of incidence. Since we do not include wavefield propagation effects

through the near-surface, surface consistency does not assume wave propagation in which seismic energy travels through the near-surface along vertical paths, as in static corrections. Therefore, the presence of ground roll in the data will not necessarily violate the surface-consistent assumption.

Application to field data requires the computation of $(\mathbf{A}^T\mathbf{C}_d^{-1}\mathbf{A}+\mathbf{C}_m^{-1})^{-1}$ [equation (4.11)]. In practice, however, the matrix will be too big to invert and to retain in memory. In such cases, the data should be decomposed into smaller sets, each of which would be processed separately. This is common practice in conventional surface-consistent processing techniques, and it is argued that this does not degrade the accuracy of the estimated operators (Wiggins et al., 1976; Cambois and Stoffa, 1992).

It should be explicitly stated that we do not impose the damped-oscillator description on the source and receiver terms. We only used this description in our synthetic experiments to obtain realistic amplitude perturbations. Therefore, this method can potentially be used to validate the damped-oscillator description for source and receiver coupling, and this could improve our understanding of source and receiver coupling effects in seismic data.

Finally, we only considered the decomposition of amplitudes into source, receiver, and medium response terms in the log/Fourier domain. Problems associated to the phase is that only the principal value of the original phase is known, which introduces discontinuities in the phase function. We did not succeed in finding a suitable regularization for the inverse problem to perform the decomposition of the phase in source, receiver, and medium response terms. This is subject of future research.

4.8 Concluding Remarks

Existing surface-consistent deconvolution techniques are applicable to primary reflection data only, and assume that common-depth point gathering is valid. Since multichannel filter operations, which are commonly used to suppress ground roll and multiples, are sensitive to source and receiver perturbations, corrections for these effects should be done in the early stages of the processing sequence.

We presented a preprocessing technique to compensate for these source and receiver perturbations which is applicable to the whole seismic trace. Furthermore, it does not impose additional requirements on the subsurface. The approach is based on reciprocity of the medium response, which implies that differences between normal and reciprocal recordings can be attributed to the source and receiver perturbations.

Reciprocity does not fully constrain lateral source and receiver amplitude perturbations. Additional information is required to obtain a unique solution to the inverse problem. We used a criterion based on minimizing energy total differences between adjacent common-source and receiver gathers, and based on minimizing variation in common-offset panels of the medium response.

We developed the theoretical framework both for single and multicomponent data. Synthetic tests on single component data demonstrated that this method significantly reduces the effects of lateral source and receiver variations.

Chapter 5

Equalization of source and receiver amplitude responses using reciprocity and waveform inversion – Application to land seismic data

Abstract

Source and receiver response equalization is necessary when their behavior or coupling changes with location within a given survey. Existing techniques which account for these effects, such as surface-consistent deconvolution, are applicable to primary reflection data only, thus requiring the suppression of ground roll and multiples prior to application. This is usually performed with multichannel filters, the performance of which degrade in the presence of source and receiver perturbations. We developed an alternative method to compensate for source and receiver perturbations which is purely a raw data preprocessing step: it is applicable to the whole seismic trace, hence does not require the isolation of primary reflections, and no assumptions are imposed on the subsurface. The method is based on reciprocity of the medium response. This implies that differences between normal and reciprocal recordings can be attributed to the source and receiver perturbations. We applied this technique to single sensor data acquired in Manistee County, Michigan. At this site, near-surface conditions vary, and this significantly affects the data quality. The application of the equalization procedure led to a substantial improvement in signal-to-noise ratio, on both prestack and poststack data. Furthermore, the source corrections are cor-

This chapter has been submitted by R. Van Vossen, A. Curtis, A. Laake and J. Trampert to *Geophysics*.

related to changes in near-surface conditions, in this case to changes in water-saturation levels. We did not observe such a correlation for the receiver corrections, which vary rapidly along the spread. Finally, the receiver response we found did not agree with the generally accepted damped harmonic oscillator model. For frequencies below 100 Hz, the retrieved receiver variations are larger than predicted by this model, and we cannot explain the receiver response using a single resonant frequency for the geophone-ground coupling.

5.1 Introduction

The variability of recordings obtained in land seismics settings cannot be fully explained using linear wave propagation models because it partially depends on changes in source and receiver behavior within a given survey. For example, the source strength and signature are mainly determined by nonlinear deformation of the near-source region. As a consequence, changing near-surface conditions deteriorate the so-called repeatability of the source (Karrenbach, 1994; Aritman, 2001). On the receiver side, several authors have reported discrepancies between signals recorded by geophones which are only a few meters apart (Berni and Roever, 1989; Blacquière and Ongkiehong, 2000). Some of the causes of these perturbations are imperfect geophone coupling, localized variations of the soil, shallow elastic property variations in consolidated rock, and variations of the ambient or recording equipment noise.

Detection and compensation for these perturbations are necessary in the early stages of processing, since the performance of multichannel filter operations rapidly deteriorates in presence of amplitude or phase perturbations. This was already recognized decades ago by Newman and Mahoney (1973), who demonstrated that the performance of the source and receiver arrays is sensitive to source and receiver perturbations. These arrays, or more generally multichannel or frequency-wavenumber filters, are commonly used for ground roll and multiple attenuation. As indicated by Kelamis and Verschuur (2000), successful multiple elimination requires careful preprocessing of the data.

Preferably, individual recordings are compensated for the source and receiver perturbations before group forming. Therefore, recordings of individual receivers are recommended (Ongkiehong and Askin, 1988; Ongkiehong, 1988), which in principle allow the compensation for each individual geophone prior to digital group forming. Moreover, digital group forming is a reversible process, maintaining flexibility during the processing stages.

Source and receiver perturbations do not only influence processing. They also bias amplitude interpretation techniques such as amplitude-versus-offset (AVO) (Castagna and Backus, 1993). Furthermore, these perturbations also directly influence the signal-to noise ratio of stacked data.

Even though compensation for acquisition effects should be done in the early stages of processing, existing surface-consistent deconvolution techniques are applicable to primary reflection data only (Taner and Koehler, 1981; Yu, 1985; Levin, 1989; Cambois and Stoffa, 1992; Cary and Lorentz, 1993), and thus require ground roll and multiple sup-

pression prior to the application. Furthermore, common depth point (CDP) gathering is assumed to be valid.

In contrast, we use an alternative approach to compensate for source and receiver perturbations, which is essentially a preprocessing step. In principle, it can be directly applied to the recorded wavefield because it uses the complete seismic trace instead of primary reflection data only. Furthermore, it does not require midpoint binning, and no assumptions are imposed on the subsurface. The approach uses reciprocity of the medium response for evaluating lateral source and receiver amplitude variations. As a result of reciprocity, differences between normal and reciprocal traces can be attributed to differences in source strength and receiver coupling. Karrenbach (1994) and Luo and Li (1998) applied this technique to determine the seismic source wavelet, assuming that the receiver perturbations can be neglected. Van Vossen et al. (2004b) demonstrated that the latter constraint is unrealistic and can be relaxed, adapting the procedure such that both source and receiver amplitude perturbations can be resolved.

Application of reciprocity requires symmetric data acquisition (Vermeer, 1991). This includes identical source and receiver positions and shot/receiver patterns, and identical source and receiver components. A field study performed by Fenati and Rocca (1984) indicated that in practice, these reciprocal conditions do not have to be met exactly. They observed that the fit between normal and reciprocal traces was not influenced by the choice of a vibratory or explosive source, except at short offsets. Furthermore, in case of a regular acquisition geometry with non-identical source and receiver positions, e.g. when a source is located between two adjacent receivers, interpolation can be used before determining the corrections.

In this paper, we first review the source and receiver equalization procedure proposed and tested synthetically by Van Vossen et al. (2004b). The main part of this paper is devoted to a field data application of this method. Data are acquired on a site in Manistee County, Michigan, which is characterized by changing near-surface conditions. Therefore, these data provide an excellent test case for the method. We discuss the characteristics of the source and receiver corrections obtained and we show that these are correlated to the near-surface conditions. Furthermore we show the influence of the amplitude corrections on both prestack and poststack data.

5.2 Source and receiver equalization procedure

5.2.1 Convolutional model and reciprocity

We discuss the equalization procedure for single component data, and denote the vertical component of the recorded particle velocity with $v(t, \mathbf{x}_s, \mathbf{x}_r)$, with $\mathbf{x}_s$ and $\mathbf{x}_r$ the source and receiver positions, respectively. The generalization for multicomponent data is given by van Vossen et al. (2004).

Considering the earth as a linear system for the propagation of seismic waves, the recorded traces satisfy the convolutional model,

$$v(t, \mathbf{x}_s, \mathbf{x}_r) = R(t, \mathbf{x}_r) * G(t, \mathbf{x}_s, \mathbf{x}_r) * S(t, \mathbf{x}_s), \tag{5.1}$$

where $R(t, \mathbf{x}_r)$ is the receiver response for the vertical component recordings at surface location $\mathbf{x}_r$, $S(t, \mathbf{x}_s)$ is the source signature at surface position $\mathbf{x}_s$, and $G(t, \mathbf{x}_s, \mathbf{x}_r)$ is the corresponding medium response. The asterisk ($*$) denotes convolution in the time domain.

The equalization procedure requires data acquisition in a geometry which allows the usage of apparently redundant recordings of reciprocal traces. Such a geometry requires symmetric wavefield sampling, that is data recorded using identical source and receiver sampling. This geometry was recommended by Vermeer (1991) to avoid processing artefacts as a result of asymmetric source and receiver sampling.

In the current application, the reciprocity theorem states that the medium response (or Green function) is invariant when the source and receiver positions are interchanged (Knopoff and Gangi, 1959). Reciprocity of the medium response is expressed as:

$$G(t, \mathbf{x}_s, \mathbf{x}_r) = G(t, \mathbf{x}_r, \mathbf{x}_s). \tag{5.2}$$

This identity requires that the source orientation is similar to the recorded particle velocity component.

Despite reciprocity of the medium response, large differences between normal and reciprocal traces are commonly observed in the field (Fenati and Rocca, 1984; Karrenbach, 1994). Karrenbach (1994) and Luo and Li (1998) explain these differences by lateral variations in source behavior only, assuming that differences in receiver behavior are small. We demonstrated that the latter constraint should be relaxed, and developed a procedure for compensating the recordings for lateral multicomponent source and receiver amplitude variations (Van Vossen et al., 2004b). In the following section we review the inverse procedure for estimating these corrections.

5.2.2 Formulation of the inverse problem

We assume that $R(t, \mathbf{x}_r)$ and $S(t, \mathbf{x}_s)$ are surface consistent. This means that effects associated with a particular source or receiver remain constant throughout the recording time, and affect all wave types similarly, regardless of the direction of propagation. The time dependence in $R(t, \mathbf{x}_r)$ and $S(t, \mathbf{x}_s)$ denotes the length of the finite-impulse response filters.

Let us assume that we have data recorded with N identical source and receiver positions. Then, the convolutional model and reciprocity result in a system of equations which constrain the individual terms in the convolutional model. Similar to surface-consistent deconvolution, we can formulate a linear inverse problem in the log/Fourier domain (Taner and Koehler, 1981; Cambois and Stoffa, 1992), where log denotes the natural logarithm. The log/Fourier transform of a time function $X(t)$ is defined as

$$\tilde{X}(\omega) = \log \left[\int_{-\infty}^{\infty} X(t) e^{-i\omega t} \mathrm{d}t \right], \tag{5.3}$$

with the inverse transform

$$X(t) = \frac{1}{2\pi} \int_{-\infty}^{\infty} e^{\tilde{X}(\omega) + i\omega t} \mathrm{d}\omega. \tag{5.4}$$

Since convolution in the time domain is equivalent to summation in the log/Fourier domain, the convolutional model becomes in the log/Fourier domain:

$$\tilde{V}(\omega, \mathbf{x}_s, \mathbf{x}_r) = \tilde{R}(\omega, \mathbf{x}_r) + \tilde{G}(\omega, \mathbf{x}_s, \mathbf{x}_r) + \tilde{S}(\omega, \mathbf{x}_s). \tag{5.5}$$

The real part of equation (5.5) describes the decomposition of the natural logarithm of the Fourier amplitude spectra into the source, receiver, and medium response terms, whereas the imaginary part of equation (5.5) gives the decomposition of the phase. In the following, we only consider the amplitude component of the problem.

For the analysis of the system of equations, it is convenient to recast equation (5.5) in a matrix-vector form:

$$\mathbf{A}\mathbf{m}(\omega) = \mathbf{d}(\omega), \tag{5.6}$$

where $\mathbf{A}$ is the coefficient matrix, $\mathbf{m}(\omega)$ contains the unknown parameters in the log/Fourier domain, and the data-vector $\mathbf{d}(\omega)$ contains the measurements of the wavefield $\tilde{V}(\omega, \mathbf{x}_s, \mathbf{x}_r)$ for all source and receiver positions. The "model" vector $\mathbf{m}(\omega)$ is partitioned into the individual components:

$$\mathbf{m}(\omega) = \begin{pmatrix} \mathbf{m}_G(\omega) \\ \mathbf{m}_R(\omega) \\ \mathbf{m}_S(\omega) \end{pmatrix}, \tag{5.7}$$

where $\mathbf{m}_G(\omega)$ contains the medium response, $\mathbf{m}_R(\omega)$ the receiver terms, and $\mathbf{m}_S(\omega)$ the source wavelets. The coefficient matrix $\mathbf{A}$ is frequency independent, containing only ones and zeros.

We treat reciprocity of the medium response as an exact relationship. Instead of inserting the reciprocal equations (5.2) in the coefficient matrix $\mathbf{A}$, we directly reduce the number of unknown parameters in $\mathbf{m}_G(\omega)$ by explicitly substituting the reciprocal medium response terms using equation (5.2). Since the number of unknowns is reduced, this approach is computationally favorable.

Furthermore, we can only solve for *relative* source and receiver differences. Consequently, we can impose a zero-mean constraint on the source and receiver terms without loss of generality. We also treat this as an exact relationship and implement it in a similar fashion to the reciprocity constraints.

5.2.3 Regularization criteria

Additional information is required to obtain a unique solution to the inverse problem. We use a criterion which minimizes variation in common-offset sections of the medium response (van Vossen et al. 2004). Prior information (or the reference model), denoted by $\mathbf{m}^0$, is included in the inverse problem defining a cost function:

$$Y = (\mathbf{A}\mathbf{m} - \mathbf{d})^T \mathbf{C}_d^{-1} (\mathbf{A}\mathbf{m} - \mathbf{d}) + \left(\mathbf{m} - \mathbf{m}^0\right)^T \mathbf{C}_m^{-1} \left(\mathbf{m} - \mathbf{m}^0\right), \tag{5.8}$$

where $\mathbf{C}_d^{-1}$ is the inverse of the data covariance matrix which we take to be diagonal, and $\mathbf{C}_m^{-1}$ is the inverse of the prior model covariance matrix. It is a block-diagonal matrix and can be written in partitioned form:

$$\mathbf{C}_m^{-1} = \theta \begin{pmatrix} \mathbf{C}_{m_G}^{-1} & \mathbf{0} & \mathbf{0} \\ \mathbf{0} & \mathbf{C}_{m_R}^{-1} & \mathbf{0} \\ \mathbf{0} & \mathbf{0} & \mathbf{C}_{m_S}^{-1} \end{pmatrix}, \tag{5.9}$$

where $\mathbf{C}_{m_G}$, $\mathbf{C}_{m_R}$ and $\mathbf{C}_{m_S}$ are the covariance matrices describing prior information on the medium response, receiver, and source terms, respectively, and θ is the overall damping parameter. The least squares solution of equation (5.8) is found by setting the derivatives with respect to the model parameters equal to zero, and is given by (e.g. Tarantola, 1987):

$$\tilde{\mathbf{m}} = \left(\mathbf{A}^T\mathbf{C}_d^{-1}\mathbf{A} + \mathbf{C}_m^{-1}\right)^{-1}\left(\mathbf{A}^T\mathbf{C}_d^{-1}\mathbf{d} + \mathbf{C}_m^{-1}\mathbf{m}^0\right). \tag{5.10}$$

Prior information on the medium response can be obtained by minimizing variation in common-offset sections of the medium response. The underlying idea is that lateral source and receiver variations result in amplitude variations in common-offset sections. If we correctly retrieve these lateral source and receiver variations and correct the recorded data for those effects, the amplitude variations in the common-offset sections of the medium response are reduced to the minimum required by the data. We give the corresponding expressions for $\mathbf{m}_G^0$ and for $\mathbf{C}_{m_G}$ in section 4.5.1.

In order to obtain a unique solution to the inverse problem, it is not necessary to provide prior information on the source and receiver terms, so we used

$$\mathbf{m}_R = \mathbf{0}, \qquad \mathbf{C}_{m_R}^{-1} = \mathbf{0}, \tag{5.11}$$

$$\mathbf{m}_S = \mathbf{0}, \qquad \mathbf{C}_{m_S}^{-1} = \mathbf{0}. \tag{5.12}$$

Alternatively, we could have used the energy criteria, minimizing energy differences between two adjacent common source and common receiver gathers. These criteria are explained in detail by van Vossen et al. (2004). Our choice for the minimum variation criterion was based on synthetic tests. On synthetic data, best results were obtained using minimum variation as a regularization criterion.

5.2.4 Filtering procedure

Instead of using directly the inversion results found in equation (5.10) for the medium response terms $\mathbf{m}_G$, we use the lateral source and receiver terms to compensate the recorded data for these effects. This approach is favored since it allows the implementation of the additional requirement that the source and receiver terms have a finite impulse response (e.g. Drijkoningen; 2000), which was not imposed explicitly in our implementation. Thus, the equalization procedure consists of the following steps: first we estimate the filters which compensate for lateral source and receiver variations in the log/Fourier domain. These inverse filters are obtained by reversing the sign of $\tilde{\mathbf{m}}_R$ and $\tilde{\mathbf{m}}_S$ in the

log/Fourier domain. Then, we apply the inverse log/Fourier transform and limit the impulse response in the time domain by tapering and truncating the obtained filter. This operation is performed such that the resulting filters are zero phase, and the filter length is set to 0.04 s. This is a good approximation, because these filters are sharply peaked around $t = 0$. Finally, we correct the recorded data for lateral source and receiver amplitude variations by convolution in the time domain.

5.3 Application to Michigan field data

5.3.1 Data description

We illustrate the method on single sensor data acquired in Manistee County, Michigan. The site is characterized by changing near-surface conditions along the acquisition line. As indicated in Figure 5.1, near-surface conditions change from moist-to-wet sediments between 0 and 600 m to dry sands beyond that point (noted at time of acquisition). The location of the dry sands coincides with the more elevated sections along the acquisition line. Both source and receiver spacing is 10 m. The wavefield is emitted by an array of explosive sources which are located at approximately 5 ft depth. The receivers are 10 Hz geophones.

The conditions for application of the source and receiver equalization method are not exactly met. There are small differences between source and receiver locations (of the order of a few meters), and the radiation pattern of the shot pattern will differ from the sensitivity kernel of the vertical component recordings. We assume that we can still treat reciprocity as an exact relationship for determining the source and receiver corrections. Furthermore, an important aspect of the acquisition is that each geophone was deployed at only one surface location, i.e. the location of a geophone was fixed during the whole survey.

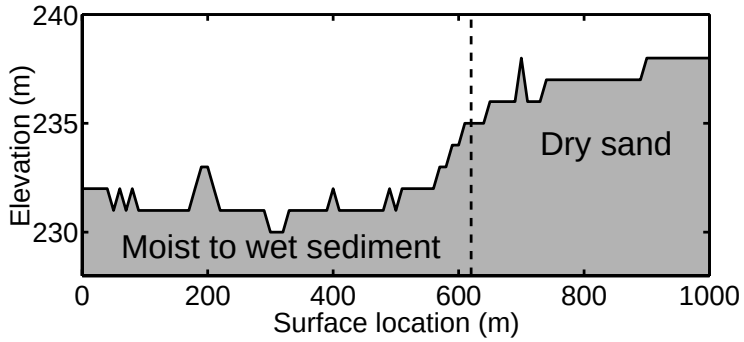

Figure 5.1: Surface topography and indication of near-surface material properties along the acquisition line.

5.3.2 Preliminary processing

In principle, the equalization procedure can be directly applied to recorded data. We only performed trace editing to remove void records, and muted acausal noise in a few traces. In case of non-identical source-receiver positions, data interpolation is required. We did not have to apply data interpolation before the equalization procedure in this application.

5.3.3 Characteristics of source and receiver corrections

As indicated by the synthetic experiments performed by van Vossen et al. (2004), best results are obtained when the source and receiver terms are computed using a weak regularization term. The examples shown here are obtained using $\theta = 1$ [equation (5.9)].

Figure 5.2 shows the correction terms for lateral source and receiver variations for the frequencies 20, 40, and 60 Hz. The receiver terms vary rapidly from point-to-point along the spread, whereas the source terms closely follow the changes in near-surface conditions (see Figure 5.1). Values larger than one correspond to corrections which increase the relative source strength, whereas values smaller than one indicate a relative energy decrease. Thus, we found that a source located in the dry sand is strongly attenuated compared to a source in moist-to-wet sediments. This can be explained by high energy absorption rates and nonlinear deformation in the near-source region for a source located in the dry sand (Aritman, 2001). When sediments are water-saturated, the compressibility dramatically changes, resulting in low energy absorption rates close to the source.

Figure 5.3 shows the frequency dependency of the source corrections. For frequencies below 20 Hz, ground roll is dominant in the recordings. At these frequencies, the source corrections do not only reflect the source coupling, but also the success or failure of the suppression of ground roll by the source arrays. The smallest source corrections are obtained at $f = 20$ Hz. For higher frequencies, the behaviour of the sources in the dry sand (for $x > 600$ m) clearly differs from the sources in the moist-to wet sediments: the

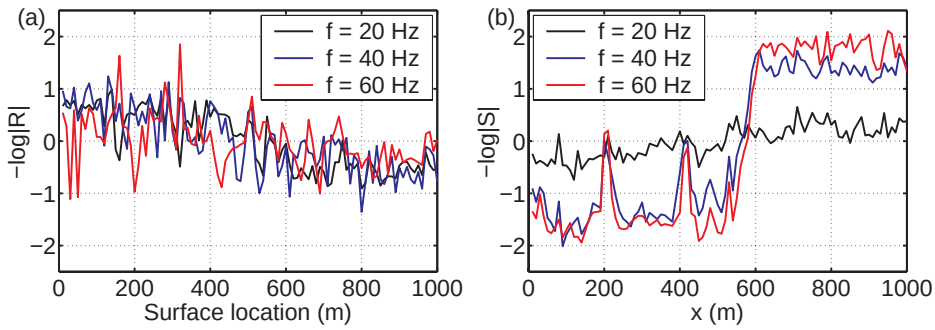

Figure 5.2: (a) Receiver and (b) source amplitude corrections along the acquisition line for different frequencies.

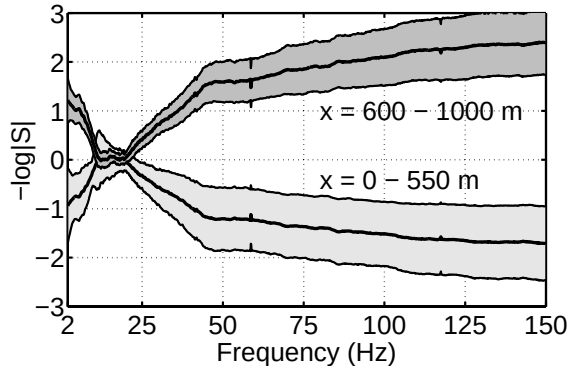

Figure 5.3: Source amplitude corrections as a function of frequency. The average corrections are given for the source corrections in the intervals between 0 and 550 m and between 600 and 1000 m, and the grey areas indicate the regions with at most one standard deviation difference with the average values.

source is strongly attenuated in the dry sand, and this pattern is found for all frequencies higher than 25 Hz. Note that we solve only for relative source corrections, requiring that the average source corrections is equal to zero in the log/Fourier domain. Consequently, the shape of the average response curve in the dry sand resembles the negated average response curve for the sources in the moist-to-wet sediments.

Figure 5.4a shows four examples of the frequency dependency of the receiver corrections which are obtained in the inversion stage. The receiver corrections are smaller than the source corrections. Furthermore, the receiver corrections do not only vary rapidly with offset, but also with frequency. Limiting the impulse response in the time domain corresponds to a smoothing operation in the frequency domain. Figure 5.4b shows the effect of limiting the impulse response to 0.04 s: these filters are used to correct the data for the receiver perturbations. The shape of the correction filters above 125 Hz are a result of cosine tapers which are applied to avoid artefacts in the inverse log/Fourier transform.

Because we have obtained only relative receiver corrections, we cannot compare these receiver corrections directly with the damped harmonic oscillator description, which is commonly used to describe geophone-ground coupling (Hoover and O'Brien, 1980; Krohn, 1984). However, we can compare ratios of the obtained corrections (differences in the log/Fourier domain) to ratios between two damped harmonic oscillators with different damping factors and resonant frequencies. Examples of differences of the retrieved receiver corrections are shown in Figure 5.4c, and the corresponding receiver locations are listed in Table 5.1. Figure 5.4d shows differences between synthetic damped harmonic oscillator curves (see equation (4.31) in Section 4.6.1) in the log/Fourier domain. The resonant frequencies and damping parameters are listed in Table 5.2. The spring of a geophone has typical resonance frequencies below 20 Hz (In this experiment, 10 Hz geo-

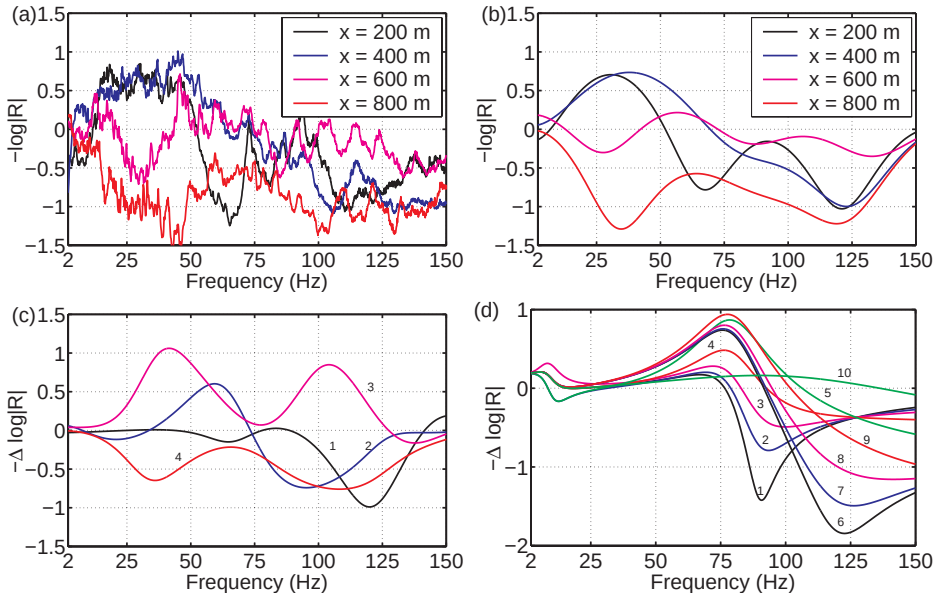

Figure 5.4: (a) Examples of obtained receiver amplitude corrections at different locations, and (b) shows the frequency response of these filters after limiting the impulse response to 0.04 s. Plot (c) shows differences between obtained receiver correction filters. The receiver positions corresponding to the labels are given in Table 5.1. Plot (d) shows differences between synthetic damped-harmonic oscillator amplitude response curves. The resonant frequencies and damping factors which correspond to these curves are listed in Table 5.2

phones were deployed), whereas the ground coupling for a vertical geophone is thought to resonate above 100 Hz (Hoover and O'Brien, 1980; Krohn, 1984). The curves in Figure 5.4d are dominated by ground coupling with one bounded minimum and maximum value at high frequencies. The retrieved receiver corrections (Figure 5.4c) show different characteristics: curves 3 and 4 have two distinct minima or maxima. On the other hand, curves 1 and 2 have one bounded minimum and maximum, and this qualitatively agrees with the damped-harmonic oscillator model. However, to explain curve 2 with this model, a 60 Hz resonant frequency is required, and this is much lower than the resonant frequencies which are reported for a vertical geophone Hoover and O'Brien (1980); Krohn (1984). As a consequence, the damped-harmonic oscillator model only predicts significant perturbations in the high-frequency range, whereas the retrieved receiver corrections are large at lower frequencies as well. Thus, the retrieved receiver corrections are inconsistent with the damped-harmonic oscillator model which is commonly used to describe geophone-ground coupling.

curve	location 1	location 2
1	200 m	210 m
2	400 m	410 m
3	600 m	610 m
4	800 m	810 m

Table 5.1: Locations of the receivers for which the obtained response difference is plotted in Figure 5.4c.

curve	$f_c^{(1)}$	$\eta_c^{(1)}$	$f_g^{(1)}$	$\eta_g^{(1)}$	$f_c^{(2)}$	$\eta_c^{(2)}$	$f_g^{(2)}$	$\eta_g^{(2)}$
1	80	0.3	10	1.0	90	0.1	11.0	1.0
2	80	0.3	10	1.0	90	0.2	11.0	0.8
3	80	0.3	10	1.0	90	0.3	11.0	1.2
4	80	0.3	10	1.0	90	0.5	11.0	1.0
5	80	0.3	10	1.0	90	1.0	11.0	0.8
6	80	0.3	10	1.0	120	0.2	11.0	1.0
7	80	0.3	10	1.0	120	0.3	11.0	1.0
8	80	0.3	10	1.0	120	0.5	11.0	1.0
9	80	0.3	10	1.0	120	1.0	11.0	1.0
10	120	1.1	10	1.0	180	1.5	11.0	1.0

Table 5.2: Parameters corresponding to the synthetic damped-harmonic oscillator geophone response curves given in Figure 5.4d. These curves show the differences between two response curves, where the superscript 1 refers to the numerator and 2 to the denominator. The variables are explained in Section 4.6.1.

5.3.4 Results on prestack data

The effect of the equalization procedure on prestack data is illustrated in Figures 5.5 and 5.6, which show a common shot (CS) and a common receiver (CR) gather with the CS and CR located at $x = 100$ m. For visualization purposes, we applied offset-scaling with the following function:

$$f(\mathbf{x}_o) = 1 + \eta \mathbf{x}_o \tag{5.13}$$

with $\eta = 0.10/\Delta x$, where Δx is the source spacing (10 m). Cosine tapers are applied at the edges of the computational domain for the computation of *f-k* spectra.

The traces in the CS and CR gather have identical and uniform scaling. The differences between the traces in the CR and CS gather are evident. In the raw CR gather (Figure 5.6a) the traces beyond $x = 600$ m generated by sources positioned in the dry sand (see Figure 5.1) are strongly attenuated. The corresponding reciprocal traces in the raw CS gather (Figure 5.5a) do not show such a signature of changing near-surface conditions. Another difference between the traces in the CR and CS gather is that correlated

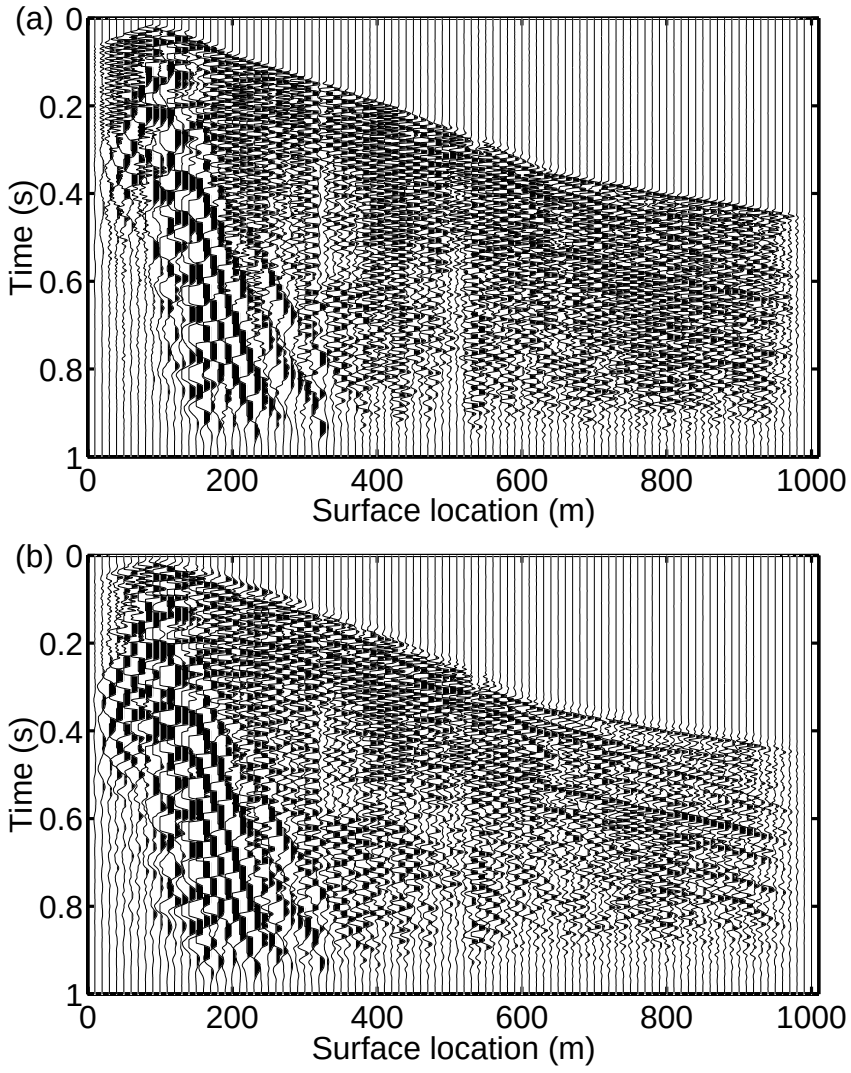

Figure 5.5: Effect of source and receiver amplitude correction on a common shot gather for a source located at position $x = 100$ m: (a) shows the input data, and (b) shows the filtered data. Both plots are scaled with respect to their maximum value (plotted with a similar relative amplitude scaling).

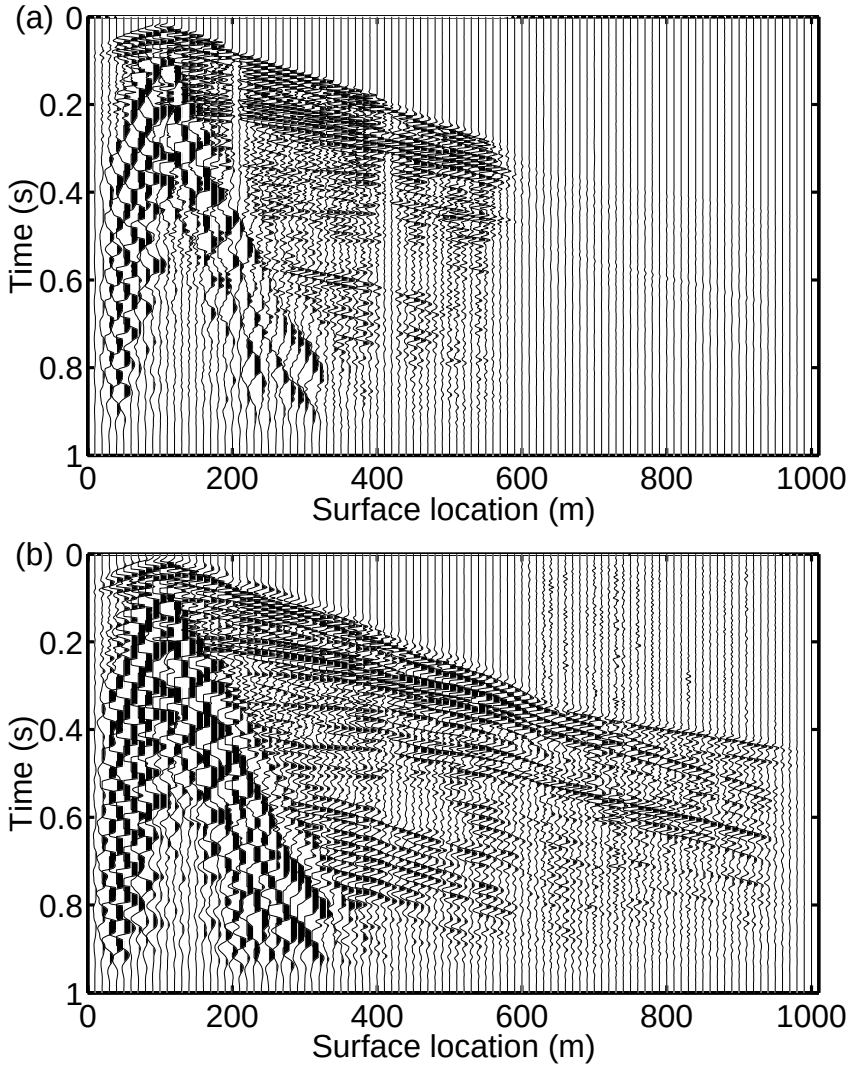

Figure 5.6: Effect of source and receiver amplitude correction on a common receiver gather for a receiver located at position $x = 100$ m: (a) shows the input data, and (b) shows the filtered data. The plots are scaled similar to the common shot gather in Figure 5.5.

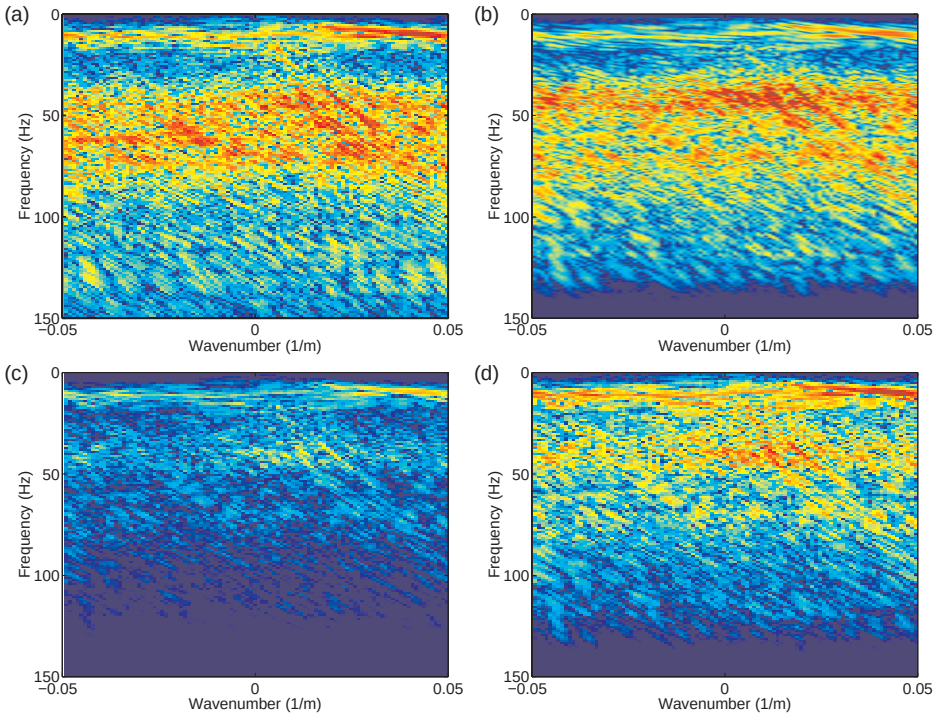

Figure 5.7: *f-k* spectra of data shown in Figure 5.5 on dB scale (common shot gather). (a) shows the input data, (b) shows the filtered data using only the receiver corrections, and (c) shows the filtered data using both source and receiver corrections. Plot (d) shows the data displayed in (c) scaled with respect to its maximum value, whereas (a), (b) and (c) have identical scaling.

events are more pronounced in the near-offset section of the CR domain.

Figures 5.5b and 5.6b show the data after the source and receiver equalization. The CR gather shows that reflectivity is measured beyond $x = 600$ m , indicating that we successfully corrected for the source attenuation effect. Furthermore, in both the corrected CR and CS gather, the correlated events are enhanced relative to the other energy. The *f-k* spectra corresponding to these data are shown in Figures 5.7 and 5.8. For the CS gather, the source equalization is only a frequency filter, whereas the receiver equalization influences the complete spectrum. To assess the consequences of both source and receiver amplitude equalization, we first applied the receiver corrections (Figure 5.7b) and consequently the source equalization. We show the final results both on similar absolute (Figure 5.7c) and relative scaling (Figure 5.7d) to the original spectrum. These spectra suggest that we have more correlated energy after the source and receiver corrections relative to other energy, and we observe that the signal bandwidth has increased in the CR domain,

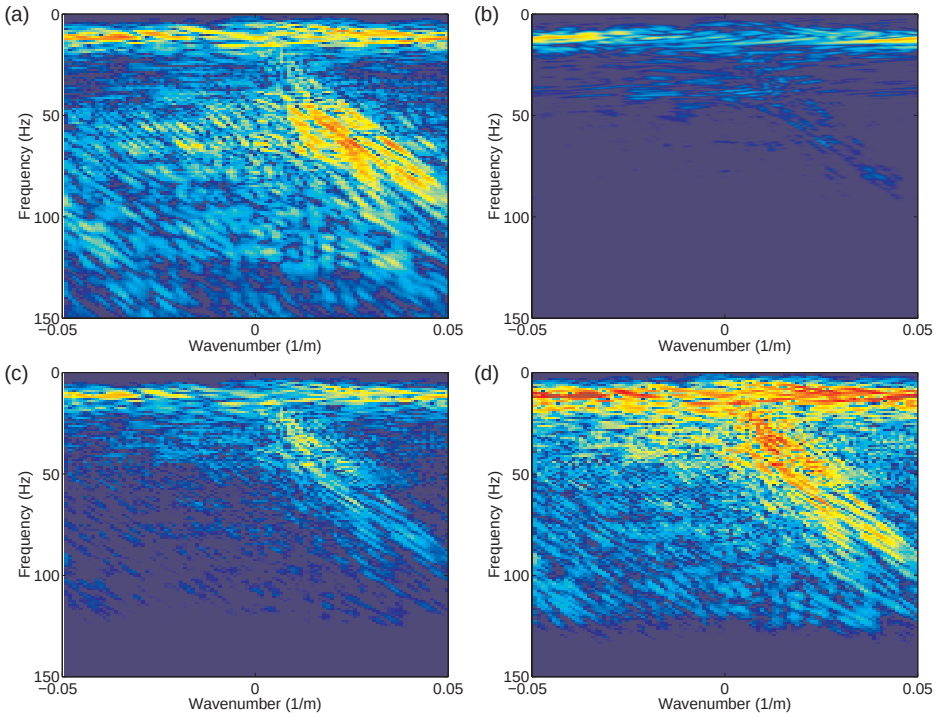

Figure 5.8: *f-k* spectra of data shown in Figure 5.6 on dB scale (common receiver gather). (a) shows the input data, (b) shows the filtered data using only the source corrections, and (c) shows the filtered data using both source and receiver corrections. Plot (d) shows the data displayed in (c) scaled with respect to its maximum value, whereas (a), (b) and (c) have identical scaling.

e.g. compare the relative signal strength below 50 Hz between Figures 5.8a and d.

We also evaluated the amplitude differences between normal and reciprocal traces before and after the equalization procedure. Therefore, we compare the amplitude of the envelope (Taner et al., 1979) of the normal and reciprocal traces in this survey and quantify the differences using the L2 norm as measure:

$$\xi = \left\{ \frac{\sum_{t=0}^{N_t \Delta t} \left[A_n(t) - A_r(t) \right]^2}{N_t} \right\}^{1/2}, \tag{5.14}$$

where $A_n(t)$ is the amplitude of the envelope of a normal trace, $A_r(t)$ denotes this for the corresponding reciprocal trace, and N_t is the number of time samples. We computed ξ for all reciprocal trace combinations in the survey, and took the average value for each offset. Killed traces are not taken into account. Figure 5.9 shows ξ as a function of offset

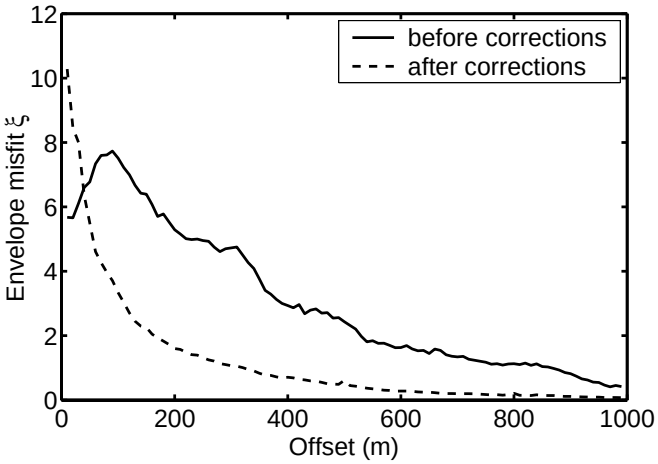

Figure 5.9: Envelope amplitude misfit as a function of offset before and after the amplitude corrections. The misfit is computed using the first 3 s of the recorded signal.

before and after the application of the equalization method. The fit between the envelope of normal and reciprocal traces has significantly improved (approximately by a factor 5), except for short offsets. Several factors contribute to the residual misfit between normal and reciprocal traces, some of which will be particularly influential at near-offsets; (i) we assumed that reciprocity is exactly valid, whereas the source radiation pattern for a shot array will differ from the receiver radiation pattern, (ii) there are mislocations between sources and receivers, since the sources are located at approximately 5 ft depth whereas the receivers are positioned at the surface, (iii) we did not apply phase corrections, (iv) and the source and receiver correction filters are approximated by finite impulse response filters.

5.3.5 Results on poststack data

We finally evaluated the consequences of the applied source and receiver equalization procedure on poststack data. The basic stacking sequence comprises the following steps: (i) trace editing, (ii) mute ground roll, air blast and refractions (performed in common receiver domain), (iii) spherical divergence correction, (iv) normal moveout correction, and finally (v) CDP stack. The poststack data are shown in Figure 5.10a, and the data which has been compensated for lateral source and receiver differences between steps (i) and (ii) are shown in Figure 5.10b. These stacks have similar scaling with respect to their maximum amplitudes. The right part of the sections is dominated by low frequency events, guided waves. A comparison between the poststack data shows that the source and receiver equalization clearly improves the signal-to-noise ratio. Subsurface structure can be more easily identified after the equalization procedure and reflectors are more

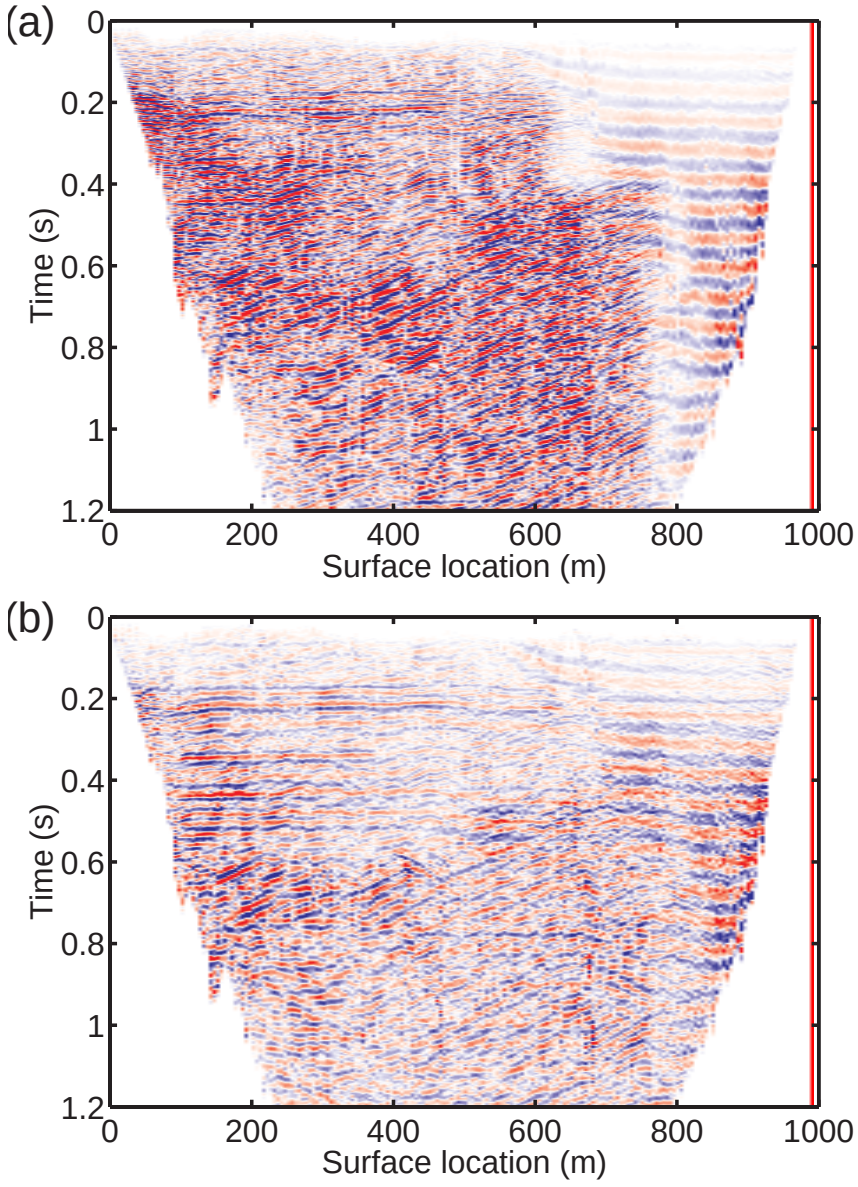

Figure 5.10: The effect of source and receiver equalization on CDP stacked data. (a) shows the uncorrected data, and (b) the corrected data.

continuous.

Thus, this example demonstrates that we can successfully compensate for lateral source and receiver perturbations, and that the application of the equalization procedure yields a substantially better image of the subsurface. It should be stressed that we did not apply any other processing to the poststack data shown in Figure 5.10.

5.4 Discussion

We illustrated the method on a relatively small data volume. For larger volumes, processing can be done in subsets, for example groups of 100 identical source and receiver positions. Two adjacent groups can be best arranged such that these have a few sources and receivers in common. Then, the differences between the relative source corrections at these positions can be used to compute a transfer function between groups. This transfer function allows scaling of the relative source correction terms of the different subsets with respect to the same absolute reference value. The relative receiver terms can be scaled in a similar fashion. As a consequence, the equalization procedure is not restricted to a small 2D acquisition geometry. Also 3D applications are possible, but this still would require identical source and receiver sampling.

For a regular recording geometry, the equalization procedure can be performed in real time in the field. This is a result of the characteristic that the coefficient matrix $\mathbf{A}$ [equation (5.6)] is independent of the recorded data, and so is its generalized inverse $\left(\mathbf{A}^T\mathbf{C}_d^{-1}\mathbf{A}+\mathbf{C}_m^{-1}\right)^{-1}\mathbf{A}^T\mathbf{C}_d^{-1}$ [equation(5.10)]. Consequently, this generalized inverse matrix can be computed prior to acquisition; the equalization procedure in the field requires then only the computation of a matrix-vector multiplication [equation (5.10)].

This is an important difference with respect to surface-consistent deconvolution methods (Taner and Koehler, 1981; Levin, 1989; Cambois and Stoffa, 1992; Cary and Lorentz, 1993). The proposed equalization procedure is essentially a preprocessing step, which can be applied in real time and to the complete seismogram, including multiples, refractions, and ground roll, whereas surface-consistent deconvolution methods can be applied to primary reflection data only. Consequently, this method is also suitable for application to multicomponent data (Van Vossen et al., 2004b) with which the conventional methods cited above often fail because it is more difficult to identify and isolate primary reflections.

Compensating multicomponent data for acquisition-related perturbations is important because these distort the characteristics of the vector-wavefield: coupling has a different effect on horizontal and vertical source and receiver components (Krohn, 1984). This can bias the observed polarization (Li and MacBeth, 1997; Michaud and Snieder, 2004). For example, determining the polarization direction of the leading split shear wave involves simultaneous rotation of the horizontal source and receiver coordinates to conform with the principal axes of an azimuthal anisotropic medium (Alford, 1986).

In principle, application of reciprocity to multicomponent recordings also requires multicomponent sources, thus $3C \times 3C$ recordings. However, the results on the field data presented above indicate that small deviations from reciprocal conditions are allowed. In the field experiment, a pattern of explosive sources was used, and we considered the

vertical component of the recorded wavefield. Therefore, it is worthwhile to investigate if we can also compensate multicomponent recordings generated by a single component source.

Application to multicomponent data is especially interesting, because the quality of shear data recorded on the horizontal components is often more severely affected by receiver coupling effects than vertical component data Krohn (1984); Garotta (2000). Since the equalization procedure for source and receiver amplitude responses resulted in a significant improvement of the vertical component data, which is most evident on the poststack data (Figure 5.10), we expect that this method will also greatly improve the quality of horizontal component data.

In this paper, we only investigated amplitude corrections, and demonstrated that these corrections can significantly improve the data quality. However, Figures 5.5 and 5.6 show that reflection curves between $t = 0.6$ and 0.8 s can be easily identified in the CR gather, whereas they are difficult to observe in the CS gather, even after the amplitude corrections. This indicates that receiver coupling variations also influence the phase of the recordings, and that these significantly vary between adjacent receivers. At the source side, phase perturbations vary less rapidly along the spread, similar to the amplitude perturbations. This results in better aligned reflections in the CR domain. We did not correct for phase changes because non-uniqueness problems related to cycle skips in phase decomposition have yet to be resolved.

5.5 Concluding remarks

We successfully applied a preprocessing technique based on reciprocity to compensate for source and receiver perturbations on field data acquired in Manistee County, Michigan. Both prestack and poststack data show a significant improvement in the signal-to-noise ratio after the source and receiver equalization procedure. The poststack data shows that subsurface structures can be observed after the equalization procedure, whereas they cannot be identified without compensating for the source and receiver amplitude perturbations. Thus, application of this method will greatly improve the prospects of land seismic data.

The obtained source corrections are sensitive to changes in near-surface conditions, especially to the water saturation level, whereas a correlation between near-surface conditions and receiver perturbations has not been observed. The receiver corrections vary rapidly along the spread. This indicates that both source and receiver perturbations have to be taken into account to properly compensate for acquisition effects.

The observed receiver response variation with frequency did not conform to the generally accepted damped harmonic oscillator model. For frequencies below 100 Hz, the retrieved corrections are much larger than predicted by this model. In addition, ratios between theoretical damped-harmonic oscillator curves have one bounded minimum and maximum value, whereas we obtained ratios with two distinct minima or maxima.

A fundamental difference with surface-consistent deconvolution methods is that those methods are applicable to primary reflection data only, requiring suppression of ground

roll and multiples prior to the application. However, the performance of multichannel filter operations which are commonly used for the suppression of ground roll and multiples themselves deteriorates in the presence of amplitude and phase perturbations. Therefore, these corrections should be applied in the early stages of the processing, preferably to single sensor data prior to group forming.

The equalization procedure discussed in this paper satisfies these criteria since it is essentially a preprocessing technique, and can be applied directly to the recorded data: it is applicable to the whole seismic trace. Furthermore, it does not make additional assumptions about the subsurface structure. The procedure is based on reciprocity, and therefore requires symmetric wavefield sampling. In case of non-identical source and receiver positions, interpolation is required prior to application.

Chapter 6

Summary and outlook

6.1 Summary

Seismic reflection methods are widely used for the detection of hydrocarbons in subsurface structures up to several kilometers depth. However, since most data are acquired at or close to the Earth's surface, it is essential to understand the influence of the near-surface on the acquired data in order that its effects are not interpreted as pertaining to the reservoir. The near-surface effect on seismic data has two main origins: (i) near-surface wave propagation and (ii) wavefield acquisition. Wavefield acquisition comprises both wavefield excitation and wavefield measurement, i.e. source and receiver effects.

Since both P- and S-wave velocities are observed to vary rapidly close to the Earth's surface, wave propagation in the near-surface is often very complex. In order to improve our understanding of near-surface wave propagation, we investigated and developed methods to determine near-surface P- and S-wave velocities (these are used in some data processing algorithms). For this purpose, we used dense recording geometries including buried geophones, since these material properties cannot be resolved with a conventional acquisition geometry using geophones only at the free surface. We investigated methods based on direct inversion of the wave equation, which are applicable to the whole seismic trace. These methods require that spatial and temporal wavefield derivatives can be obtained from the acquired data. The problem associated with these methods is that the spatial derivatives cannot be obtained with sufficient accuracy in the presence of measurement errors.

Alternatively, in the plane wave assumption, the spatial wavefield derivatives do not have to be determined explicitly from the acquired data. This leads to the Haskell-Thompson propagator formalism, which describes vertical plane wave propagation in a horizontally layered medium. Using symmetry properties of the elastic propagator matrix, we obtain several components of the propagator matrix directly from the recorded data. We developed a procedure to invert these components of the propagator matrix for near-surface P- and S-wave velocities. We refer to this procedure as *propagator inversion*.

Synthetic tests demonstrated that this method is robust in the presence of measurement errors. In addition, the plane wave assumption is not strictly required - it can be relaxed if data are acquired with multiple sources in a configuration which allows the estimation of the propagator matrix in the frequency-wavenumber domain, i.e. for a superposition of plane waves.

The propagator inversion was applied to a field data set which we acquired in Zeist, The Netherlands. We obtained a low near-surface P velocity, namely 270 ± 15 m/s, which is well below the sound velocity in air, and 150 ± 9 m/s for the S velocity. The buried geophone was located at approximately 1.0 m depth, thus the obtained velocities are only representative of the top meter of the near-surface. A higher P velocity was obtained (approximately 450 m/s) with dispersion analysis for guided waves. This estimate represents the average velocity for the near-surface layer located above the groundwater table, which was located at approximately 8.0 m depth. This indicates that velocities increase quite rapidly with depth in the near-surface low-velocity layer, presumably due to compaction. We suspect that this is the reason that subsonic P-wave velocities are not commonly observed. Hence, we infer that they should be used more frequently in future in data processing algorithms that require estimates of velocities at the surface [e.g. wavefield separation and polarization analysis (Dankbaar, 1985; Wapenaar et al., 1990; Robertsson and Curtis, 2002)].

The second part of this thesis is devoted to the influence of wavefield acquisition. Corrections for source and receiver perturbations are necessary when their behaviour changes within a given survey. Since these perturbations affect all multichannel filter operations, which are commonly used for ground roll and multiple suppression, corrections should be performed in the early stages of processing. However, existing techniques, such as surface-consistent deconvolution, are applicable to primary reflection data only, and thus require prior processing before even they can be applied.

We developed an alternative approach to compensate for source and receiver amplitude perturbations which has the advantage of being purely a preprocessing step. It is applicable to the whole seismic trace, and does not impose additional assumptions on the subsurface. The approach is based on reciprocity of the medium response. This implies that differences between normal and reciprocal traces can be attributed to the source and receiver perturbations. We successfully demonstrated the procedure to compensate for these perturbations on both synthetic and field data. The field data were acquired in Manistee County, Michigan (courtesy of WesternGeco). Along the acquisition line, near-surface conditions change from moist-to-wet sediments to dry sands. The obtained source corrections are strongly correlated to these changing near-surface conditions, whereas the receiver corrections vary more strongly from geophone to geophone. Compensation of the recorded data for the source and receiver perturbations resulted in a significant improvement of the signal-to-noise ratio, both on prestack and poststack data. Finally, the receiver response we found did not agree with the generally accepted damped harmonic oscillator model, implying that this model need to be revised.

6.2 Outlook

Source and receiver perturbations are widely considered to be a major problem in land seismic data. It is one of the reasons that marine data are generally of better quality than land seismic data, since uniform acoustic properties of the seawater provide consistent coupling for the marine sources and receivers (Aritman, 2001). For land seismic data, near-surface material properties are observed to vary rapidly, and corrections are required for source and receiver perturbations before a reliable image of the subsurface can be obtained. In this thesis, a raw data preprocessing method is developed to compensate land seismic data for these source and receiver perturbations. We expect that this will substantially improve the results of processing and interpreting land seismic data in various ways.

Our understanding of the complexities of near-surface wave propagation will improve, since we are able to distinguish these effects from acquisition-related effects. We have seen that rapid variations in the recordings can be a result of the acquisition. However, experiments with geophones at shallow depth indicated that rapid changes in the wavefield with depth are due to effects of plane wave propagation, rather than due to measurement errors. These changes are a result of interfering waves in the near-surface low velocity layer. Rapid changes in wave velocities were observed close to the free surface, i.e. P- and S-wave velocities are lower than the sound speed in air. We have to be aware of the existence of these low velocities close to the free surface when analyzing the partitioning of the wavefield at the free surface.

Since seismic surveys usually aim to resolve deeper structures, effects of near-surface wave propagation have to be removed in the data. Processing aims to isolate primary reflections in the data, and therefore ground roll and multiples have to be suppressed. In the field, source and receiver arrays are commonly used to suppress ground roll. However, the performance of these types of multichannel filters degrades in the presence of source and receiver perturbations. Therefore, we recommend to acquire recordings of individual sources and receivers in the field. Single sensor recordings and digital group forming was originally suggested by Ongkiehong and Askin (1988) in order to maintain flexibility during the processing stages. In principle, these individual recordings can be compensated for source and receiver perturbations prior to digital group forming. Therefore, we expect that ground roll and multiples can be suppressed more effectively.

Interpretation is also influenced by source and receiver perturbations, since these influence primary reflection data directly. Especially amplitude information, which is used to determine rock properties such as permeability and porosity of reservoir rock, can be corrupted. This could create false AVO trends, and could potentially lead to misinterpretations. As a result, the interpretation could greatly benefit from the corrections for source and receiver perturbations.

Although we have only given examples of single component data in this thesis, the equalization procedure is also applicable to multicomponent data. As a result, this technique can improve the vector fidelity of recorded multicomponent data: in addition to the previously cited applications, compensating multicomponent data for source and receiver perturbations is necessary for estimating earth properties which are based on polarization,

such as information on the direction of fractures (Winterstein and Meadows, 1991). In order to retrieve the polarization, the directivity of the source and receiver has to be taken into account (Brummit, 1989).

The developed equalization procedure requires data acquisition in a geometry which allows the usage of apparently redundant recordings of reciprocal traces. This redundancy enables us to use reciprocity to identify source and receiver perturbations, and to appropriately compensate for these effects. This procedure significantly improves the data quality of land seismic data, and our expectation is that this enables better processing of the data. This results in better images of the subsurface structures, and more reliable amplitude information to determine reservoir rock properties.

Finally, the retrieved receiver responses did not agree with the generally accepted damped harmonic oscillator model (Hoover and O'Brien, 1980; Krohn, 1984) which describes the geophone-ground coupling. This implies that instead of indicating the frequency response of geophone-ground coupling with a resonant frequency and a corresponding damping factor, an alternative description may be necessary.

Bibliography

Aki, K. and Richards, P. G. (2002). *Quantitative Seismology, 2nd. Ed.* University Science Books.

Alford, R. M. (1986). Shear data in the presence of azimuthal anisotropy: Dilley, Texas. *56th Annual International Meeting, SEG, Expanded Abstracts*, pages 476–479.

Ammon, C. J. (1991). The isolation of receiver effects from teleseismic P waveforms. *Bulletin of the Seismological Society of America*, 81:2504–2510.

Aritman, B. C. (2001). Repeatability study of seismic source signatures. *Geophysics*, 66:1811–1817.

Bachrach, R., Dvorkin, J., and Nur, A. M. (1998). High-resolution shallow-seismic experiments in sand, Part II: Velocities in shallow unconsolidated sand. *Geophysics*, 63:1234–1240.

Bachrach, R., Dvorkin, J., and Nur, A. M. (2000). Seismic velocities and Poisson's ratio of shallow unconsolidated sands. *Geophysics*, 65:559–564.

Bachrach, R. and Nur, A. M. (1998). High-resolution shallow-seismic experiments in sand, Part I: Water table, fluid flow, and saturation. *Geophysics*, 63:1225–1233.

Baker, G. S., Steeples, D. W., and Schmeissner, C. (1999). In-situ, high-resolution P-wave velocity measurements within 1 m of the earth's surface. *Geophysics*, 64:323–325.

Berni, A. J. and Roever, W. L. (1989). Field array performance: Theoretical study of spatially correlated variations in amplitude coupling and static shift and case study in the Paris Basin. *Geophysics*, 54:451–459.

Birkelo, B. A., Steeples, D. W., Miller, R. D., and Sophocleous, M. (1987). Seismic reflection study of a shallow aquifer during a pumping test. *Ground Water*, 25:703–709.

Blacquière, G. and Ongkiehong, L. (2000). Single sensor recording: anti-alias filtering, perturbations and dynamic range. *70th Annual International Meeting, SEG, Expanded Abstracts*, pages 33–36.

Bourbié, T., Coussy, O., and Zinszner, B. (1987). *Acoustics of porous media*. Technip.

Brekhovskikh, L. M. (1980). *Waves in layered media*. Academic Press.

Brummit, J. G. (1989). Source directivity and its effect on resolution and signature deconvolution. *First Break*, 7:17–24.

Cambois, G. and Stoffa, P. L. (1992). Surface-consistent deconvolution in the log/Fourier domain. *Geophysics*, 57:823–840.

Cary, P. W. and Lorentz, G. A. (1993). Four-component surface-consistent deconvolution. *Geophysics*, 58:383–392.

Castagna, J. P. and Backus, M. M. (1993). *Offset-dependent reflectivity – Theory and practice of AVO analysis*. Society of Exploration Geophysicists.

Cox, M. (1999). *Static corrections for seismic reflection surveys*. Society of Exploration Geophysicists.

Curtis, A. and Robertsson, J. O. A. (2002). Volumetric wavefield recording and wave equation inversion for near-surface material properties. *Geophysics*, 67:1602–1611.

Dankbaar, J. W. M. (1985). Separation of P- and S- waves. *Geophysical Prospecting*, 33:970–986.

de Hoop, A. T. and Van der Hijden, J. H. M. T. (1983). Generation of acoustic waves by an impulsive line source in a fluid/solid configuration with a plane boundary. *Journal of the Acoustical Society of America*, 74:333–342.

Deal, M. M. and Nolet, G. (1996). Nullspace shuttles. *Geophysical Journal International*, 124:372–380.

Doornenbal, J. C. and Helbig, K. (1983). High-resolution seismics on a tidal flat in the Dutch

Delta – acquisition, processing and interpretation. *First Break*, 1:9–20.

Drijkoningen, G. G. (2000). On the usefulness of ground-coupling experiments to seismic data. *Geophysics*, 65:1780–1787.

Fenati, D. and Rocca, F. (1984). Seismic reciprocity field tests from the Italian Peninsula. *Geophysics*, 49:1690–1700.

Gao, L., Parker, K. J., Lerner, R. M., and Levinson, S. F. (1996). Imaging of the elastic properties of tissue — A review. *Ultrasound in Medicine & Biology*, 22:959–977.

Garotta, R. (2000). *Shear waves from acquisition to interpretation*. Society of Exploration Geophysicists.

Gilbert, F. and Backus, G. E. (1965). Propagator matrices in elastic wave and vibration problems. *Geophysics*, 31:326–332.

Goforth, T. and Hayward, C. (1992). Seismic reflection investigations of a bedrock surface buried under alluvium. *Geophysics*, 57:1217–1227.

Goupillaud, P. L. (1961). An approach to inverse filtering of near-surface layer effects from seismic records. *Geophysics*, 26:754–760.

Haskell, N. (1953). The dispersion of surface waves in multilayered media. *Bulletin of the Seismological Society of America*, 43:17–34.

Helmberger, D. and Wiggins, R. A. (1971). Upper mantle structure of Midwestern United States. *Journal of Geophysical Research*, 76:3229–3245.

Hoover, G. M. and O'Brien, J. T. (1980). The influence of the planted geophone on seismic land data. *Geophysics*, 45:1239–1253.

Hunter, J. A., Pullan, S. E., Burns, R. A., Gagne, R. M., and Good, R. L. (1984). Shallow seismic reflection mapping of the overburden bedrock interface with the engineering seismograph – Some simple techniques. *Geophysics*, 49:1381–1385.

Kähler, S. and Meissner, R. (1983). Radiation and receiver pattern of shear and compressional waves as a function of poisson ratio. *Geophysical Prospecting*, 31:421–435.

Karrenbach, M. (1994). Multicomponent source equalization. *64th Annual International Meeting,SEG, Expanded Abstracts*, pages 1449–1452.

Kelamis, P. G. and Verschuur, D. J. (2000). Surface-related multiple elimination on land seismic data – Strategies via case studies. *Geophysics*, 65:719–734.

Kennett, B. L. N. (1983). *Seismic wave propagation in stratified media*. Cambridge University Press.

Knopoff, L. and Gangi, A. F. (1959). Seismic reciprocity. *Geophysics*, 24:681–691.

Krohn, C. E. (1984). Geophone ground coupling. *Geophysics*, 49:722–731.

Lanczos, C. (1961). *Linear Differential Operators*. Van Nostrand.

Langston, C. A. (1979). Structure under Mount Rainier, Washington, inferred from teleseismic body waves. *Journal of Geophysical Research*, 84:4749–4762.

Levander, A. R. (1988). Fourth-order finite-difference P-SV seismograms. *Geophysics*, 53:1425–1435.

Levin, S. A. (1989). Surface-consistent deconvolution. *Geophysics*, 54:1123–1133.

Li, X. and MacBeth, C. (1997). Data-matrix asymmetry and polarization changes from multicomponent surface seismics. *Geophysics*, 62:630–643.

Luo, H. and Li, Y. (1998). The application of blind channel identification techniques to prestack seismic deconvolution. *Proceedings of the IEEE*, 86:2082–2089.

Menke, W. (1984). *Geophysical data analysis: discrete inverse theory*. Academic Press.

Michaels, P. (2002). Identification of subsonic P-waves. *Geophysics*, 67:909–920.

Michaud, G. and Snieder, R. (2004). Error in shear-wave polarization and time splitting. *Geophysical Prospecting*, 52:123–132.

Mindlin, R. D. (1949). Compliance of elastic bodies in contact. *Journal of Applied Mechanics*, 16:259–268.

Muijs, R., Holliger, K., and Robertsson, J. O. A. (2002). Perturbation analysis of an explicit wavefield separation scheme for P- and S-waves. *Geophysics*, 67:1972–1982.

Muthupillai, R., Lomas, D. J., Rossman, P. J., Greenleaf, J. F., Manduca, A., and Ehman, R. L. (1995). Magnetic resonance elastography by direct visualization of propagating acoustic strain waves. *Science*, 269:1854–1857.

Newman, P. and Mahoney, J. T. (1973). Patterns – With a pinch of salt. *Geophysical Prospecting*, 21:197–219.

Oliphant, T., Mahowald, J. L., Ehman, R. L., and Greenleaf, J. F. (1999). Complex–valued quantitative stiffness estimation using dynamic displacement measurements and local inversion of conservation of momentum. *IEEE Ultrasonics Symposium*, pages 1641–1644.

Oliphant, T. E., Manduca, A., Ehman, R. L., and Greenleaf, J. F. (2001). Complex-valued stiffness reconstruction for magnetic resonance elastography by algebraic inversion of the differential equation. *Magnetic Resonance in Medicine*, 45:299–310.

Ongkiehong, L. (1988). A changing philosophy in seismic data acquisition. *First Break*, 6(9):281–285.

Ongkiehong, L. and Askin, H. J. (1988). Towards the universal seismic acquisition technique. *First Break*, 6(2):46–63.

Osen, A., Amundsen, L., and Reitan, A. (1999). Removal of water-layer multiples from multicomponent sea-bottom data. *Geophysics*, 64:838–851.

Ostrander, W. J. (1984). Plane-wave reflection coefficients for gas sands at nonnormal angles of incidence. *Geophysics*, 49:1637–1648.

Park, C. B., Miller, R. D., and Xia, J. (1998). Imaging dispersion curves of surface waves on multichannel record. *68th Annual International Meeting, SEG, Expanded Abstracts*, pages 1377–1380.

Robertsson, J. O. A., Blanch, J. O., and Symes, W. W. (1994). Viscoelastic finite-difference modeling. *Geophysics*, 59:1444–1456.

Robertsson, J. O. A. and Curtis, A. (2002). Wavefield separation using densely deployed three–component single–sensor groups in land surface–seismic recordings. *Geophysics*, 67:1624–1633.

Robertsson, J. O. A., Holliger, K., Green, A. G., Pugin, A., and Iaco, R. D. (1996). Effects on near-surface waveguides on shallow high-resolution seismic refraction and relection data. *Geophysical Research Letters*, 23:495–498.

Robertsson, J. O. A. and Muyzert, E. (1999). Wavefield separation using a volume distribution of three component recordings. *Geophysical Research Letters*, 26:2821–2824.

Romano, A. J., Bucaro, J. A., Ehman, R. L., and Shirron, J. J. (2000). Evaluation of a material parameter extraction algorithm using MRI-based displacement measurements. *IEEE Transactions on Ultrasonics, Ferroelectrics, and Frequency Control*, 47:1575–1581.

Romano, A. J., Shirron, J. J., and Bucaro, J. A. (1998). On the noninvasive determination of material parameters from a knowledge of elastic displacements: theory and numerical simulation. *IEEE Transactions on Ultrasonics, Ferroelectrics, and Frequency Control*, 45:751–759.

Sallas, J. J. (1984). Seismic vibrator control and the downgoing P-wave. *Geophysics*, 49:732–740.

Steeples, D. W. and Miller, R. D. (1990). Seismic reflection methods applied to engineering, environmental and groundwater problems. In Ward, S. H., editor, *Geotechnical and environmental geophysics I*, pages 1–30. Society of Exploration Geophysicists.

Stümpel, H., Kähler, S., Meissner, R., and Milkereit, B. (1984). The use of seismic shear waves and compressional waves for lithological problems of shallow sediments. *Geophysical Prospecting*, 32:662–675.

Taner, M., Koehler, F., and Sheriff, R. (1979). Complex seismic trace analysis. *Geophysics*, 44:1041–1063.

Taner, M. T. and Koehler, F. (1981). Surface consistent corrections. *Geophysics*, 46:17–22.

Tarantola, A. (1987). *Inverse problem theory*. Elsevier.

Tatham, R. H. and McCormack, M. D. (1991).

Multicomponent seismology in petroleum exploration. Society of Exploration Geophysicists.

Thomson, W. T. (1950). Transmission of elastic waves through a stratified solid medium. *Journal of Applied Physics*, 21:89–93.

Toksöz, M. N., Cheng, C. H., and Timur, A. (1976). Velocities of seismic waves in porous rocks. *Geophysics*, 41:621–645.

Trampert, J., Cara, M., and Frogneux, M. (1993). SH propagator matrix and Q_s estimates from borehole- and surface- recorded earthquake data. *Geophysical Journal International*, 112:290–299.

Unser, M. (1999). Splines, a perfect fit for signal and image processing. *IEEE Signal Processing Magazine*, 16(6):22–38.

Van den Berg, J., Curtis, A., and Trampert, J. (2003). Optimal nonlinear Bayesian experimental design: an application to amplitude versus offset experiments. *Geophysical Journal International*, 155:411–421.

Van Houten, E. E. W., Paulsen, K. D., Miga, M. I., Kennedy, F. E., and Weaver, J. B. (1999). An overlapping subzone technique for MR-based elastic property reconstruction. *Magnetic Resonance in Medicine*, 42:779–786.

Van Vossen, R., Curtis, A., Laake, A., and Trampert, J. (2005). Equalization of source and receiver amplitude responses using reciprocity and waveform inversion – Application to land seismic data. *Submitted to Geophysics*.

Van Vossen, R., Curtis, A., and Trampert, J. (2004a). Subsonic near-surface P-velocity and low S-velocity observations using propagator inversion. *Geophysics*, in press.

Van Vossen, R., Curtis, A., and Trampert, J. (2004b). Surface-consistent amplitude corrections for single- or multi-component sources and receivers using reciprocity and waveform inversion. *Submitted to Geophysical Journal International*.

Van Vossen, R., Trampert, J., and Curtis, A. (2004c). Propagator and wave-equation inversion for near-receiver material properties. *Geophysical Journal International*, 157:796–812.

Vermeer, G. (1991). Symmetric sampling. *The Leading Edge*, 10(11):21–27.

Verschuur, D. J., Berkhout, A. J., and Wapenaar, C. P. A. (1992). Adaptive surface-related multiple elimination. *Geophysics*, 57:1166–1177.

Wang, Z. and Nur, A. (1992). *Seismic and acoustic velocities in reservoir rocks, Vol. 2, Theoretical and model studies*. Society of Exploration Geophysicists.

Wapenaar, C. P. A., Herrmann, P., Verschuur, D. J., and Berkhout, A. J. (1990). Decomposition of multicomponent seismic data into primary P- and S-wave responses. *Geophysical Prospecting*, 38:633–661.

Ward, S. H. (1990). *Geotechnical and environmental geophysics, Vol. I–III*. Society of Exploration Geophysicists.

White, J. E. (1960). Use of reciprocity theorem for computation of low frequency radiation patterns. *Geophysics*, 25:613–624.

White, J. E. and Sengbush, R. L. (1953). Velocity measurements in near-surface formations. *Geophysics*, 18:54–69.

Wiggins, R. A., Larner, K. L., and Wisecup, R. D. (1976). Residual static analysis as a general linear inverse problem. *Geophysics*, 41:922–938.

Winterstein, D. F. and Meadows, M. A. (1991). Shear-wave polarizations and subsurface stress directions at Lost Hills field. *Geophysics*, 56:1331,1348.

Yilmaz, O. (2001). *Seismic data analysis I – Processing, inversion and interpretation of seismic data*. Society of Exploration Geophysicists.

Yu, G. (1985). Offset-amplitude variation and controlled-amplitude processing. *Geophysics*, 50:2697–2708.

Zeng, X. and MacBeth, C. (1993). Algebraic processing techniques for estimating shear-wave splitting in near-offset VSP data: Theory. *Geophysical Prospecting*, 41:1033–1066.

Appendix A

Coefficients for direct wave-equation inversion and integral equation formulation

A.1 Coefficients for direct wave-equation inversion

The measurable coefficients in equations (2.6)–(2.8) for direct wave-equation inversion are found by inserting the free-surface derivative conditions, equations (2.3)–(2.5), into the wave equation (2.1):

$$A_1(t) = \frac{2}{\Delta z}\left(\partial_1 v_3 + \partial_3 v_1\right) + \nabla_H^2 v_1 + 2\partial_1\left(\nabla_H \cdot \mathbf{v}_H\right), \tag{A.1}$$

$$A_2(t) = \frac{2}{\Delta z}\left(\partial_2 v_3 + \partial_3 v_2\right) + \nabla_H^2 v_2 + 2\partial_2\left(\nabla_H \cdot \mathbf{v}_H\right), \tag{A.2}$$

$$A_3(t) = \frac{2}{\Delta z}\left(\nabla_H \cdot \mathbf{v}_H + \partial_3 v_3\right) - \nabla_H^2 v_3, \tag{A.3}$$

$$B_1(t) = 2\partial_1\left(\nabla_H \cdot \mathbf{v}_H\right), \tag{A.4}$$

$$B_2(t) = 2\partial_2\left(\nabla_H \cdot \mathbf{v}_H\right), \tag{A.5}$$

and

$$B_3(t) = \frac{4}{\Delta z}\left(\nabla_H \cdot \mathbf{v}_H\right) - 2\left(\nabla_H^2 v_3\right). \tag{A.6}$$

The finite-difference (FD) first-order derivatives in depth are denoted $\partial_3 \mathbf{v}$ and are given by:

$$\partial_3 \mathbf{v}(\Delta z/2) = \frac{\mathbf{v}(\Delta z) - \mathbf{v}(0)}{\Delta z} + O(\Delta z^2), \tag{A.7}$$

with Δz the depth beneath the free surface of the buried geophone. The vertical derivative cannot be measured exactly at the free surface but at depth $\Delta z/2$. The following notation is used for horizontal wavefield derivatives:

$$\nabla_H \quad = \quad [\partial_1 \; \partial_2]^T \,, \tag{A.8}$$

and

$$\mathbf{v}_H \quad = \quad [v_1 \; v_2]^T \,. \tag{A.9}$$

Temporal and spatial wavefield derivatives are computed using finite-difference operators.

A.2 Integral equation formulation

We demonstrate that the wave equation (2.1) can be transformed into an integral equation. Let $\mathbf{w} = (w_1, w_2, w_3)^T$ be a sufficient smooth vector-valued function and Ω a volume bounded by a surface Γ. If the wave equation is multiplied by $\mathbf{w}$ and integrated over the volume Ω, the result is:

$$\int_\Omega \mathbf{w} \cdot \ddot{\mathbf{v}} \, \mathrm{d}\Omega = \int_\Omega \mathbf{w} \cdot \left[\alpha^2 \nabla (\nabla \cdot \mathbf{v}) - \beta^2 \nabla \times (\nabla \times \mathbf{v}) \right] \mathrm{d}\Omega. \tag{A.10}$$

The first term of the right-hand side of equation (A.10) can be expanded by repeated application of the divergence theorem:

$$\begin{aligned} &\int_\Omega \mathrm{d}\Omega \, \mathbf{w} \cdot [\nabla (\nabla \cdot \mathbf{v})] && \text{(A.11)} \\ &= \int_\Gamma \mathrm{d}\Gamma \; [\mathbf{w} (\nabla \cdot \mathbf{v})] \cdot \mathbf{n} - \int_\Omega \mathrm{d}\Omega \; (\nabla \cdot \mathbf{w}) (\nabla \cdot \mathbf{v}) \\ &= \int_\Gamma \mathrm{d}\Gamma \; [\mathbf{w} (\nabla \cdot \mathbf{v}) - \mathbf{v} (\nabla \cdot \mathbf{w})] \cdot \mathbf{n} + \int_\Omega \mathrm{d}\Omega \, \mathbf{v} \cdot [\nabla (\nabla \cdot \mathbf{w})] \,, && \text{(A.12)} \end{aligned}$$

where $\mathbf{n}$ is the outward pointing normal vector on Γ. The second term is expanded using the identity

$$\nabla \times (\nabla \times \mathbf{v}) = \nabla (\nabla \cdot \mathbf{v}) - \nabla^2 \mathbf{v} \tag{A.13}$$

and the divergence theorem:

$$\begin{aligned} &\int_\Omega \mathrm{d}\Omega \, \mathbf{w} \cdot [\nabla \times (\nabla \times \mathbf{v})] = \int_\Omega \mathrm{d}\Omega \, \mathbf{v} \cdot [\nabla \times (\nabla \times \mathbf{w})] \, \mathrm{d}\Omega \\ &+ \int_\Gamma \mathrm{d}\Gamma \; \left[\mathbf{w} (\nabla \cdot \mathbf{v}) - \mathbf{v} (\nabla \cdot \mathbf{w}) - \mathbf{w} \cdot (\nabla \mathbf{v})^T + \mathbf{v} \cdot (\nabla \mathbf{w})^T \right] \cdot \mathbf{n}. && \text{(A.14)} \end{aligned}$$

In the volume integrals, all spatial wavefield derivatives have disappeared in equation (A.14). Because the vector-valued functions $\mathbf{w}$ can be chosen arbitrarily, boundary conditions can be imposed such that the surface integrals vanish. Consequently, all spatial wavefield derivatives can be made to disappear.

Appendix B

Propagator estimation using Wiener deconvolution

In this section, we demonstrate the procedure to obtain the propagator filters, which are either symmetric or antisymmetric about $t = 0$, using Wiener deconvolution. We closely follow Yilmaz (2001) in our derivation, with the exception that we estimate acausal filters with symmetry conditions around $t = 0$.

Suppose that $f(t)$ and $g(t)$ are continuous signals, and that $h(t)$ is given by the deconvolution of $f(t)$ by $g(t)$:

$$h(t) = f(t) * g^{-1}(t), \tag{B.1}$$

with $g^{-1}(t)$ defined such that $g^{-1}(t) * g(t) = \delta(t)$, and the asterisk $(*)$ is the convolution operator. Thus,

$$g(t) * h(t) = f(t), \tag{B.2}$$

where the function $h(t)$ represents here the unknown propagator. Cross-correlating equation (B.2) with $g(t)$ gives:

$$R(t) * h(t) = q(t), \tag{B.3}$$

where $R(t)$ denotes the autocorrelation of $g(t)$ and

$$q(t) = \int_{-\infty}^{\infty} f(t+\tau)g(\tau)\mathrm{d}\tau. \tag{B.4}$$

Assume that we may approximate the propagator $h(t)$ by a filter with $2M+1$ independent coefficients. This reads, denoting the time series with a vector:

$$\mathbf{h} \;=\; [h_{-M}\; h_{-M+1}\; \ldots h_{-1}\; h_0\; h_1\; \ldots h_{M-1}\; h_M]^T, \tag{B.5}$$

where ^{T} is the transpose operator. For a correlation with a maximum correlation length of $N+1$, $\mathbf{q}$ has $2N+1$ coefficients, and reads

$$\mathbf{q} = [q_{-N}\ q_{-N+1} \cdots q_{-1}\ q_0\ q_1\ \cdots q_{N-1}\ q_N]^T . \tag{B.6}$$

Then, we may recast equation (B.3) in a discrete form:

$$\mathbf{R}\mathbf{h} = \mathbf{q}. \tag{B.7}$$

The coefficients of the $(2N+1) \times (2M+1)$ autocorrelation matrix $\mathbf{R}$ are given by:

$$R_{ij} = r_{|i-j|}, \tag{B.8}$$

where r_k denotes the k^{th} lag of the autocorrelation of $\mathbf{g}$, and $N+1$ is the maximum correlation length.

In order to take the symmetry conditions into account, we partition $\mathbf{q}$, $\mathbf{h}$, and $\mathbf{R}$:

$$\mathbf{h} = \begin{pmatrix} \mathbf{h}^- \\ \mathbf{h}^+ \end{pmatrix}, \qquad \mathbf{q} = \begin{pmatrix} \mathbf{q}^- \\ \mathbf{q}^+ \end{pmatrix}, \tag{B.9}$$

and

$$\mathbf{R} = \begin{pmatrix} \mathbf{R}^{-,-} & \mathbf{R}^{-,+} \\ \mathbf{R}^{+,-} & \mathbf{R}^{+,+} \end{pmatrix}. \tag{B.10}$$

The partitioned vectors are given by:

$$\mathbf{h}^- = [h_0/2\ h_{-1}\ h_{-2} \ldots h_{-M}]^T , \tag{B.11}$$

$$\mathbf{h}^+ = [h_0/2\ h_1\ h_2\ \ldots h_M]^T , \tag{B.12}$$

$$\mathbf{q}^- = [q_0\ q_{-1}\ q_{-2} \cdots q_{-N}]^T , \tag{B.13}$$

$$\mathbf{q}^+ = [q_0\ q_1\ q_2 \ldots q_N]^T , \tag{B.14}$$

and the submatrices of $\mathbf{R}$ read:

$$\mathbf{R}^{+,+} = \mathbf{R}^{-,-} = \begin{pmatrix} r_0 & r_1 & r_2 & \cdots & & r_M \\ r_1 & r_0 & r_1 & \ddots & & r_{M-1} \\ r_2 & r_1 & r_0 & \ddots & & r_{M-2} \\ \vdots & \ddots & \ddots & \ddots & & \\ & & & & r_1 & \\ r_N & & & & r_1 & r_0 \end{pmatrix} \tag{B.15}$$

and

$$\mathbf{R}^{-,+} = \mathbf{R}^{+,-} = \begin{pmatrix} r_0 & r_1 & r_2 & \cdots & & r_M \\ r_1 & r_2 & r_3 & \ddots & & r_{M+1} \\ r_2 & r_3 & r_4 & \ddots & & r_{M+2} \\ \vdots & \ddots & \ddots & \ddots & & \\ & & & & & r_{M+N-1} \\ r_N & & & & r_{M+N-1} & r_{M+N} \end{pmatrix}. \tag{B.16}$$

Note that an additional row and column are added in the system of equations, because the coefficients q_0 and $h_0/2$ appear both in the positive and negative parts of the partitioned vectors. It can be verified that equation (B.7) can be rewritten in partitioned form as:

$$\begin{pmatrix} \mathbf{R}^{-,-} & \mathbf{R}^{-,+} \\ \mathbf{R}^{+,-} & \mathbf{R}^{+,+} \end{pmatrix} \begin{pmatrix} \mathbf{h}^{-} \\ \mathbf{h}^{+} \end{pmatrix} = \begin{pmatrix} \mathbf{q}^{-} \\ \mathbf{q}^{+} \end{pmatrix}. \tag{B.17}$$

For a symmetric filter, $\mathbf{h}^{-} = \mathbf{h}^{+}$, hence equation (B.17) reduces to:

$$\left(\mathbf{R}^{+,+} + \mathbf{R}^{+,-}\right) \mathbf{h}^{+} = \left(\mathbf{q}^{+} + \mathbf{q}^{-}\right)/2, \tag{B.18}$$

whereas for an antisymmetric filter, $\mathbf{h}^{-} = -\mathbf{h}^{+}$. This gives:

$$\left(\mathbf{R}^{+,+} - \mathbf{R}^{+,-}\right) \mathbf{h}^{+} = \left(\mathbf{q}^{+} - \mathbf{q}^{-}\right)/2. \tag{B.19}$$

These systems of equations can be solved for the independent filter coefficients using a damped least-squares solution. Prewhitening of the data is essential to avoid artefacts as a result of limited bandwidth.

Samenvatting (Summary in Dutch)

Seismische reflectiemethoden worden veel gebruikt voor het opsporen van olie en gas in de ondergrond. In landseismiek worden de meeste data gemeten aan het aardoppervlak. Voordat echter een goed beeld van de diepere ondergrond verkregen kan worden is het noodzakelijk om de invloed van ondiepe structuur op deze data te begrijpen. Deze effecten kunnen onderverdeeld worden in twee categorieën: (i) het effect van ondiepe structuur op golfvoortplanting, en (ii) het effect op data acquisitie. Data acquisitie omvat zowel excitatie als registratie van het golfveld, dus de effecten van bron en ontvanger.

Golfvoortplanting nabij het aardoppervlak is vaak erg complex omdat snelheden van compressionele (P) en transversale (S) golven in deze zone vaak sterk variëren. Om inzicht te krijgen op de invloed hiervan op de geregistreerde data is het dus belangrijk om deze materiaaleigenschappen te kunnen bepalen. Hiervoor zijn er verschillende methoden ontwikkeld en getest. Deze methoden maken gebruik van een dicht netwerk van ontvangers inclusief geofoons op diepte. Deze P- en S golfsnelheden kunnen namelijk niet bepaald worden met een conventionele acquisitiegeometrie zonder begraven geofoons. Van de geteste methoden was degene die gebaseerd is op inversie van de "propagator matrix" het minst gevoelig voor meetfouten. Deze methode is succesvol toegepast op data gemeten nabij Zeist. Deze data lieten zien dat het golfveld nabij het aardoppervlak sterk variëerde met de diepte. Dit kon verklaard worden door interferentie van vlakke golven. Tevens konden met behulp van "propagator inversie" de P- en S golfsnelheden bepaald worden: een P-snelheid was geobserveerd van 270 ± 15 m/s voor de bovenste meter in de ondergrond, hetgeen lager is dan de P-snelheid in lucht (geluidssnelheid), en de S-snelheid was 150 ± 9 m/s. Dit betekent dat golfvoortplanting gevoelig is voor deze materiaaleigenschappen, en dat deze in principe nodig zijn voor het verder correct bewerken van de data. Deze lage snelheden worden echter niet vaak geobserveerd omdat snelheden sterk toenemen met de diepte, en omdat met een conventionele acquisitie geen gevoeligheid verkregen wordt voor deze ondiepe materiaaleigenschappen.

Het tweede deel van dit proefschrift behandelt de effecten van bron en ontvanger op seismische data. Deze verstoren het beeld van de ondergrond als hun eigenschappen veranderen binnen een experiment. Deze situatie is karakteristiek voor landseismische experimenten. Verstoringen worden veroorzaakt doordat een seismische bron, bijvoorbeeld een explosie, in los zand een compleet ander signaal zal uitzenden dan in hard gesteente. Daarnaast heeft ook de ontvanger invloed op het uiteindelijk geregistreerde signaal. Naast de response van het instrument zelf bepaalt ook het contact met de grond hoe goed de bodembeweging wordt geregistreerd.

Een nieuwe methode is ontwikkeld om voor deze verstorende effecten te corrigeren. Deze methode is direct toepasbaar op het gehele geregistreerde signaal, en vereist geen aannames over de ondergrond. De methode maakt gebruik van reciprociteit van golfvoort-

planting in de ondergrond. Dit betekent dat verschillen tussen metingen met verwisselde bron- en ontvanger posities veroorzaakt worden door acquisitie effecten: het signaal van het medium blijft namelijk gelijk wanneer bron- en ontvanger posities worden verwisseld. Deze methode was succesvol toegepast op zowel synthetische als experimentele data. De experimentele data waren verkregen in Manistee County, Michigan (WesternGeco). Gedurende de acquisitie was geobserveerd dat de bodemeigenschappen langs de seismische lijn veranderden. De verkregen broncorrecties waren sterk gecorreleerd aan deze bodemeigenschappen, terwijl de correcties voor de ontvanger variëerden van locatie tot locatie. Compensatie van deze data voor de bron- en ontvanger effecten leverde een duidelijker beeld van de ondergrond op. De resultaten van de bron- en ontvanger correcties op deze data zijn zodanig goed dat de verwachting is dat deze techniek een belangrijke bijdrage kan leveren aan het verbeteren van de kwaliteit van landseismische data.

Dankwoord (Acknowledgments)

Vele mensen hebben bijgedragen aan de totstandkoming van dit proefschrift, en ik wil iedereen hier graag voor bedanken.

I would like to express my gratitude to my promotor Jeannot Trampert for giving me the opportunity to carry out this challenging research project. I really appreciated your daily guidance and availability whenever I had any question. I am also grateful for your efforts convincing me that the developed methods would also work on land seismic data, while I had still my doubts whether anything could be achieved with these data at all. I really enjoyed working with you!

I would like to thank Andrew Curtis for initiating this research project. I very much enjoyed the many inspiring discussions which we had during my visits in Cambridge and Edinburgh and on the phone. I appreciated your promptness and accuracy in reading, and also your skills to get in touch with me to give feedback, wherever you were. It was a great experience working with you!

I acknowledge Schlumberger for funding this research project, and WesternGeco for providing the Michigan field data. I would like to thank Everhard Muyzert, Henk Keers, Romain Prioul, Ed Kragh, Leo Eisner, Ralf Ferber, Chris Chapman, Stephen Arrowsmith, Johan Robertsson and James Dale for the nice times in Cambridge. I still will have to return to go punting and for some pints!

Verder wil ik Hanneke Paulssen, Dirk-Jan van Manen, en Remco Muijs bedanken voor vele nuttige discussies, hulp, collegialiteit, en morale steun. Graag zou ik ook Tim van Zon, Stefan Carpentier, en Henk van der Meer willen bedanken voor hun bijdrage aan de veldexperimenten. Daarnaast wil ik Stefan ook bedanken voor zijn bijdrage aan de data processing.

I would like to express my gratitude to the members of the dissertation committee: Klaus Holliger, Roel Snieder, Chris Spiers, Peter Vermeer, and Kees Wapenaar, for their valuable comments which helped to improve this manuscript.

Een aantal mensen hebben belangrijke ondersteuning verricht. Joop Hoofd en Theo van Zessen wil ik bedanken voor het helpen met en het voorkomen van computerproblemen, Jacqueline Landsheer voor het scheppen van overzicht in de administratieve rompslomp, en Jan Jansen voor zijn hulp in de bibliotheek.

Vele collega's hebben de afgelopen jaren tot een aangename tijd gemaakt. Mijn kamergenoten Karin Visser, Renate Hartog, Hester van de Kasteele, en Yvonne Zwiers wil ik speciaal bedanken. Zonder jullie was het lang niet zo gezellig geweest. Ook alle andere collega's en oud-collega's wil ik bedanken voor gezelligheid bij de koffie- en theepauzes, lunches, en borrels: Caroline Beghein, Joe Resovsky, Ueli Meijer, Peter van Thienen, Frederic Deschamps, Vessa Dimova, Dirk Kraaijpoel, Joost van Summeren, Arie van Wettum, Sergei Lebedev, Maisha Amaru, Jacqueline Landsheer, Kabir Roy Chowdhurry. Jesper Spetzler, Arend Dijkstra, Xiao Mei Zhang, Ebru Bozdag, en vele anderen, bedankt!

Gelukkig was er ook nog tijd over naast het werk. Graag wil ik Martin Bootsma en Stefan Nobbenhuis bedanken voor vele momenten van ontspanning. Op de tennisbaan en

het schaakbord kon er altijd flink op los gemept worden. Ook wil ik mijn clubgenoten van D4 bedanken voor de vele aangename uurtjes tijdens en na het schaken. Hiernaast wil ik Carlijn Langeveld, Nick Cox, Idsard Septer, Jet Hengeveld, Evert Kramer, en iedereen die ik vergeten ben bedanken voor de goede tijden naast het werk.

Mijn ouders hebben me altijd volledig gesteund en aangemoedigd, op school, tijdens mijn studie, en zo ook gedurende dit project. Ik ben ze hiervoor enorm dankbaar. Ook wil ik Bas en Ellen bedanken voor hun steun en aanmoedigingen. Tenslotte wil ik Jojanneke bedanken voor haar liefde, geduld, en vele fijne momenten samen.

Curriculum vitae

July 13th 1977	Born in Raamsdonk, The Netherlands
1989-1995	Secondary school, St. Oelbert Gymnasium, Oosterhout, The Netherlands
1995-2000	Study of Geophysics, Utrecht University, The Netherlands
2000-2005	Ph.D. Student in the Seismology research group, Utrecht University, The Netherlands, in collaboration with Schlumberger Cambridge Research, United Kingdom

List of publications

Patents

R. Van Vossen, A. Curtis, and J. Trampert, 2003. Method for retrieving local near-surface material information. UK Patent No. 2,397,378. PCT Patent No. 0300876.0. Granted 02/03/2005.

R. van Vossen, A. Curtis, J. Trampert, 2004. Method for correcting seismic data. PCT Patent No. 0426232.5.

Papers

R. van Vossen, J. O. A. Robertsson and C. H. Chapman, 2002. Finite-difference modeling of wave propagation in a fluid-solid configuration, *Geophysics*, 67, 618-624.

R. van Vossen, J. Trampert, and A. Curtis, 2004. Propagator and wave-equation inversion for near-receiver material properties, *Geophysical Journal International*, 157, 796-812.

R. van Vossen, A. Curtis and J. Trampert, 2004. Subsonic near-surface P-velocity and low S-velocity observations using propagator inversion, *Geophysics*, in press.

R. van Vossen, A. Curtis and J. Trampert, 2004. Surface-consistent amplitude corrections for single- or multi-component sources and receivers using reciprocity and waveform inversion, submitted to *Geophysical Journal International*.

R. van Vossen, A. Curtis, A. Laake and J. Trampert, 2005. Equalization of source and receiver amplitude responses using recprocity and waveform inversion – Application to land seismic data, submitted to *Geophysics*.

Extended Abstracts

R. van Vossen, J. O. A. Robertsson and C. H. Chapman, 2000. Finite-difference modelling of wave propagation in a fluid/solid configuration, 62nd Ann. Internat Mtg., Eur. Assn. Geosci. Eng., Expanded Abstracts, C-41.

R. van Vossen, J. Trampert and A. Curtis, 2003. Propagator inversion for shallow structure, 73rd Ann. Internat. Mtg., Soc. Expl. Geophys., Expanded Abstracts, 82-85.

R. van Vossen, A. Curtis and J. Trampert, 2005. Source and receiver equalization using reciprocity, 67th Ann. Internat. Mtg., Eur. Assn. Geosci. Eng., Madrid.